# Material-Point Analysis of Large-Strain Problems

*modelling of landslides*

Andersen, Søren

*Publication date:*
2009

*Document Version*
Publisher's PDF, also known as Version of record

# *Material-Point Analysis of Large-Strain Problems: Modelling of Landslides*

***Søren M. Andersen***


**ISSN 1901-7294**
**DCE Thesis No. 20**

**Department of Civil Engineering**

Aalborg University
Department of Civil Engineering
Water and Soil / Structural Mechanics

**DCE Thesis No. 20**

# *Material-Point Analysis of Large-Strain Problems: Modelling of Landslides*

PhD thesis by

Søren M. Andersen

December 2009

## Scientific Publications at the Department of Civil Engineering

***Technical Reports*** are published for timely dissemination of research results and scientific work carried out at the Department of Civil Engineering (DCE) at Aalborg University. This medium allows publication of more detailed explanations and results than typically allowed in scientific journals.

***Technical Memoranda*** are produced to enable the preliminary dissemination of scientific work by the personnel of the DCE where such release is deemed to be appropriate. Documents of this kind may be incomplete or temporary versions of papers—or part of continuing work. This should be kept in mind when references are given to publications of this kind.

***Contract Reports*** are produced to report scientific work carried out under contract. Publications of this kind contain confidential matter and are reserved for the sponsors and the DCE. Therefore, Contract Reports are generally not available for public circulation.

***Lecture Notes*** contain material produced by the lecturers at the DCE for educational purposes. This may be scientific notes, lecture books, example problems or manuals for laboratory work, or computer programs developed at the DCE.

***Theses*** are monograms or collections of papers published to report the scientific work carried out at the DCE to obtain a degree as either PhD or Doctor of Technology. The thesis is publicly available after the defence of the degree.

***Latest News*** is published to enable rapid communication of information about scientific work carried out at the DCE. This includes the status of research projects, developments in the laboratories, information about collaborative work and recent research results.

Published 2009 by
Aalborg University
Department of Civil Engineering
Sohngaardsholmsvej 57,
DK-9000 Aalborg, Denmark

Printed in Denmark at Aalborg University by UniPrint

ISSN 1901-7294 DCE Thesis No. 20

# Preface

The present thesis "Material-Analysis of Large-Strain Problems: Modelling of Landslides" has been prepared in in partial fulfillment of the requirements for obtaining the degree of Doctor of Philosophi. The Ph.D. study carried out in the period July 2006 to December 2009 at Department of Civil Engineering, Aalborg University, Denmark.

First of all, I wish to thank my supervisor, Associate Professor, Dr. Lars Andersen, for many fruitful discussions.

I am also grateful to Professor Deborah Sulsky, who I was working with, when I spent five months in the spring of summer of 2007 at the University of New Mexico, New Mexico, USA exploring the material-point method. Professor Sulsky is one of the creators of the material-point method which is used extensively in this thesis. Professor Sulsky provided us with many ideas for improving the algorithms of the material-point method.

Next, I would like to thank Assistant Professor, Dr. Johan Clausen for assisting with the implementation of an effective material model for soil which I have utilized for the computational experiments.

I would also like to thank my friend Mr. Stefan Hansen for his enthusiastic assistance in performing a Land Survey of a local landslide.

Finally, I would like to thanks my friends and family for support during the preparation of this thesis.

Aalborg, December 2nd, 2009 Søren Mikkel Andersen

# Summary in English

The aim of this thesis is to apply and improve the material-point method for modelling of geotechnical problems. One of the geotechnical phenomena that is a subject of active research is the study of landslides. A large amount of research is focused on determining when slopes become unstable. Hence, it is possible to predict if a certain slope is stable using commercial finite element or finite difference software such as PLAXIS, ABAQUS or FLAC. However, the dynamics during a landslide are less explored.

The material-point method (MPM) is a novel numerical method aimed at analysing problems involving materials subjected to large strains in a dynamical time–space domain. This thesis explores the material-point method with the specific aim of improving the performance for geotechnical problems. Large-strain geotechnical problems such as landslides pose a major challenge to model numerically. Employing material points to track all relevant variables and a computational grid to solve the equations of motion, the material-point method avoids some of the problematic issues associated with traditional numerical models such as the finite element method. However, several challenges for the method exist as discussed in this thesis.

The thesis discusses the state of the art of the material-point method. Further, it presents ideas to better represent problems involving extreme deformations utilizing the framework of the generalized interpolation material point method (GIMP). Some of the results of this thesis are presented in the form of three research papers. The content of the individual papers are summarised below.

**I. Analysis of Spatial Interpolation in the Material-Point Method**

This paper analyses different types of spatial interpolation for the material-point method. The paper explores how the functions that map between the material points and the grid influences the behaviour of the method. It compares the traditionally employed linear mapping with quadratic interpolation and interpolation using cubic splines. It is demonstrated that using smoother interpolation functions improves the representation of stresses at the individual material points. However, it is found that quadratic interpolation is not generally applicable for the material point method. An important result is that although stresses are not realistic at the individual material points, stresses are always realistic for linear elastic problems when interpolated to the grid nodes.

**II. Modelling of Landslides with the Material-Point Method**

In this paper the ability of the material-point method to model landslides is explored. The GIMP formulation is employed. A simplified slope with a house placed on top of the slope is analysed. An algorithm to obtain initial stress states based on an incremental gravitation scheme is presented and an elasto-plastic material model based on the Mohr-Coulomb yield criterion is employed for the soil. The slides are triggered for the initially stable slopes by removing the cohesion of the soil. Using the time-space integration scheme of the MPM, the slide is followed from the triggering until a state of static equilibrium is again reached. Parameter studies, in which the angle of internal friction of the soil and the degree of discretization are varied, are presented.

**III. Material-point analysis of collapsing slopes**

This paper involves a case study of a recent landslide near Rubjerg Knude in north western Denmark. This landslide took place November 2008 at a steep slope near the beach in an area where landslides are actively forming the landscape. The modelling employs several of the ideas presented in this thesis. Data on the geometry are based on land surveying after the landslide. The result of the land survey is compared with GIS data from 2007. The slope before the slide is discretized using MPM and different algorithms for triggering the slide are tested. Despite a large uncertainty regarding the properties and variation of the soil layers before and after the slide, the presented numerical model provides insight into the physics while the slide took place.

The three research papers are placed at the end of the thesis as appendices, after the reference list. In addition to the three research papers, a state of the art example of a collapsing slope is included to demonstrate the proposed changes to the method. The example involves a detailed analysis of the dynamics of a collapsing slope. The influence of the elasto-plastic properties on the nature of the landslide is discussed. The example utilizes new ideas, that are not presented in the paper “Material-point analysis of collapsing slopes”, notably the adaptive scheme for splitting the material points in zones of large deformations and the new algorithm to visualize the physically realistic stresses.

It is worth noting, that the improvements of the material-point method suggested in this thesis are general and can be applied to all problems that are traditionally modelled with the material-point method.

# Summary in Danish

Formålet med denne afhandling er at anvende og forbedre materialepunktsmetoden for modellering af geotekniske problemer. Et geoteknisk fænomen, der er genstand for aktiv forskning, er studiet af jordskred. En stor del af den eksisterende forskning er forkuseret på forudsigelse af, hvornår skråninger bliver instabile. Ved hjælp af kommerciel finite element eller finite difference software som Plaxis, ABAQUS eller FLAC er det muligt at forudsige stabiliteten af visse typer af skråninger. Dynamikken under et jordskred er imidlertid mindre udforsket.

Materialepunktsmetoden (MPM) er en nyskabende numerisk metode specielt designet til at analysere problemer, der involverer materialer udsat for store tøjninger i et dynamisk tid–rum domæne. Afhandlingen udforsker materialepunktsmetoden med specielt fokus på at forbedre modelleringen af problemer, der involverer store flytninger. Geotekniske problemer med store tøjninger så som jordskred er en stor udfordring at modellere nummerisk. Ved at kombinere materialepunkter, der indeholder de relevante tilstandsvariabler, og et beregningsnet, hvor bevægelsesligningen løses, er materialepunktsmetoden i stand til at undgå nogle af problematikkerne, der er forbundet med de traditionelle metoder såsom finite element metoden. Imidlertid er der nye væsentlige udfordringer, der behandles i denne afhandling.

Afhandlingen diskuterer de nyeste ideer indenfor materialepunktsmetoden. Endvidere præsenteres ideer til at repræsentere problemer med ekstreme deformationer. Den numerske model, der ligger til grund for resultaterne i denne afhandling er baseret på den generaliserede interpolationsmaterialepunktsmetode (GIMP). En del af forskningsresultaterne i denne afhandling er præsenteret i form af tre forskningsartikler. Indholdet af de enkelte artikler er skitseret nedenfor.

**I. Analysis of Spatial Interpolation in the Material-Point Method**

Artiklen analyserer forskellige typer af rumlig interpolation for materialepunktsmetoden. Artiklen undersøger, hvordan funktionerne, der transformerer mellem materialepunkter og beregningsnet, indvirker på resultaterne. Der foretages en sammenligning af de traditionelle linære elementer med kvadratisk interpolation og kubisk, stykvis interpolation. Det vises, at højereordens interpolation forbederer repræsentation af spændinger for de enkelte materialepunkter. Imidlertid er kvadratisk interpolation ikke generelt anvendelig for materialepunktsmetoden. Som et vigtigt resultat demonstreres det, at der ved at interpolere til knuderne kan findes spændinger, der er realistiske for alle interpolationstyperne.

**II. Modelling of Landslides with the Material-Point Method**

I denne artikel udforskes det, hvordan materialepunktsmetoden kan anvendes til dynamisk modellering af jordskred. Til analyserne bebyttes GIMP-formuleringen. De numeriske analyser tager udgangspunkt i en simpel skråning med et hus på toppen. Der præsenteres en algoritme til at bestemme initialspændingstilstanden ved hjælp af inkremental gravitation. Jorden modelleres som elasto-plastisk materiale baseret på Mohr-Coulomb flydekriteriet. Jordskreddet startes for en oprindelig stabil skråning ved at fjerne kohæsionen. Ved hjælp af tid–rum integrationsalgoritmen i MPM følges jordskreddet fra det begyndende plastiske kollaps indtil jorden igen har opnået en ligevægtstilstand. Der præsenteres parameterstudier, hvor friktionsvinklen og diskretiseringen varieres.

**III. Material-point analysis of collapsing slopes**
Artiklen indeholder et specifikt studie af et nyligt jordskred ved Rubjerg Knude i det nordvestlige Danmark. Jordskreddet skete November, 2008 i en stejl skråning ved stranden. Skråningen er placeret i et område, hvor jordskred aktivt former landskabet. Modelleringen af jordskreddet udnytter mange af ideerne præsenteret i denne afhandling. Skråningens geometri efter skreddet er opnået ved landmåling. Resultaterne af landmålingen sammenlignes GIS data fra 2007. Skråningen før skreddet diskretiseres ved hjælp af materialepunktsmetoden og forskellige algoritmer for at initiere skreddet testes. På trods af de store usikkerheder omkring materialeegenskaber og jordlagsvariation før og efter skreddet, giver den numeriske model indsigt i fysikken under skreddet.

De tre artikler er vedhæftet som appendices sidst i afhandlingen, efter referencelisten. Udover de tre forskningsartikler præsenteres et eksempel med en kollapsende skråning, der viser ideerne til ændringer af GIMP algoritmen præsenteret i denne afhandling. Eksemplet indeholder en detaljeret analyse af dynamikken under jordskred. De elasto-plastiske materialeparametres betydning for jordskredstpen diskuteres. Eksemplet bentytter en række nye ideer, der ikke er præsenteret i forskningsartiklen "Modelling of Landslides with the Material-Point Method", specielt en adaptiv algoritme til at splitte materialepunkterne i zoner med store deformationer og en algoritme til at visualisere de fysisk realistiske spændinger.

Det er værd at bemærke, at forbedringerne af materialepunktsmetoden foreslået i denne afhandling er generelle og kan anvendes til alle problemer, der traditionelt modelleres ved hjælp af materialepunktsmetoden.

# Contents

# List of Figures

# CHAPTER 1
# Analysis of landslides

Fistly, the physics of landslides are discussed. This chapter includes a description of the state of the art within the analysis of landslides. The state of the art review is divided into a review of the geological landslide description, and an analysis of the traditional geotechnical analysis tools. Finally, modern computational methods that have been applied for analysis of slope stability and landslides are reviewed.

## 1.1 Introduction

In many places, cities are built next to unstable slopes and it is essential to understand the dynamics of a landslide. Specifically, it is of interest to obtain an idea of the extent of an eventual landslide. Further, if an unstable slope poses a significant risk, it is essential to understand the effect of landslide retaining structures. Numerical modelling is an essential tool in obtaining this knowledge.

However, landslides are very complex to study due to many factors. One complicating issue is that it is not possible to predict, precisely, when a landslide will occur–only general observations exists such that landslides typically take place due to saturation during heavy rainfall. Hence, the observations are often performed on the slope before and after the slide. Typically, detailed observations before the slides are also unavailable. Further, the properties of the slope are generally not known completely unless extensive testing has been performed. The determination of material properties is also complicated, as soil is an anisotropic, non-linear, non-homogenous material with properties changing over time. A third issue that poses a significant challenge modelling landslides, in comparison to other engineering problems, is the extreme deformations the soil undergoes. Most knowledge of soil behaviour is obtained by laboratory test in which the soil is subjected to significantly smaller deformations than observed under landslides.

The idea of this thesis is to explore the geological findings using detailed computational mechanics in order to better understand the dynamics during the slides. Hopefully, this understanding can be utilized to determine the risks in urban environments near unstable slopes, where slides will sooner or later occur. Further, it is the idea to develop a tool that can be applied do design landslide retaining structures.

The traditional analysis of landslides can be divided into two categories. The first category is the geological study of landslides. It involves describing the geological processes leading to landslides. Further, it describes the physical processes during the slide as well as determination of the extent of slides. The geological analysis is largely based on field studies. The second category of landslide analysis involves the slope stability analysis in geotechnical engineering. Here practice has mainly focused on determining the risk of slope failure.

## 1.2 Geological description of landslides

In the geological literature, landslides are used as common denominator for processes including rock falls, mudslides, debris-flows, debris avalanches as well as slides along a slip-plane. A schematic overview of different landslides as presented by the U.S. Geological Survey is shown in Figure 1.1.

The different types of landslides are often interrelated. For instance, rock falls can lead to slide of a soil slab along a failure surface due to the impact, which in turn can lead to debris flow due to liquefaction (Lacerda 2007). An extensive description of the mechanics of debris flows is given by Takahashi (2007) who analyses the mechanics of the soil and water during the debris flow type landslides. One important physical process leading to landslides is the effect of saturation on partially saturated soils. When a soil is partially saturated negative pore pressures due to capillarity yields an apparent cohesive strength to the soil skeleton. However, when the soil becomes fully saturated this cohesive strength disappears which can cause a sudden slide. A similar effect is that of roots from vegetation on the shear strength of the soil. The vegetation also applies suction preventing the top layers of a slope from reaching full saturation. Hence, deforesting or forest fires can easily lead to landslides. This is often the case in tropical regions.

Another cause of landslides, described by Lacerda (2007), is cyclic variations of pore pressures which can degrade cementation of soils. An example, where the risk of landslides is a major design parameter, is the Three Gorges Reservoir Region, China (Kequiang et al. 2009). The work of Fan et al. (2009) suspects the generation of uplift water pressures to be a likely cause for the frequent landslides in the Three Gorges Reservoir Region.

An example, where irrigation of fields likely triggered a massive landslide, is presented by Zhang et al. (2009). Another factor, often triggering landslides, is earthquakes. The work of Chen and Hawkins (2009) explores how earthquake disturbance along with tropical rainstorm cause a large number of debris flow type landslides in Taiwan. The work by Guthrie et al. (2009) attributes weathering, along with a raise in pore water pressures in the rock, to be cause to a massive rock slide–debris avalanche at Guinsaugon Philippines. In the mentioned paper, the authors suspect the earthquake that appeared after the slide to be triggered by to tectonic unloading as a results of the magnitude of the slide.

In northern areas, landslide phenomena are often due to the glacial tectonic effects during the last ice ages. This is the case in northern Denmark, where the work of Pedersen (2006) describes how the glacial tectonic processes during the ice age lead to a complex of unstable soil slopes. Here soil layers are inclined at angles of up to 60 degrees from horizontal. Landslides typically take place due to slips along interfaces between sand and clay. A recent slide in the area from December, 2008, is shown in Figure 1.2. Paper III of this thesis deals further with this recent slide.

In Norway, the presence of glaciomarine and marine clays leads to many landslides, especially in the presence of the so called quick clays. Quick clays are characterized by the fact that remolding completely collapse the clay structure, dramatically reducing the shear strength towards zero. Hence, initial plastic deformation can lead to dramatic progressive slides, similar to mudslides. The work by Eilertsen et al. (2008) analyses the occurrence and triggering mechanisms for the clay slides in the Måselv valley in northern Norway. Figure 1.3 shows an examples from this work illustrating slides in quick clays.

Another area, where landslides pose a huge risk, is on volcanos. The material deposited by volcanic eruption often leads to unstable slopes. Examples of slides include the flank collapse

at the Casita Volcano in Nicaragua (Devoli et al. 2009). Here a large volume of 260 000 $m^3$ of highly fractured volcanic breccia collapsed and started to move rapidly. During movement, the breccia passed clay-rich pyroclastic deposits, which triggered an even larger slide. Another

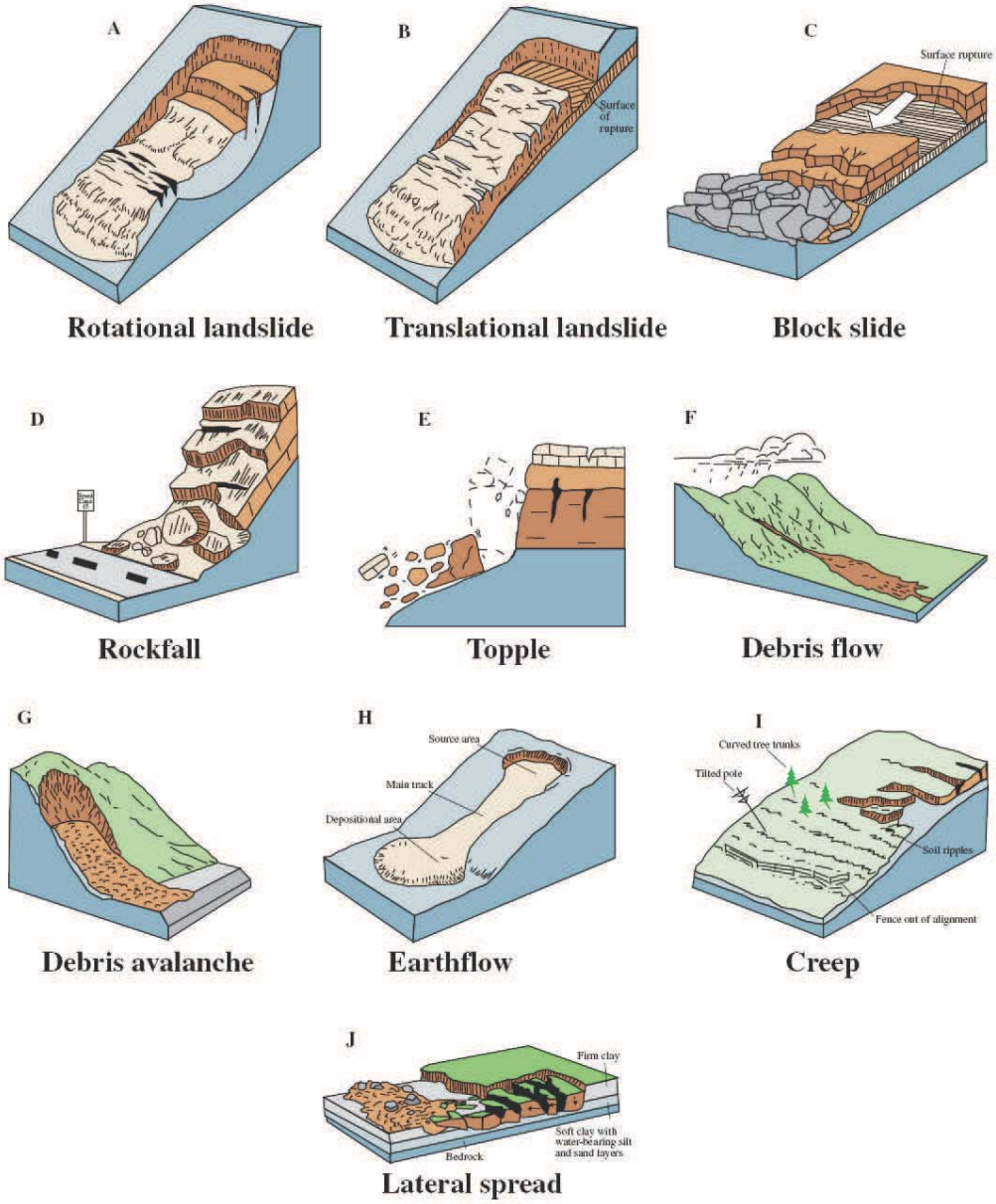


**Figure 1.1** Definition of different types of landslides. U.S. Geological Survey fact sheet (United States Geological Survey, 2004). Reproduced by courtesy of the U.S. Geological Survey.

**Figure 1.2** A recent slide at the coast in Northern Denmark. An analysis of this slide is presented in Paper III.

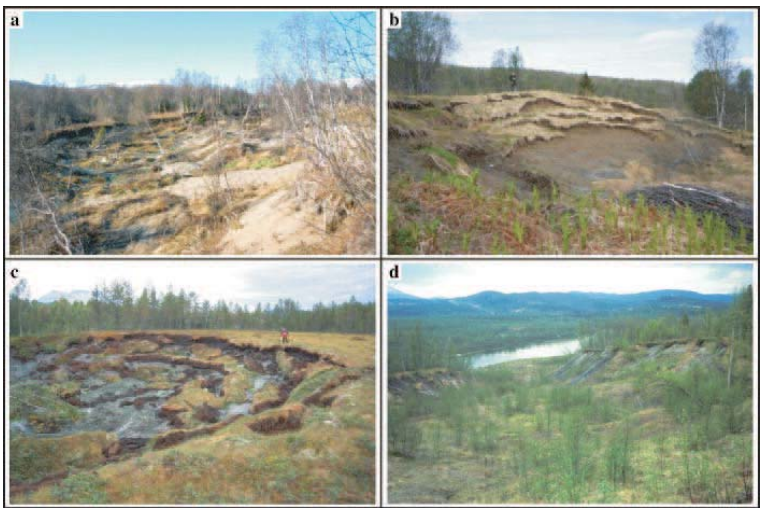


**Figure 1.3** Quick clay slides in Måselv valley, Norway. Note the person in the pictures (b and (c for an idea of the extent. Reproduced with permission from the work of Eilertsen et al. (2008)

example is the collapse of the volcano on Stromboli, Italy (Apuanui et al. 2005). Analysis shows that without external triggering forces the volcano should be stable. As a major destabilizing factor, the authors mention magma pressures from dykes. In areas of volcanic deposits, flow-

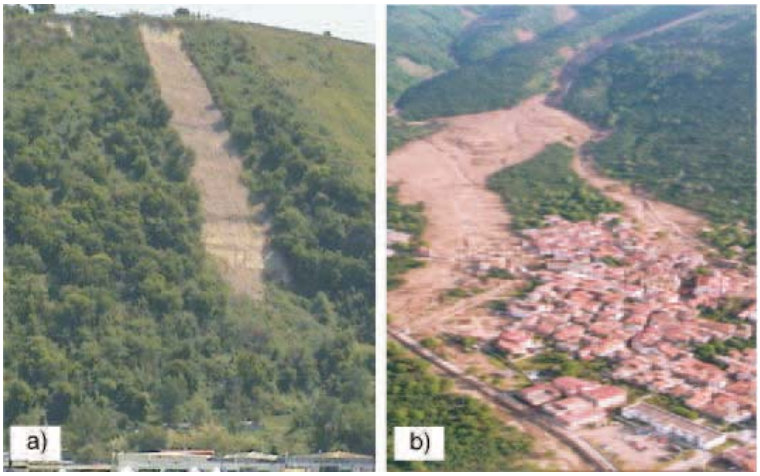


**Figure 1.4** Examples of flow like landslides in volcanic soils: a) Debris avalanche, b) liquefied debris flow. Reproduced with permission from the work of Picarelli et al. (2008) .

like landslides and avalanches are observed. Figure 1.4 shows two examples of rainfall induced landslides in pyroclastic soils from the Campania Region in Italy, from the work of Picarelli et al. (2008).

The work of Hasegawa (2009) suggest that one of the main causes of landslides in the Lesser Himalaya of central Nepal is the the clay mineralization in sliding zones during advancement of the Main Central Thrust tectonic plate.

Landslides triggered due to climate changes has also become a topic of research. The work by Jakob and Lambert (2009) discusses how climate changes will lead to an increase in short-term intense rainfall, which is expected to increase the frequency of landslides in British Colombia, Canada. Wang et al. (2009) analyse landslides in the Northwest Territories, Canada, due to climate induced thaw on fine-grained permafrost soils. An example from this article of a thaw induced landslide is shown in Figure 1.5.

## 1.3 Geotechnical analysis of slope stability

The geotechnical analysis of slope stability typically involves mechanical analysis of slopes subjected to extreme expected forces, in order to determine the risk of failure. The analysis is usually static, utilizing the concept of limit equilibrium. Limit equilibrium refers to an extreme case, where the soil is at rest in equilibrium, but equilibrium cannot be obtained for a further increase of the load. The work by Duncan (1996) presents the state of the art of slope stability research from the seventies to the nineties. Limit equilibrium analysis of slope stability is typically focused on determine a factor of safety, $F$, defined by

$$F = \frac{Shear\ \ strength\ \ of\ \ the\ \ soil}{Shear\ \ strength\ \ required\ \ for\ \ equilibrium} \tag{1.1}$$

In order to determine an analytical safety factor, the traditional geotechnical engineering analysis tools for slope stability analysis typically employ the rigid-perfect plastic constitutive idealiza-


**Figure 1.5** Example of a thaw induced slide, Mackenzie Valley, Canada. The area of the largest slide shown is about 30.000m$^2$. Reproduced with permission from the work of Wang et al. (2009).

.

tion. The Mohr-Coulomb yield criterion is typically applied to determine failure.

One of the early tools for determining the stability of a slope is slope stability charts. A slope stability chart can be employed to determine the safety of a slope using simple, dimensionless charts. Using the charts, the safety factor can be determined based the slope angle, the effective cohesion, the effective friction angle, the density of the soil and other relevant parameters. The development of slope stability charts is attributed to Taylor (1948) and Janbu (1954). More recently, Huat et al. (2006) present the development of stability charts for analysing tropical residual slopes. The approach defines a dimensionless stability number. As an example, the stability number for a slope consisting of uniform, dry soil is defined by

$$N = \frac{c}{\gamma H F}, \tag{1.2}$$

where $c$ is the cohesion, $\gamma$ is the unit weight of the soil and $H$ height of the slope. Figure 1.6 shows a corresponding stablilty chart presented by Michalowski (2002).

For a safety factor of $F = 1$, the stability number describes the combination of $H$, $c$ and $\gamma$, at which the slope is a state of limit equilibrium for a given angle of internal friction.

Another method for determining the slope stability for slopes with a circular slip surface is known as the ordinary method of slices. The ordinary method of slices is attributed to Fellenius (Duncan 1996). It assumes a circular slip surface in the soil and calculates the stabilizing and destabilizing forces utilizing the principle of virtual work. Another similar method is known as Bishop's modified method. Bishop's method satisfies moment equilibrium and equilibrium of vertical forces, but does not satisfy equilibrium of horizontal forces. Bishop's modified method is utilized by Han et al. (2004) to analyse the slope stability of embankments over deep mixed foundations. The ordinary methods of slices and Bishop's modified method are both upper bound

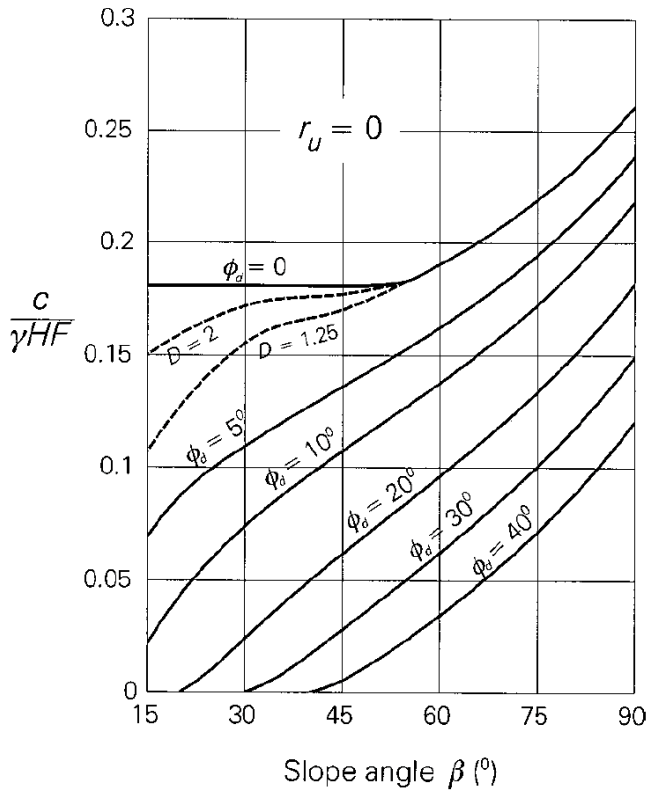


**Figure 1.6** Stability chart provides an easy determination of slope stability for simple cases. The chart is a reproduction with permission from Michalowski (2002). This chart is for a non-saturated uniform slope. The parameter $\phi_d$ is defined by $F = \frac{\tan\phi}{\tan\phi_d}$, where $\phi$ is angle of friction.

solutions as they satisfy kinematic conditions, but do not satisfy all equilibrium equations. Hence, they tend to overestimate the safety factor for a given slope. Another traditional family of methods is the force equilibrium methods of slices. The work by Furuya (2004) presents an overview of the most popular methods. Figure 1.7 shows an example of limit equilibrium analysis using the method of slices.

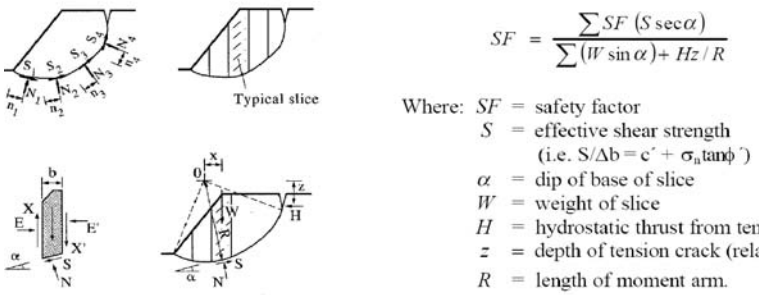


**Figure 1.7** Limit equlibruim analysis of slope stability using the methods of slices for a circular failure. The figure is a reproduction of the work by Eberhart (2003).

## 1.4 Modern computational methods

Evidently, there exists a huge gap from the geological understanding of landslides to what is included in the traditional geotechnical slope stability analysis. The ability to combine the detailed geological knowledge with accurate mechanical models to perform detailed analysis has traditionally been limited due to the lack of computational models.

During the last decades, computer power and the availability of analysis software has changed this picture. One of the most applied methods for numerical analysis of geotechnical problems is the finite element method (FEM) (Zienkiewicz et al. 2005). The finite element method for solids assumes a continuum description of the material. In the finite element method, the material is discretized using a finite set of grid nodes. The set of nodes defines a finite set of elements. The spatial variation within each finite element is governed by shape functions defined at the nodes. Each finite element has an associated mass, and field variables are assumed to vary within the elements according to the shape functions associated with the nodes. A discretization technique for the continuum, where the governing equations of continuum mechanics are formulated in a weak form, lead to a system of algebraic equations at the grid-nodes. Within each finite element, Gauss points are typically used to obtain necessary integrals as a result of this weak formulation. Figure 1.8 shows the commercial finite element code ABAQUS employed to determine the vertical normal stresses of a slope with a house on top. The dynamic collapse of the slope in the figure is analysed in Paper II

Finite element methods can be divided depending on whether they are used for analysis of static or dynamic problems. In respect to slope stability analysis, the static FE analysis involves comparing the state of stress in the slope with the corresponding state of deformation. The static FEM formulation overcomes many of the approximations associated with the slope stability methods. Firstly, it is possibly to represent accurately the geometry of the slope. Secondly, the FEM allows for incorporation of advanced models for the constitutive behaviour of the soil. One of the most popular constitutive models for soil is the elasto plastic model based on the Mohr-Coulomb yield criterion. The work by Clausen et al. (2006) discusses how to implement elasto plastic material models in a finite element framework for associated plasticity while Clausen et al. (2007) presents the corresponding non-associated formulation. Using elasto plastic material

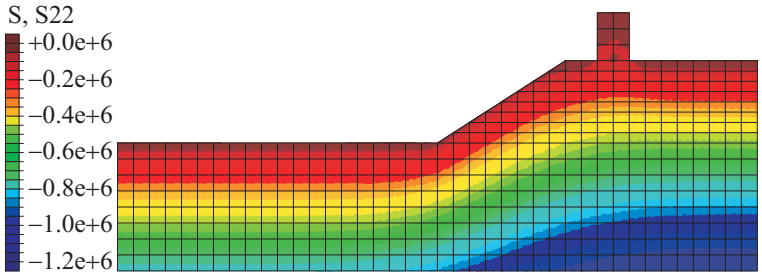


**Figure 1.8** Vertical normal stresses for a slope with a house on top obtained with the commercial FE analysis tool ABAQUS. The collapse of this slope is analysed in Paper II.

models, it is possible to study how stresses evolve from an elastic state to a plastic state.

A way to apply FEM to study the stability of slopes is discussed by Tsuchiya et al. (2009). Here the shear strength utilized in the constitutive model is gradually reduced until failure of the slope is observed in the numerical model. Failure is defined to occur at a state similar to the limit equilibrium at the threshold, where global equilibrium and the Mohr-Coulomb yield criterion can just be satisfied. The authors show that the slip surface predicted by the FEM model is similar to actual failure observed. One important application for geotechnical engineering and landslides is the ability to include the interaction of pore water and the soil skeleton. The work by Zienkiewicz (1999) describes how a finite element scheme can be applied to model coupled problems involving interaction of water and soil in saturated and partially saturated soil based on the principle of effective stress. Currently, the finite element method is by far the most popular method for analysis of quasi-static geotechnical problems.

The above described references focus on determining the triggering of landslides. More recently, dynamic finite element modelling has become part of geotechnical engineering research. The dynamic finite element method is in many respects very similar to the material point method. Dynamic finite element models solve the balance of momentum equation in order to find the acceleration of the material at the nodes, where the governing equations are solved. A time-integration scheme is then used to update the velocity and position of the nodes. The position of the nodes is then used to find updated location of the Gauss points. Applications of dynamic finite element modelling involve the simulation of a slow moving natural slope in the Upper-Austrian Alps using a visco-hypoplastic constitutive model (Ham et al. 2009) and flow-like landslides in the Las Colinas Landslide, El Salvador (Crosta et al. 2005).

The original finite element formulation is known as a Lagrangian material description. This means that the computational mesh follows the deformation of the material. Hence, the strains are directly determined by the relative movement of the mesh. Further, as the mesh follows the deformation, the amount of mass to associate with a given finite element is the same at all points in time. The Lagrangian material description is the natural approach to solid problems.

For problems involving extreme deformations, some drawbacks are associated with the application of the FEM. As shown in several texts, the interpolation functions used in the FEM produce the highest accuracy, if the the finite elements are of regular shapes. During a landslide, the deformations that take place significantly degrades the computational mesh. Another issue is the modelling of interaction of different soil layers. In the landslide modelling presented in Paper III the triggering mechanism is the slip along the interface between soil layers. This kind of interaction is non trivial to model in the FEM in the case where both layers undergo large

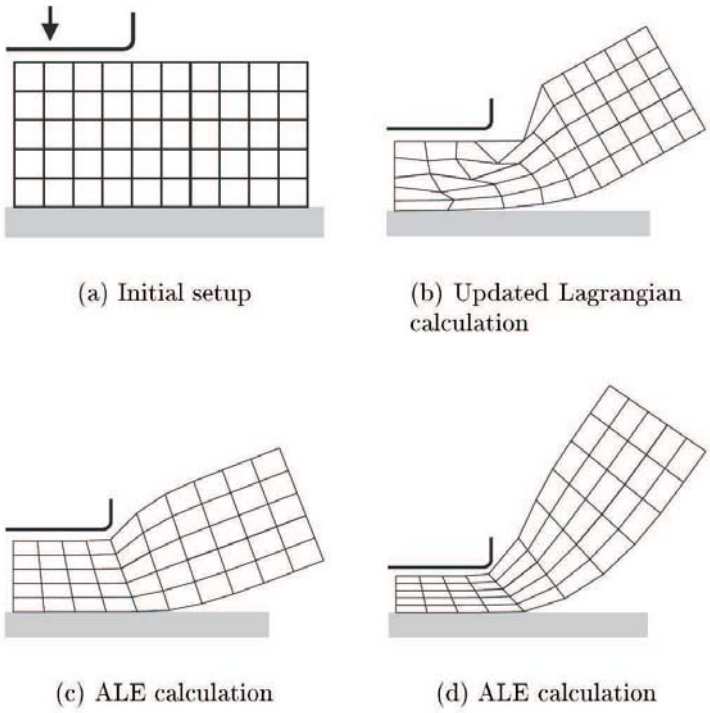


**Figure 1.9** Principles of the ALE. a) is the initial configuration. b) shows that the mesh becomes severely distorted if no re-meshing is performed. c) and d) show updated meshes as a result of ALE re-meshing and remapping. This example is a reproduction of Stoker (1999).

plastic deformations.

Another idea is to model the material using a spatially fixed set of nodes, which is known as a Eulerian formulation. Here, the material will move relatively to the grid. Hence, the mesh will not undergo any deformation. However, a pure Eulerian formulation introduces several new problems. Firstly, the amount of mass associated with a node will generally vary in a dynamical problem and may not be easy to determine with a high degree of accuracy. Secondly, in order to determine for instance strain rates for the material, convective terms will need to be accounted for. The work by Liu et al. (Liu et al. 2007) describe the algorithms for tracking state variables in Eulerian problems. The Eulerian formulation is the natural choice for fluid problems.

One of the areas, where both Eulerian and Lagrangian formulations has been applied, is in complicated fluid problems for instance particle transport by a fluid carrier and turbulence. The work by Deubelbeiss and Kaus (2008) compares the performance of Eulerian and Lagrangian grids for modelling problems governed by the Stokes equations in the presence of strongly varying viscosity. The work by Hryb et al. (2009) analyses particle transport in turbulent fluid flow using both Lagrangian and Eulerian formulations while the work by Falkovich et al. (2001) demonstrate how the use of a Lagrangian description can enhance the modelling of fluid turbulence.

The arbitrary Lagangian–Eulerian method (ALE) is a method that tries to avoid the draw-

backs of the finite element method formulated in a pure Lagrangian description by introducing an extra Eulerian material description. An extensive presentation of the ALE method is given by Stoker (1999). The idea is to employ both a Lagrangian and a Eulerian description of the material. Hence, in addition to the Lagrangian description from the FEM model a Eulerian mesh is used. When the current Lagrangian finite element mesh becomes significantly distorted, the Eulerian mesh is utilized to define a new Lagrangian mesh, which is more regular. Figure 1.9 shows how the ALE method can be applied to model a metal forming process. The figure is a reproduction of the work by Stoker displaying the concept of ALE re-meshing. Figure 1.9 b shows, that without any re-meshing, the mesh becomes significantly distorted, hence degrading the quality of the numerical solution. Figure 1.9 c) and d) shows how the ALE re-meshing maintains a smoother mesh. In the work by Wójcik and Tejchman the ALE formulation is employed to study the shear localization for confined granular flow in silos. One drawback of the ALE method is the remapping of state variables that takes place when defining a new Lagrangian grid. Obviously, this remapping becomes more problematic, when a more complicated material model is employed.

In recent years, several methods have evolved that track the material by a discrete set of particles instead of a mesh. These methods include smoothed particle hydrodynamics (SPH) (Monaghan 2005), the finite point method (Õnate et al. 1996), the element-free Galerkin method (Li and Belytsko 2001), reproducing kernel particle methods (Chen et al. 1996) and the hp-mesh-less cloud method (Duarte and Oden 1996; Liszka et al. 1996). A comparison study of the consistency and stability of particle methods, including SPH, the particle-in-cell method and the ALE method, is presented by Brackbill (2005) while a longer discussion of mesh-free and particle methods is presented by Belytschko (1996) and by Li and Liu (2002). The discretization in these methods involves locally defined approximation functions centered at the particles. The difference between the methods largely depends on the type of approximation functions. SPH applies integral representations of the field quantities using kernel functions. The work of Cleary and Monaghan (1999) uses products of cubic b-splines as kernel functions in SPH modelling while Liu (2002) explores different kernel functions for SPH. In the finite point method the approximation is based on a finite difference scheme, while the element free Galerkin and the hp-cloud methods uses moving least square approximations. A review of mesh-less methods is given by Nguyen et al. (2008). A comparison of the of mesh-less methods with finite element and finite difference methods is presented by Trovec et al. (2009).

Some of the problems with pure particle based methods are associated with the need to determine the interaction of the particles. Typically, a domain of influence is defined for each particle and a search of neighbouring particles, that the particle interacts with, is needed. An open issue for pure particle methods is implementation of boundary conditions. Further, some numerical problems are notified when implementing the particle methods. In the work of Ma et al. (2009) the so called tension instability in SPH is noted to decrease the applicability for hyper-velocity impact problems.

Another method with some potential for geotechnical problems is the discrete element method (DEM). Opposite to the finite element method, the discrete element method models each grain/particle as a separate element. The interaction between different elements is governed by contact laws. The DEM has mostly been applied to study the mechanics of granular flows at the grain level. The work by Rycroft et al. (2009) applies the DEM to analyse granular flow phenomena in order to analyse the typical continuum representation of granular materials.

The mentioned methods so far are all in essence Lagrangian, in the sense that the particles

are tracked by either a Lagrangian mesh or by a set of particles. However, for certain mudslides, avalanches and submarine landslides, the soil acts more like a fluid than a solid during part of the slide. An analysis of the mechanics of granular flows is presented by Savage (1984) who discusses the application of fluid dynamical models to describe rapid granular flow using a Eulerian description. An analysis of submarine landslides using computational fluid mechanics to representing the submarine soil employed by Rzadkiewicz (1997) to study tsunamis induced by submarine landslides.

For studying landslides, one successfully applied model is cellular automata (D'Ambrosio et al. 2003). The method of cellular automata is very different from both the FEM and the particle based methods in the way the governing differential equations are resolved spatially. The cellular automata discretization consists of subdividing the surface area of a slope into regular cells. For each cell, a number of state parameters are defined including the altitude, the thickness of landslide debris, adherence of landslide debris to the basal surface, debris inflow/outflow, water content of debris. The cellular automata is specialized for slopes, where a stable base mountain is overlain by unstable debris.

## 1.5 Scope of this thesis

As described, the different methods have all been successfully applied to different problem areas. However, for modelling large strain geotechnical problems as landslides all the above methods have several drawbacks. The drawbacks associated with the finite element method have already been discussed. The generalization for large strains, the ALE method which has been successfully applied to study metal forming processes requires well defined boundaries in order to specify a useful Eulerian grid. The convective remapping in the ALE scheme would be very complicated for a soil deformation involving for instance a collapsing slope. Further, it is expected that the complicated neighbour search necessary in the pure particle based method along with the open question of boundary conditions likely preclude good results. Finally, the cellular automata though promising for certain types of landslides is not general enough for analysis of a majority of landslides types. Hence, the need for a method combining the possibility of accurate representation of large deformation and displacement and an easy representation of complicated material behaviour exists.

Here the material-point method stands out. In the material-point method, the state variables are, like the particle-based methods, tracked by a discrete set of particles, called material points. Further, a regular grid is employed to solve the governing equations. The grid is also utilized to define boundary conditions and to determine contact between multiple materials. As no state variables are associated with the grid, a regular grid can be utilized throughout the deformations associated with, for instance, a landslide without issues of convection. Thereby, the material point method combines the good features of the FEM and the purely particle based methods.

The initial aim of this PhD-project was to develop a computer program implementing the material-point method for the study of geotechnical problems, as no commercial software implementing the material-point method currently exists. Compared to the finite element method, the material-point method has been subjected for significantly less theoretical verification. Hence, many issues regarding the precise computational implementation are not completely resolved.

As will be apparent from Section 2.1, the calculation procedure for the MPM is very straightforward. So an MPM-code was soon produced. However, the initial program was seen to

produce results of varying quality depending on the nature of the test problems. Hence, improving the method with the special aim of improving the performance became a part of this research project. Thus, the scope of the research presented in this thesis can be formulated as:

- Improve the material point method for large strain problems,
- apply the material point method for state of the art modelling within geotechnical engineering.

The thesis presents the latest theory of the material-point method and presents several new ideas for modelling of large strain problems. To the authors best belief, the following aspects may be regarded as novel:

1. Numerical modelling of landslides using the material point method,
2. while the stresses may be unrealistic at the individual material points, physical stresses can found by mapping to the grid nodes,
3. new way of extracting the physically realistic stresses on the material points using the grid-node stresses,
4. numerical determination of GIMP weighting functions,
5. new algorithm for splitting material points using the GIMP implementation.

## 1.6 Layout of the thesis

Firstly, a review the material-point method (MPM) and the generalized material point method (GIMP) is presented. The remaining chapters contain the presentation of the new ideas. A brief introduction to each chapter is given below.

### Chapter 2

This chapter describes the current state of the art of the material-point method and the generalization of the material-point method, known as the generalized interpolation material point method (GIMP).

### Chapter 3

This chapter discusses how to model large strain problems. For the case of large deformations, Section 3.2 discusses how to track large deformations using the deformation gradient tensor as a state variable. Section 3.3 presents a way of implementing large strain descriptions into the GIMP framework. One important idea with respect to analysis of problems involving large deformations is to apply a finer discretization where the larger deformations occur, or where the stresses or other state variables need to be determined accurately. Section 3.4 provides a tool for dynamical adaptive discretization based on splitting material points in case of large deformations. An extension of the splitting scheme to the analysis of extremely localized shear deformation is presented in Section 3.4.2. An idea, although not implemented in any of the numerical examples, is to adaptively refine the grid, where the material points are split. This is discussed in Section 3.4.3.

### Chapter 4

One of the most problematic issues in respect to the material point method is the way in which stresses are treated. This chapter deals with this issue, analysing where and how to evaluate stresses and proposes a novel idea for visualization of stresses.

### Chapter 5

In order to show the potential of the proposed ideas, two case studies involving large deformations are presented. In the first example, a column of soil is placed on a frictional surface and allowed to collapse. The second, and much larger, example involving analysis of a collapsing slope.

### Chapter 6

This chapter presents conclusions and recommendations for future research.

# CHAPTER 2
# State of the art for the material-point method

This chapter presents the basic equations for the material-point method and discusses the state of the art of the method. A distinction is made between the original MPM formulation, where material points are integrated on the grid using Dirac's delta functions, and the GIMP formulation, where the material points are integrated using particle characteristic functions.

## 2.1 State of the art of the material-point method

The material-point method developed by Sulsky and coworkers (1994, 1995) is an extension of the fluid-implicit particle-method (FLIP) developed by Brackbill and Ruppel (1986). Further, the FLIP is an extension of the particle-in-cell method by Harlow (1964). In the later work by Sulsky and Schreyer (1996), an axisymmetric form of the equations is presented and the notion the *material point method* is introduced for the first time. More recently, a generalization of the method was presented by Bardenhagen and Kober (2004) called the generalized interpolation material point method (GIMP).

In the material-point method a continuum is considered. The continuum is subject to governing equations. Firstly, the balance of momentum is given by

$$\rho \frac{d\mathbf{v}}{dt} = \nabla \cdot \boldsymbol{\sigma} + \rho \mathbf{b}, \tag{2.1}$$

where $\rho = \rho(\mathbf{x}, t)$ is the current density, $\mathbf{v} = \mathbf{v}(\mathbf{x}, t)$ is the spatial velocity, $\boldsymbol{\sigma} = \boldsymbol{\sigma}(\mathbf{x}, t)$ is the Cauchy stress tensor and $\mathbf{b} = \mathbf{b}(\mathbf{x}, t)$ is the specific body force.

Secondly, conservation of mass involves that

$$\frac{d\rho}{dt} + \rho \nabla \cdot \mathbf{v} = 0, \tag{2.2}$$

where $\nabla$ is the gradient operator and $\nabla \cdot \mathbf{a}$ is the divergence of the vector field $\mathbf{a}$.

Finally, mechanical energy conservation is ensured by the equation

$$\rho \frac{dE}{dt} = \boldsymbol{\sigma} : \frac{d\boldsymbol{\varepsilon}}{dt} + \rho \mathbf{v} \cdot \mathbf{b}, \tag{2.3}$$

where $E$ is the internal energy per unit mass in the current configuration, $\boldsymbol{\varepsilon} = \boldsymbol{\varepsilon}(\mathbf{x}, t)$ is the strain and $d\boldsymbol{\varepsilon}/dt$ the corresponding strain rate.

In order to complete the description of the continuum, a constitutive law relating the strain rates and the stress rates of the material is needed. The strain rate can be determined from the equation

$$\frac{d\boldsymbol{\varepsilon}}{dt} = \frac{1}{2}\left(\nabla \mathbf{v} + (\nabla \mathbf{v})^T\right), \tag{2.4}$$

where superscript $T$ denotes the transpose. The stress depends on the type of material under consideration. A general linear-hyperelastic constitutive model or an incrementally linear elasto plastic model can be expressed as

$$\frac{d\boldsymbol{\sigma}}{dt} = \mathbf{D} : \frac{d\boldsymbol{\varepsilon}}{dt}, \tag{2.5}$$

where $\mathbf{D}$ is the fourth-order constitutive tensor.

A discretization technique similar to the one applied to the finite element method is applied. The balance of momentum, Eq. (2.1) is formulated in a weak form by multiplication by an arbitrary test function, $\mathbf{w}$, and integrating over the domain, yielding

$$\int_\Omega \rho \mathbf{w} \cdot \frac{d\mathbf{v}}{dt}\, dV = \int_\Omega \mathbf{w} \cdot \nabla \cdot \boldsymbol{\sigma}\, dV + \int_\Omega \rho \mathbf{w} \cdot \mathbf{b}\, dV. \tag{2.6}$$

Using the Green's divergence theorem, Eq. (2.6) can be reformulated as

$$\int_\Omega \rho \mathbf{w} \cdot \frac{d\mathbf{v}}{dt}\, dV = -\int_\Omega \boldsymbol{\sigma} : \nabla \mathbf{w}\, dV + \int_{\partial\Omega_\tau} \mathbf{w} \cdot \boldsymbol{\tau}\, dS + \int_\Omega \rho \mathbf{w} \cdot \mathbf{b}\, dV. \tag{2.7}$$

In order to arrive at a finite set of equations, the initial continuum domain, $\Omega$, of the physical problem is represented as a finite sum of material points, each representing part of the domain $\Omega_p$ with $p = 1, 2..., N_p$, where $N_p$ is the number of material points. The index $p$ is used for material points, while the index $i$ is reserved for denoting grid nodes. The material point $\mathbf{x}_p$ is defined at the centroid of the volume, $\Omega_p$. Further, at each time step a computational grid is formed of a finite set of grid points with coordinates $\mathbf{x}_i$, $i = 1, 2..., N_n$, where $N_n$ is the number of grid nodes. The discretization used in the material point method is illustrated in Figure 2.1.

### The original material-point method

Each material point is assigned initial values of position, velocity, mass, volume and stresses, denoted by $\mathbf{x}_p$, $\mathbf{v_p}$, $m_p$, $V_p$, $\boldsymbol{\sigma}_p$ as well as any other relevant variables associated with the specific material model. The problem is then integrated using a discrete number of time steps, $k = 1..N_t$, where $k$ is the current time step and $N_t$ is the number of time-steps. In Eq. (2.7) the density field is represented by material-point representations given by

$$\rho(\mathbf{x}, t) = \sum_{p=1}^{N_p} m_p \delta(\mathbf{x} - \mathbf{x}_p), \tag{2.8}$$

where $\delta$ is the Dirac's delta function. In order to discretize the first term of the left side of Eq. (2.7), a specific stress is defined by

$$\boldsymbol{\sigma}_s = \frac{\boldsymbol{\sigma}}{\rho} \tag{2.9}$$

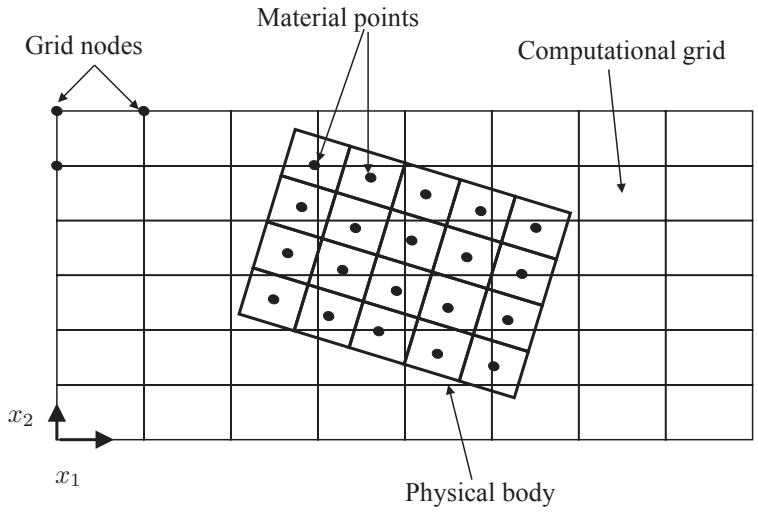


**Figure 2.1** Discretization used in the material-point method

and the term becomes

$$\int_\Omega \boldsymbol{\sigma} : \nabla \mathbf{w}\, dV = \int_\Omega \rho \boldsymbol{\sigma}_s : \nabla \mathbf{w}\, dV \tag{2.10}$$

Further, the spatial variation of the velocity and the test function fields is provided in the form

$$\mathbf{v}(\mathbf{x}, t) = \sum_{i=1}^{N_n} \mathbf{v}_i N_i(\mathbf{x}) \tag{2.11}$$

and

$$\mathbf{w}(\mathbf{x}, t) = \sum_{i=1}^{N_n} \mathbf{w}_i N_i(\mathbf{x}), \tag{2.12}$$

where $\mathbf{v}_i$ and $\mathbf{w}_i$ are the nodal velocity and test functions, respectively, while $N_i$ is the nodal shape function. Combining Eqs. (2.7), (2.8), (2.10), (2.11) and (2.12) and utilizing that the test functions are arbitrary yields

$$m_{ij}\mathbf{a}_j = \mathbf{f}_i^{int} + \mathbf{f}_i^{ext}. \tag{2.13}$$

Here $m_{ij}$ signifies the components of the mass matrix. In the case of consistent mass,

$$m_{ij} = \sum_{p=1}^{N_p} m_p N_{ip} N_{jp}, \tag{2.14}$$

in which the notation $N_{ip} = N_i(\mathbf{x}_p)$ is used. The vector of internal forces is given by

$$\mathbf{f}_i^{int} = \sum_{p=1}^{N_p} \nabla N_{ip} \boldsymbol{\sigma}_p^s m_p = \sum_{p=1}^{N_p} \nabla N_{ip} \boldsymbol{\sigma}_p V_p, \tag{2.15}$$

where $m_p = \rho_p V_p$. The vector of external forces is given by

$$\mathbf{f}_i^{ext} = \mathbf{b}_i + \boldsymbol{\tau}_i. \tag{2.16}$$

The first term is the external body forces, such as gravity, which is most naturally specified at the material points, in which case the body force vector is found by

$$\mathbf{b}_i = \sum_{p=1}^{N_p} m_p \mathbf{b}(\mathbf{x}_p) N_{ip}, \tag{2.17}$$

where $\mathbf{b}(\mathbf{x}_p)$ is the external acceleration associated with material point $p$. The second term of Eq. (2.17) is the traction at the boundary of the domain $\Omega$ and is generally evaluated by

$$\boldsymbol{\tau}_i = \int_{\partial\Omega_\tau} N_{ip} \boldsymbol{\tau}(\mathbf{x}) dS. \tag{2.18}$$

Finally, nodal velocities are found by solving

$$m_{ij} \mathbf{v}_j = \sum_{p=1}^{N_p} N_{ip} N_{jp} m_p \mathbf{v}_p \tag{2.19}$$

and the nodal velocities are utilized to find strain increments at the material points, based on the gradient of the grid velocity field. The strain increments at the material points are found by

$$\Delta\boldsymbol{\varepsilon}_p = \frac{\Delta t}{2} \sum_{i=1}^{N_n} \left( \nabla N_{ip} \mathbf{v}_i + (\nabla N_{ip} \mathbf{v}_i)^T \right). \tag{2.20}$$

Then the stress increments are found individually at each material point from an appropriate constitutive model.

In in the work by Sulsky et al. (1995) the above formulation is described as a consistent mass formulation. The corresponding lumped mass formulation is given by specifying

$$m_i \mathbf{a}_i = \mathbf{f}_i^{int} + \mathbf{f}_i^{ext}, \tag{2.21}$$

where

$$m_i = \sum_{p=1}^{N_p} N_{ip} m_p \tag{2.22}$$

and

$$\mathbf{v}_i = \frac{\sum_{p=1}^{N_p} N_{ip} m_p \mathbf{v}_p}{m_i}. \tag{2.23}$$

Most of the cited references of MPM, including this work, applies the lumped-mass formulation of Eqs. (2.21), (2.22) and (2.23) in order to allow a fast explicit time integration.

Finally, the velocity and position of the material points need to be updated. In the first publication on the MPM (Sulsky et al. 1994), the nodal acceleration is calculated and used to update the material points. Here the nodal velocity at the end of the time step is calculated as

$$\mathbf{v}_i^{k+1} = \mathbf{v}_i^k + \Delta t \mathbf{a}_i^k, \tag{2.24}$$

where the upper index, $k$, refers to the time step. The nodal acceleration is found by Eq. (2.21) and the updated velocity and position of the material points are found as

$$\mathbf{v}_p^{k+1} = \mathbf{v}_p^{k+1} + \Delta t \sum_{i=1}^{N_n} N_{ip}^k \mathbf{a}_i^k \tag{2.25}$$

and

$$\mathbf{x}_p^{k+1} = \mathbf{x}_p^k + \Delta t \sum_{i=1}^{N_n} N_{ip}^k \mathbf{v}_i^{k+1}. \tag{2.26}$$

However, this way of updating the velocity and position has been shown to be numerically unstable. This is due to that $\mathbf{f}_i^{int}$ can be finite for an infinitesimal nodal mass, $m_i$. This can lead to numerical problems when calculating the nodal acceleration applied in Eq. (2.24). Hence, a better, and mathematically equivalent, way of updating the material points is

$$\mathbf{v}_p^{k+1} = \mathbf{v}_p^k + \Delta t \sum_{i=1}^{N_n} \frac{N_{ip}^k (\mathbf{f}_i^{int,k} + \mathbf{f}_i^{ext,k})}{m_i^k} \tag{2.27}$$

and

$$\mathbf{x}_p^{k+1} = \mathbf{x}_p^k + \Delta t \sum_{i=1}^{N_n} \frac{N_{ip}^k \left( \mathbf{v}_i^k m_i^k + \Delta t (\mathbf{f}_i^{int,k} + \mathbf{f}_i^{ext,k}) \right)}{m_i^k}. \tag{2.28}$$

This formulation is first presented by Sulsky (1995). Due to the updated Lagrangian description using material points, mass conservation is always satisfied.

The equations (2.21), (2.22), (2.23), (2.27), (2.28) and (2.20) together with appropriate constitutive models constitute the basics of the material-point method. However, several choices exist in order to implement a reliable MPM code. It is noted that the MPM calculation procedure makes easy to implement constitutive response as each material point is evaluated separately.

One of the early benchmark examples of the MPM involves the collision of elastic discs. Figure 2.2 shows the setting of the problem. The problem is discretized using a grid of 10 by 10 cells using linear spatial interpolation and nine material points per cell. A total of 122 material points is used to represent each disc. The grid is fixed in time while the explicit time integration scheme is utilized to determine the configuration of material points as a function of time. A time increment of $\Delta t = 0.002$ and a total time of $T = 0.2$ is used. Figure 2.3 shows the position of the material points as a function of time. The collision occurs in a physically realistic fashion, although no contact law has been specified. The interaction of the two discs is numerically modelled by the requirement of a single valued nodal velocity field and single valued vector of internal forces at each grid node.

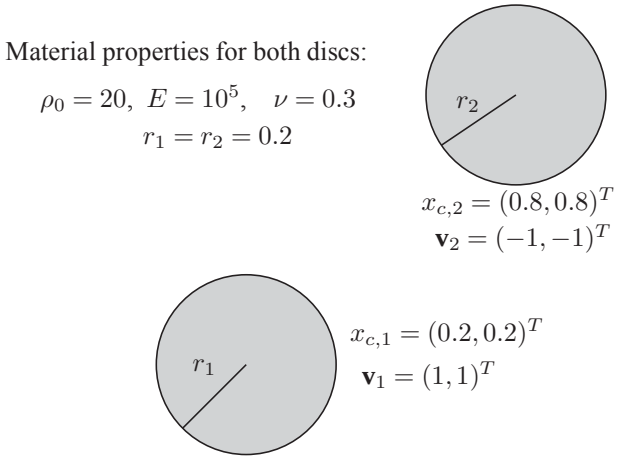


**Figure 2.2** The colliding discs problem

## Implementation choices for the material-point method

One choice in the implementation of the method regards when in the constitutive response is evaluated in the computational cycle. The initial formulation of MPM (Sulsky et al. 1994) evaluates the constitutive response after the calculation of internal force. This issue is discussed by Bardenhagen (2002) who shows that updating the stresses before the calculation of internal forces—"update stress first"—improves the robustness of the method compared to updating the stresses after the calculation of internal forces—"update stress last". The work by Buzzi et al. (2008) as well as Wallstedt and Guilkey (2008) further discusses this issue. The issue of when to update the stresses is discussed in detail in Chapter 4.

Another key issue is the actual choice of interpolation functions. As the operations in Eqs. (2.22), (2.23), (2.20), (2.27) and (2.28) all require mapping, this is essential. In the above presentation, the material-point quantities are represented spatially using Dirac's delta functions. This leads to the interpolation functions that are simply the nodal shape functions.

The initial implementations of the MPM employed linear shape functions for interpolation between the material points and the grid. However, for the usual case of a fixed grid, this leads to unphysical stresses oscillations, when a material switches cell between two time steps. The reason is found in the linear shape functions. As shown by Steffen, Wallstedt, Guilkey, Kirby, and Berzins (2008), interpolation using linear shape functions fails to provide spatial convergence due to this effect, also known as the grid crossing error. The errors associated with the interpolations are analysed by Wallstedt and Guilkey (2007) for different configurations of material points and grid nodes.

An approach to obtain better results is to apply higher order nodal shape functions within the framework of the original MPM formulation. This approach is explored by Steffen and co-workers (Steffen, Wallstedt, Guilkey, Kirby, and Berzins 2008; Steffen, Kirby, and Berzins 2008) and in Paper I of this thesis. The most promising results are obtained using cubic splines as interpolation functions. Steffen, Wallstedt, Guilkey, Kirby, and Berzins (2008) show that for simple problems, the use of cubic splines improves the spatial convergence properties of method as grid-crossing errors are reduced. Further, Paper I shows that cubic splines improve

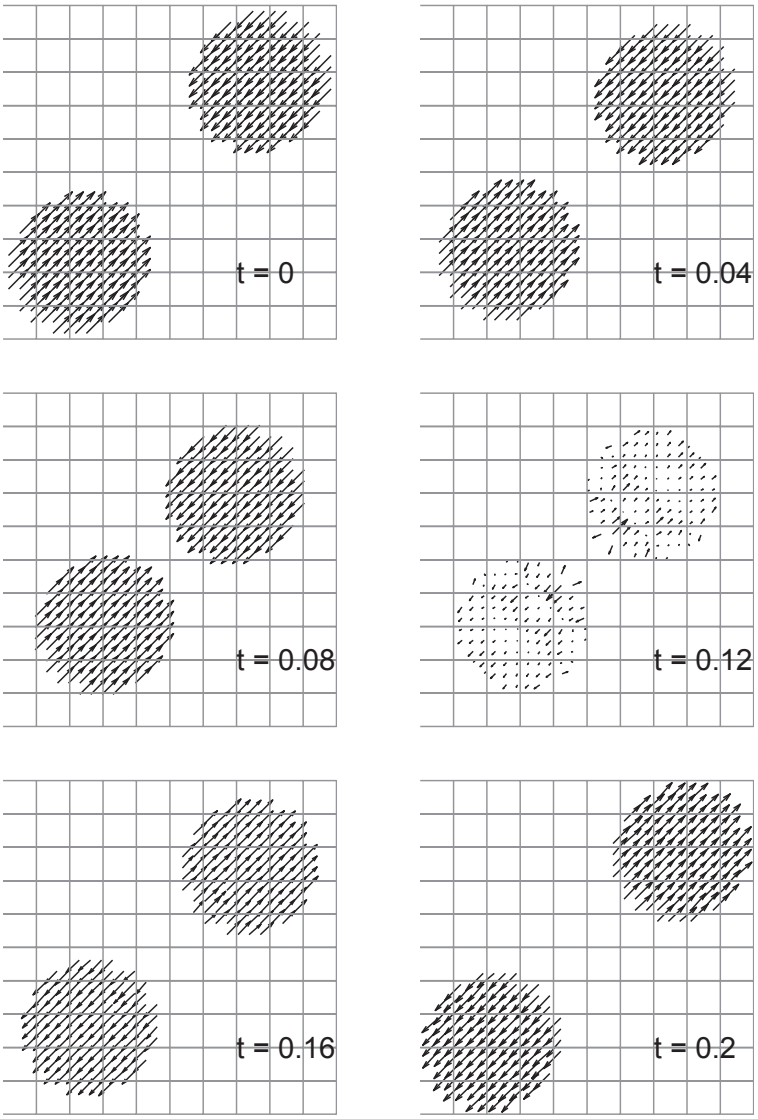


**Figure 2.3** Position and velocity field of material points as a function of time.

the representation of stresses at the individual material points. One problem with the cubic-spline interpolation, however, is that the support of a material point enlarged, i.e. the domain where the interpolation function is non-zero. This necessitates a finer discretization in terms of number of

grid nodes and material points, in order to maintain the same behaviour.

Another approach is to represent the material using particle characteristic functions, $\chi_p$, when deriving the discrete momentum equation. This approach, described in the work by Bardenhagen and Kober (2004), is called the generalized interpolation material point method (GIMP). It leads to a system of equations identical to (2.21), (2.22), (2.23), but where the interpolation functions that map between the mesh and material points are integrals over the domain of the particle characteristic functions

$$\Phi_{ip} = \frac{1}{V_p} \int_{\Omega_p \bigcap \Omega} \chi_p(\mathbf{x} - \mathbf{x}_p) N_i(\mathbf{x}) \, d\mathbf{x}, \tag{2.29}$$

where $\Phi_{ip} = \Phi_i(\mathbf{x}_p)$.

The generalization from MPM can identified by specifying

$$\chi_p(\mathbf{x} - \mathbf{x}_p) = \delta(\mathbf{x} - \mathbf{x}_p) V_p, \tag{2.30}$$

in which case the formulation is equivalent to the original MPM formulation. Bardenhagen and Kober shows that the GIMP formulation reduces the so called grid-crossing error as the particle characteristic function has the effect of smoothing the nodal shape functions. The most commonly employed particle characteristic function is constant within the volume of the material point. The difference in results when modelling using the MPM and the GIMP are easily visualized in terms of the stress fields. Chapter 4 presents examples, where the GIMP formulation is compared with the original MPM formulation.

For most implementations the grid is usually fixed in time, while the material points move and deform. For deformed configurations of material points, evaluation of the integral in Eq. (2.29) is non trivial. Hence, the deformations of volumes represented by the material points are typically not taken into account when evaluating the integral. In Section 3.3 a way of numerically evaluating the integral of Eq. (2.29) is presented for a constant particle characteristic function, corresponding to integrating over the deformed volume of the material.

In the example of the colliding discs, the collision occurs as physically expected, although the equations were formulated for one continuum, $\Omega$. The two approaching discs lead to compressive strain increments, driving the collision. However, for other geometries of collisions, where the area of contact is larger compared to the volume of the continua, this approach has shortcomings. In more general cases the bodies seem to unrealistically stick to each other after contact. In the work by York et al. (1999, 2000) an important refinement of the method for modelling the interaction of two or more continua is presented. The idea is to define a nodal velocity field by Eq. (2.23) individually for each of the bodies. Normal vectors associated with each continuum are calculated based on the gradients of the density fields for nodes shared by two continua. When two continua are approaching, the updates (2.20), (2.27) and (2.28) are performed for the entire system, but when two continua depart the updates are done for each continuum individually.

This idea is utilized in the work by Bardenhagen et al. (2000a, 2000b) to formulate frictional conditions between multiple continua. The algorithm is utilized to study shearing mechanics for granular materials. This algorithm is utilized by Coetzee et al. (2005) to model the capacity of soil anchors and bucket excavator filling (2006) while Hu and Chen (2003) employs this model to simulate the meshing process for spurning gears. In the work by Bardenhagen et al. (2001) the algorithm for frictional contact is improved, such that contact is now defined when the normal

tractions are negative, corresponding to compression. The frictional contact is implemented by changing the velocities of the shared grid nodes according to the frictional law. In Paper III this algorithm is employed to model the slip between sand and clay that lead to the landslide at Rubjerg Knude.

A special case of material friction is that, in which one of the continua has a regular geometry and is subject to negligible deformations. In such cases, the frictional contact law can be implemented as a boundary condition. A frictional boundary model, implemented for analysis of a silo discharging problem is presented by Wieckowski et al. (1999, 2004). A penalty regularization method is employed in the determination of the frictional forces.

Another active area of discussion is whether to use explicit or implicit time-integration. The initial implementations of MPM all used explicit time integration. However, several studies of applying implicit time integration to the material-point method is presented in the literature, for instance Cummins and Brackbill (2002), Guilkey and Weiss (2003), Sulsky and Kaul (2004). Love and Sulsky (2006b) present an MPM scheme with implicit energy and momentum conserving mesh dynamics for hyperelastic material and the same authors propose an algorithm for finite deformation plasticity (Love and Sulsky 2006a).

The work by Shen and Chen (2005) presents an algorithm for realistic modelling of boundary conditions for finite parts of larger domains using transmitting boundary conditions.

### 2.1.1 Applications of the MPM

One important application of the MPM is the modelling of discontinuities such as cracks, decohesion and delamination. Schreyer et al. (2002) describes application of the material-point method to model delamination using a strong discontinuity approach. In the work by Sulsky and Schreyer (2004) delamination is modelled using a decohesive constitutive model. Another application in modelling localized deformation is performed by Chen et al. (2002). Tan and Nairn (2002), Nairn (2003) and Guo and Nairn (2004) explore a crack-closure model for the MPM. A model for crack growth within the content of the GIMP is presented by Daphalapurkar et al.(2007) employing a cohesive zone model.

The modelling of hypervelocity impact problems and explosions is another applications, where the material point model is employed due to its ability to represent large strains. A study of hyper-velocity impact problems is performed by Zhang et al. (2006). The work by Ma et al. (2009) compares the performance of the MPM against smoothed particle hydrodynamics (SPH). The material-point method is shown superior due to the automatic modelling of contact in the MPM and the problem of tensile instability in SPH. A similar application is presented by Hu and Chen (2006) who study synergistic effects of blasts and fragmentation on a concrete wall using the MPM. Guilkey et al. (2007) describe the simulation of explosions of energetic devises.

Another application is the micromechanical modelling of materials. The work by Shen et al. (2000) analyses localization of plastic deformation along grain boundaries in a hardening material. Densification of open-cell foam microstructures is modelled with the GIMP is presented by Brydon et al. (2005).

Another research area is the implementation of the MPM to large scale parallel computing. The work by Ma and coworkers (2005, 2006) deals with structured mesh refinement for large scale problems.

A recent idea is to combine the material-point method with other numerical methods for the study of specialized problems. In the work by Gilmanov and Acharya (2008), fluid-structure

interaction is analysed with a combination the material-point method to represent the structure combined with the hybrid immersed boundary method (HIMB) to represent the fluid. The work of Guo and Yang (2006) utilizes a combination of the MPM and molecular dynamics (MD) in order to study high energy cluster impacts. The continuum part the problem is modelled by the MPM while the individual atoms are represented by molecular dynamics.

Within the field of geotechnical engineering, Zhou et al. (1999) applies the material-point method in a quasi-static form to study geo-membrane response to settlement of landfills. Of special interest for landslide modelling is the implementation of two-phase models for saturated porous media. Zhang et al. (2009) describes a u-p form of the governing equations in which the state variables for the fluid phase are defined at the material points. The algorithm consist of firstly updating the displacement of the multi-phase medium and then calculating the change in pore pressure. The interface between the coupled soil and the foundation structures are modelled by a Coulomb friction law.

## 2.2 The generalized interpolation material point method

The generalized interpolation material point method, firstly presented by Bardenhagen and Kober (2004), is a generalization of the material-point method. The generalization involves how material points are utilized to obtain the governing equations. In the initial formulation of the material-point method by Sulsky et al. (1995), as given above, the material points are represented spatially using the Dirac delta function. In the GIMP, a particle characteristic function, generally of a finite extent, is defined for each material point. In the work of this thesis, a formulation is presented, where the particle characteristic function is defined as a constant within the volume associated with each material point.

Firstly, it is shown that the GIMP formulation leads to a system of equations similar to Eq. (2.21). The governing equation to discretize is Eq. (2.7), repeated here

$$\int_\Omega \rho \mathbf{w} \cdot \frac{d\mathbf{v}}{dt}\, dV = -\int_\Omega \boldsymbol{\sigma} : \nabla \mathbf{w}\, dV + \int_{\partial\Omega_\tau} \mathbf{w} \cdot \boldsymbol{\tau}\, dS + \int_\Omega \rho \mathbf{w} \cdot \mathbf{b}\, dV. \tag{2.7}$$

In order to discretize Eq. (2.7), the domain is represented by a finite set of material volumes. The initial domain $\Omega^0$ is divided into a set of non-overlapping subdomains $\Omega_p^0$, where $p = 1, 2, ..., N_p$ and $N_p$ is the number of material volumes. At the centroid of each subdomain, a material point with the coordinates $\mathbf{x}_p$ is defined. In order for clarity, $\Omega_p^0$ denotes the initial domain while the volume of this domain is denoted $V_p^0$. Hence, given an initial density field $\rho^0(\mathbf{x})$, the initial volume and the mass associated with material point $p$ is given by

$$V_p^0 = \int_{\Omega_p^0} dV \tag{2.31}$$

and

$$m_p = \int_{\Omega_p^0} \rho^0(\mathbf{x})\, dV, \tag{2.32}$$

respectively, whereas

$$\rho_p^0 = \frac{m_p}{V_p^0} \tag{2.33}$$

is introduced as the density of material point $p$ in the initial configuration.

The velocity and stress associated with a material point are defined as volume-weighted quantities, i.e.

$$\mathbf{v}_p = \frac{1}{V_p^0}\int_{\Omega_p^0} \mathbf{v}(\mathbf{x})dV \tag{2.34}$$

and

$$\boldsymbol{\sigma}_p = \frac{1}{V_p^0}\int_{\Omega_p^0} \boldsymbol{\sigma}(\mathbf{x})dV. \tag{2.35}$$

Similarly, external body forces are defined by

$$\mathbf{b}_p = \frac{1}{V_p^0}\int_{\Omega_p^0} \mathbf{b}(\mathbf{x})dV. \tag{2.36}$$

Although associated with the material volumes, the quantities defined by Eqs. (2.31) to (2.36) will, in accordance with existing MPM articles, be referred to as material-point quantities.

In order to obtain a discrete spatial representation, particle characteristic functions, $\chi_p$, associated with the material points are defined. The particle characteristic functions are defined such that they are a partition of unity in the reference configuration, i.e.

$$\sum_{p=1}^{N_p} \chi_p^0(\mathbf{x}) = 1 \;\forall\, \mathbf{x}. \tag{2.37}$$

Further, the particle characteristic functions are normalized with respect to the initial volume, i.e.

$$\int_{\Omega^0} \chi_p(\mathbf{x},t)dV = V_p^0. \tag{2.38}$$

It is noted, that the original MPM formulation is obtained by setting $\chi_p = \delta(\mathbf{x}-\mathbf{x}_p)$, where $\delta$ is the Dirac delta function. The material point quantities defined in Eqs. (2.32) to (2.36) are used to approximate the fields for the momentum, the body forces and stresses in the balance of momentum, respectively. Field quantities are represented as sums over the material points, i.e.

$$f(\mathbf{x}) = \sum_{p=1}^{N_p} f_p \chi_p(\mathbf{x}). \tag{2.39}$$

For instance, the first term in the balance of momentum is represented by

$$\rho\frac{d\mathbf{v}}{dt} \cong \sum_{p=1}^{N_p} \rho_p \frac{d\mathbf{v}_p}{dt}\chi_p(\mathbf{x}) = \sum_{p=1}^{N_p} \frac{m_p}{V_p}\frac{d\mathbf{v}_p}{dt}\chi_p(\mathbf{x}). \tag{2.40}$$

Using the material-points representation in the balance of momentum yields

$$\sum_{p=1}^{N_p} \frac{m_p}{V_p}\int_{\Omega_p} \mathbf{w}\cdot\frac{d\mathbf{v}_p}{dt}\chi_p\, dV = \int_{\partial\Omega_\tau} \mathbf{w}\cdot\boldsymbol{\tau}\, dS - \sum_{p=1}^{N_p} \boldsymbol{\sigma}_p : \int_{\Omega_p} \frac{\partial \mathbf{w}}{\partial \mathbf{x}}\chi_p\, dV$$

$$+\sum_{p=1}^{N_p} \frac{m_p \mathbf{b}_p}{V_p} \int_{\Omega_p} \mathbf{w}\chi_p \, dV. \tag{2.41}$$

The term on the left hand side represents the rate of change of momentum. On the right hand side the first term represents the surface tractions, the second term represents internal forces due to stress gradients while the last term represents external body forces. Further, it is noted that the physical quantities are evaluated at each material point.

Now approximations for the field of test functions are made in terms of the background grid. The geometry of the grid is defined by $N_n$ nodes, using the index $i = 1, ..., N_n$ exclusively to identify the nodes. Between the nodes, the test functions are represented continuously by means of shape functions by

$$\mathbf{w}(\mathbf{x}) \cong \sum_{i=1}^{N_n} \mathbf{w}_i N_i(\mathbf{x}), \tag{2.42}$$

while the gradients of the test function are represented by

$$\frac{\partial \mathbf{w}(\mathbf{x})}{\partial \mathbf{x}} \cong \sum_{i=1}^{N_n} \mathbf{w}_i \frac{\partial N_i(\mathbf{x})}{\partial \mathbf{x}}. \tag{2.43}$$

As for the particle characteristic function, the nodal shape functions are required to be a partition of unity, i.e.

$$\sum_{i=1}^{N_n} N_i(\mathbf{x}) = 1 \; \forall \; \mathbf{x}, \; \mathbf{x} \in \Omega_c, \tag{2.44}$$

where $\Omega_c$ is the computational domain.

Employing Eqs. (2.42) and (2.43), the balance of momentum can be written as

$$\sum_{i=1}^{N_n} \mathbf{w}_i \cdot \left( \sum_{p=1}^{N_p} m_p d\mathbf{v}_p/dt \frac{1}{V_p} \int_{\Omega_p \bigcup \Omega_i} N_i \chi_p dV \right) = \sum_{i=1}^{N_n} \mathbf{w}_i \cdot \left( \int_{\partial\Omega_\tau} N_i \tau dS) \right)$$

$$- \sum_{i=1}^{N_n} \mathbf{w}_i \cdot \left( \sum_{p=1}^{N_p} \int_{\Omega_p \bigcup \Omega_i} \boldsymbol{\sigma}_p \cdot \frac{\partial N_i}{\partial \mathbf{x}} \chi_p dV \right) + \sum_{i=1}^{N_n} \mathbf{w}_i \cdot \left( \sum_{p=1}^{N_p} m_p \mathbf{b}_p \frac{1}{V_p} \int_{\Omega_p \bigcup \Omega_i} N_i \chi_p dV \right), \tag{2.45}$$

where $\Omega_i$ is the domain where $N_i$ is nonzero.

Now, the weighting and the gradient weighting function are introduced as

$$\bar{N}_{ip} = \frac{1}{V_p} \int_{\Omega_p \bigcup \Omega} N_i \chi_p dV \tag{2.46}$$

and

$$\frac{\partial \bar{N}_{ip}}{\partial \mathbf{x}} = \frac{1}{V_p} \int_{\Omega_p \bigcup \Omega} \frac{\partial N_i}{\partial \mathbf{x}} \chi_p dV. \tag{2.47}$$

Utilizing that the test functions $\mathbf{w}_i$ are arbitrary, the system of equations need to be satisfied at all grid nodes. Employing Eqs. (2.46) and (2.47) in Eq. (2.45) yields

$$\sum_p m_p \frac{d\mathbf{v}_p}{dt} \bar{N}_{ip} = \int_{\partial\Omega_\tau^0} N_i \boldsymbol{\tau} dS - \sum_p \boldsymbol{\sigma}_p V_p \frac{\partial \bar{N}_{ip}}{\partial \mathbf{x}} + \sum_p m_p \mathbf{b}_p \bar{N}_{ip}. \tag{2.48}$$

Rewriting the balance of momentum yields

$$m_i \frac{d\mathbf{v}_i}{dt} = \mathbf{f}_i^{int} + \mathbf{f}_i^{ext}, \tag{2.49}$$

where

$$m_i \frac{d\mathbf{v}_i}{dt} = \sum_p m_p \frac{d\mathbf{v}_p}{dt} \bar{N}_{ip} \tag{2.50}$$

is the nodal momentum rate of change,

$$\mathbf{f}_i^{int} = -\sum_p \boldsymbol{\sigma}_p V_p \frac{\partial \bar{N}_{ip}}{\partial \mathbf{x}} \tag{2.51}$$

is the internal force and

$$\mathbf{f}_i^{ext} = \int_{\partial\Omega_\tau} N_i \boldsymbol{\tau} dS + \sum_p m_p \mathbf{b}_p \bar{N}_{ip} \tag{2.52}$$

is the external force. Comparing Eq. (2.49) with Eq. (2.21) its is seen that the GIMP formulation leads to a system of equations almost identical to the MPM equations, only now the governing equation is assembled using the weighting function $\bar{N}_{ip}$. As the mass is carried by the material points, the conservation of mass is automatically satisfied.

### 2.2.1 Explicit time-integration approach

In the material-point method, the basic idea is to solve the balance on the grid and then use the information to update the quantities associated with the material points. The mass and momentum at grid node $i$ are found by

$$m_i^k = \sum_{p=1}^{N_p} m_p^k \bar{N}_{ip} \tag{2.53}$$

and

$$m_i^k \mathbf{v}_i^k = \sum_{p=1}^{N_p} \mathbf{v}_p^k m_p \bar{N}_{ip}, \tag{2.54}$$

respectively.

The position and the velocity update for the material points are given by

$$\mathbf{x}_p^{k+1} = \mathbf{x}_p^k + \Delta t \sum_{i=1}^{N_n} \bar{N}_{ip} \frac{m_i^k \mathbf{v}_i^k + \Delta t(\mathbf{f}_i^{int,k} + \mathbf{f}_i^{ext,k})}{m_i^k} \tag{2.55}$$

and

$$\mathbf{v}_p^{k+1} = \mathbf{v}_p^k + \Delta t \sum_{i=1}^{N_n} \bar{N}_{ip} \frac{(\mathbf{f}_i^{int,k} + \mathbf{f}_i^{ext,k})}{m_i^k}. \tag{2.56}$$

A simple MPM/GIMP algorithm using explicit time-integration can be given as

**1** Initialisation of material properties at the material points at time $t^k = 0$.

**2** At each time step:

- A background computational grid is generated,
- the shape/weighting and the gradient shape/weighting functions are determined,
- masses and velocities at the grid nodes is found,
- stresses and strain increments are determined,
- calculate internal and external forces,
- the position and the velocity of the material points are found.

Section 2.1 and Section 2.2 constitute the basis of the MPM/GIMP theory. The next chapter contains a detailed description of the implementation in this work and the work carried out in order to refine the method.

# CHAPTER 3
# Large strain formulation for the material-point method

This chapter presents several new ideas for the generalized material point method. Firstly, visualization of the results is discussed. Secondly, a new approach for tracking large deformations using the deformation gradient tensor is presented.

## 3.1 Presentation and visualization of results

Chapter 2 presents the governing equations for the material-point method as well as the generalized interpolation material point method. In order to verify results obtained by integrating the equations in time, some visualizations need to be performed. In the finite element method, the mesh tracks the deformation. Hence, the domain to visualize is well defined in the FEM. The work of Zienkiewicz and Taylor (2005) show finite element visualizations involving analysis of an arc dam in a mountainous region. The work by Babuška and Miller (1984) presents several approaches for visualizing results from finite-element analysis with particular emphasis on stresses. In the material-point method, important quantities to visualize typical engineering problems are displacements, strains, stresses etc. In the finite-element analysis, the displacements are determined at the nodes, while stresses and strains typically are determined at Gauss points. Typically, the stresses and strains at the Gauss points are utilized to obtain more smooth stress distribution. For instance, Abaqus Version 6.8 (Dassault Systèmes 2008) allows for extrapolation of integration point quantities to the nodes or interpolation of integration point quantities to the centroid of an element.

In the initial articles involving the material-point method, for instance (Sulsky et al. 1994; Sulsky et al. 1995; Sulsky and Schreyer 1996), several numerical benchmark examples are presented. Common for the examples in these articles is that the visualization of the results is limited to showing the configuration of the material point coordinates as a function of time. For the case of the colliding discs, presented in Section 2.1, the position of material points as a function of time is shown in Figure 3.1. Compared to the finite-element method, the material points in the MPM caries all the information and the material moves relatively to the grid. This preclude using the grid to visualize the deformations of the material, as is typically performed in the finite element analysis.

An alternative way to visualize the results of two-dimensional MPM simulations is to associate an area with each material point. One simple implementation involves assuming a rectangular area for each material point. Using this, it is possible to illustrate different state variables

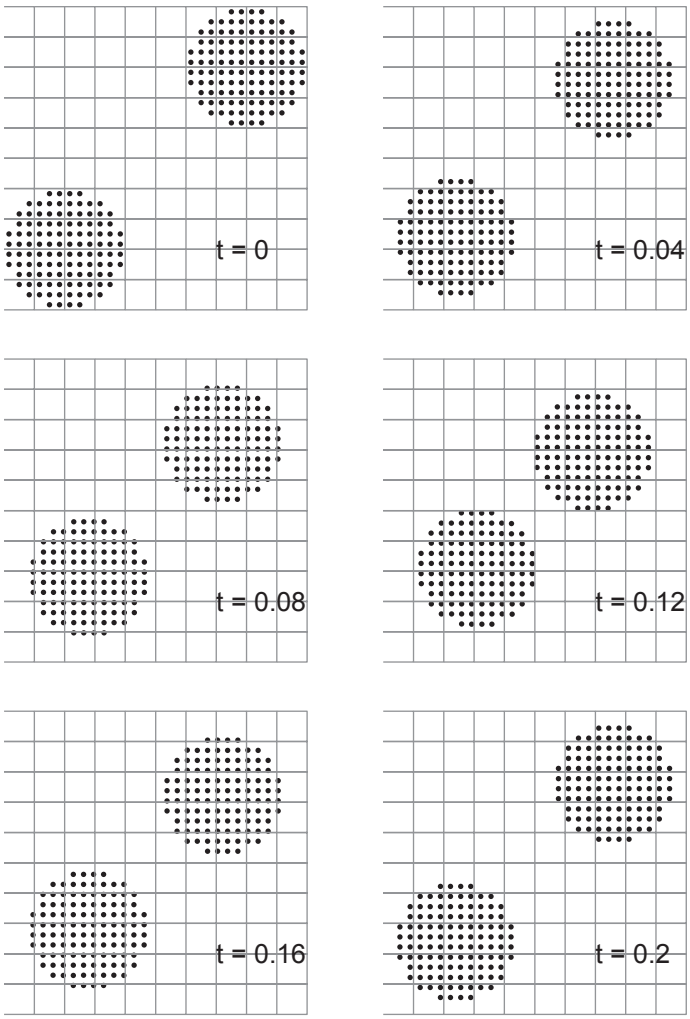


**Figure 3.1** Collision of elastic discs. The figure shows the position of material points as a function of time.

using colour plots. Figure 3.2 shows the horizontal velocity as a function of time for each material point. Here, the geometry is defined satisfactory by only associating a rectangle, with a size that is fixed in time, by each material point.

Another case is the collision of discs with elasto-plastic material properties. The two discs are modelled by a Tresca material model with the cohesion $c = 5$. The Mohr-Coulomb model presented in Section 5.2 is an extension of the Tresca model allowing also for frictional material behaviour. Further, a finer discretization using 896 material points is employed. Figure 3.3 shows

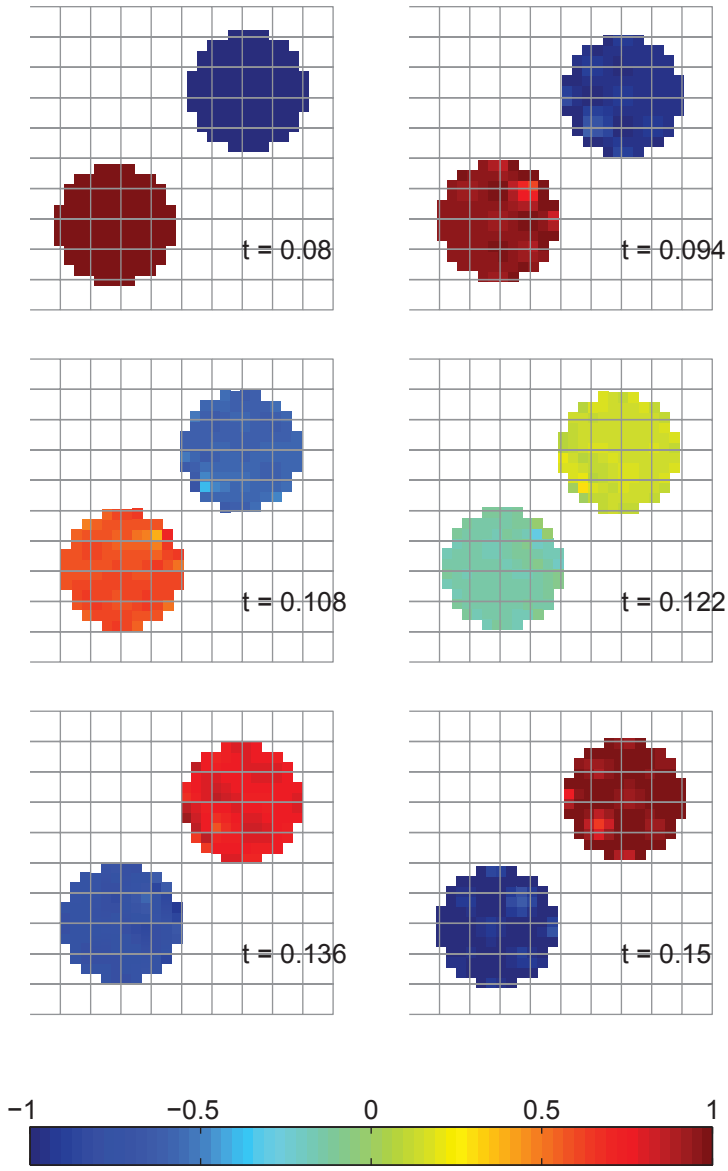


**Figure 3.2** By defining an area associated with each material point, it is possible to gain better visualization. The figure shows the horizontal velocity before, during and immediately after the impact.

the horizontal velocity of the discs during the impact

As observed, the initial momentum causes a significant plastic deformation such that the two discs stick after the impact. Another thing to observe is that the visualization using rectangles with sizes, that are fixed in time, is not completely adequate for capturing the nature of the

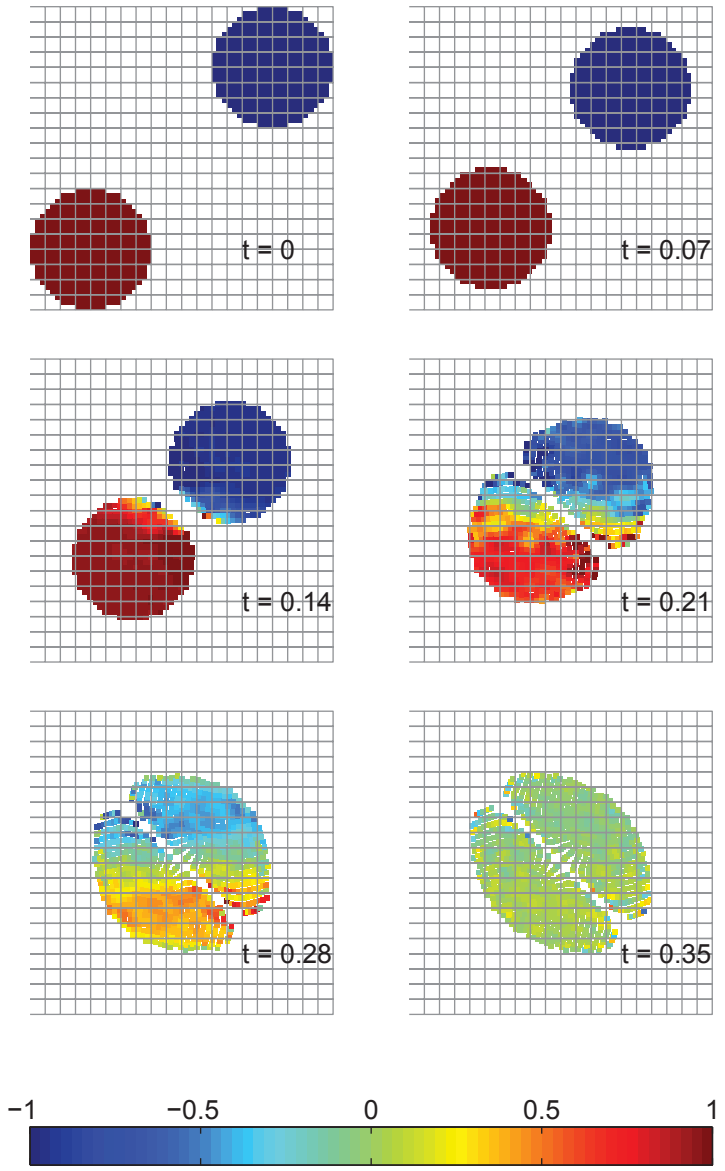


**Figure 3.3** Horizontal velocity as a function of time for the collision of two elasto plastic discs.

deformation.

## 3.2 Tracking large deformations

A logical extension of the visualization can be obtained by tracking the deformation of the areas associated with each material point. The geometric area associated with a material point is the given the notion *voxel*. In the reference configuration, the voxel is defined such that $V_p$ corresponds to the size of the voxel. The voxel notion is introduced by Steffen, Kirby, and Berzins (2008). The location of the corners associated with each voxel at a deformed state is specified through the deformation-gradient tensor which needs to be tracked through the simulation.

Utilizing this concept, a deformation gradient is associated with each material point in the current state as

$$\mathbf{F}_p = \frac{\partial \mathbf{x}_p}{\partial \mathbf{x}^0} = \frac{1}{V_p^0} \int_{\Omega_p^0} \mathbf{F}(\mathbf{x})\, dV. \tag{3.1}$$

In the initial configuration, the deformation gradient tensor is known. Typically, an undeformed material state will be prescribed, i.e. $\mathbf{F}^0 = \mathbf{I}$, where $\mathbf{I}$ is the identity tensor. An explicit forward difference updating scheme for updating the deformation gradient is employed,

$$\mathbf{F}^{k+1} = \Delta\mathbf{F}^{k+1}\mathbf{F}^k. \tag{3.2}$$

Expressing the time derivative of the deformation gradient as $\frac{\partial \mathbf{F}}{\partial t}\big|_{t=t^k} = \frac{\partial \mathbf{v}^k}{\partial \mathbf{x}^0}$, $\Delta\mathbf{F}^k$ can be expressed as

$$\Delta\mathbf{F}^{k+1} = \mathbf{I} + \Delta t \frac{\partial \mathbf{v}^k}{\partial \mathbf{x}^0}. \tag{3.3}$$

This corresponds to a first order MacLaurin expansion of the deformation gradient around $t^k$.

Using the nodal shape functions, the change in deformation gradient at an arbitrary point $\mathbf{x}$ can be evaluated as

$$\Delta\mathbf{F}^{k+1}(\mathbf{y}) = \mathbf{I} + \Delta t \sum_{i=1}^{N_n} \mathbf{v}_i^k \left.\frac{\partial N_i^k(\mathbf{x})}{\partial \mathbf{x}}\right|_{\mathbf{x}=\mathbf{y}}. \tag{3.4}$$

By use of the particle characteristic function, the increment of the deformation gradient can be formulated as

$$\Delta\mathbf{F}_p^{k+1} = \mathbf{I} + \Delta t \sum_{i=1}^{N_n} \mathbf{v}_i^k \frac{\partial \bar{N}_{ip}}{\partial \mathbf{x}}. \tag{3.5}$$

This way of integrating the deformation gradient, using the grid velocities, is also employed by Guilkey and Weiss (2003) and Love and Sulsky (2006b).

Here, it is presumed that the deformation of the voxel associated with the material point is uniform determined by the deformation gradient tensor. This concept is illustrated in Figure 3.4.

The tracking of the deformation gradient tensor can be applied to provide a better visualization of problems involving large strains. Considering a voxel associated with a material point initially located at $\mathbf{x}_p^0$, the coordinate for a corner in the initial configuration can be written as

$$\mathbf{x}_C^0 = \mathbf{x}_p^0 + d\mathbf{x}^0, \tag{3.6}$$

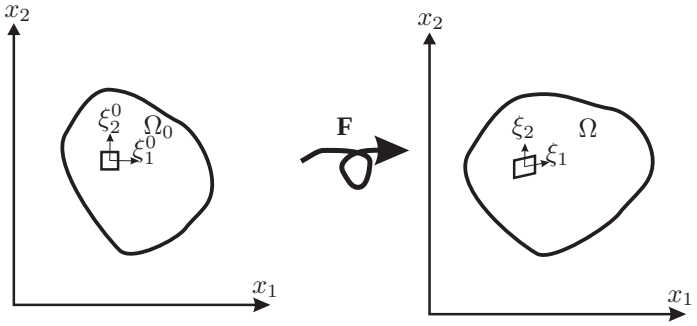


**Figure 3.4** Tracking the voxel associated with a material point through the deformation gradient tensor, **F**. The local coordinates $(\xi_1, \xi_2)^T$ determines the deformation of the voxel.

where $\mathbf{x}_C^0$ is the location of the corner and $d\mathbf{x}^0$ is the line segment between the material point and the corner. At an arbitrary time the location of the corner is given as

$$\mathbf{x}_C^t = \mathbf{x}_p^t + d\mathbf{x}. \tag{3.7}$$

Using the deformation gradient, defined at the material point, the line segment can be calculated by

$$d\mathbf{x} = \mathbf{F} d\mathbf{x}^0, \tag{3.8}$$

where $d\mathbf{x}^0$ is the deformed line segment and **F** is the deformation-gradient tensor defined in the local coordinate system $(\xi_1, \xi_2)^T$ by

$$\mathbf{F}^{local} = \frac{\partial \boldsymbol{\xi}}{\partial \boldsymbol{\xi}^0} \tag{3.9}$$

Using the chain rule, the deformation gradient tensor in the global coordinate system becomes

$$\mathbf{F} = \frac{\partial \mathbf{x}}{\partial \boldsymbol{\xi}} \frac{\partial \boldsymbol{\xi}}{\partial \boldsymbol{\xi}^0} \frac{\partial \boldsymbol{\xi}^0}{\partial \mathbf{x}^0}, \tag{3.10}$$

where the coordinate-systems are defined on Figure 3.4. In the presented examples, the initial local axes are chosen along the global coordinate system. Hence, in this case

$$\frac{\partial \mathbf{x}}{\partial \boldsymbol{\xi}} = \mathbf{I} \quad \text{and} \quad \frac{\partial \mathbf{x}_0}{\partial \boldsymbol{\xi}_0} = \mathbf{I} \tag{3.11}$$

Hence, when the local voxel coordinates are coincident with the global coordinate system, the deformation gradient tensor reduces to

$$\mathbf{F} = \frac{\partial \boldsymbol{\xi}}{\partial \boldsymbol{\xi}^0}. \tag{3.12}$$

Figure 3.5 shows how the tracking of the deformation gradient tensor can be applied to provide a better representation of the deformation in the example of the colliding plastic discs. As seen by comparing Figures 3.3 and 3.5, the tracking of the deformed geometry provides a better visualisation of the deformation.

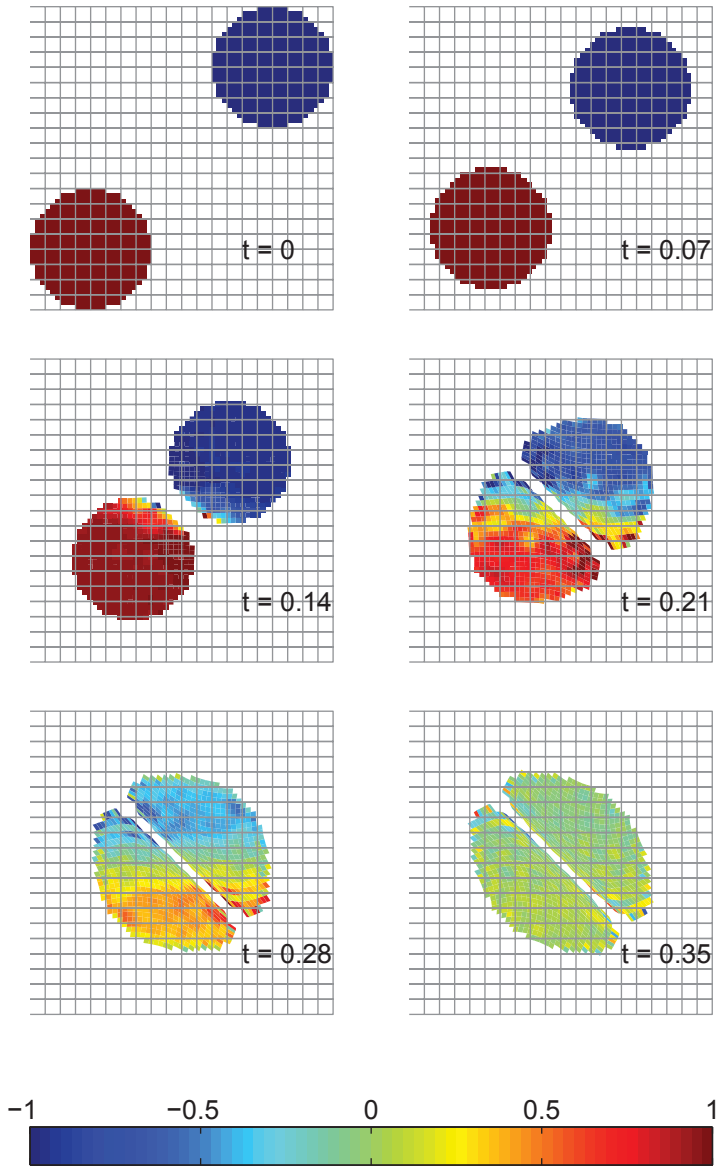


**Figure 3.5** Tracking of the deformed geometry for each material point. Horizontal velocity as a function of time for the collision of two elasto plastic discs.

## 3.3 Large strain analysis by the material point method

As shown in several references, the application of the GIMP significantly improves the performance of the material-point method. The GIMP generalization involves associating a particle

characteristic function with each material point instead of a Dirac delta function as applied in the original MPM formulation. As shown in Section 2.2, this leads to a system of equations similar to the lumped mass formulation of MPM. However, the interpolation is now defined by weighting functions. The most applied GIMP implementation and the one used in Paper II involves defining a volume associated with each material point. The particle characteristic function is defined as a constant within this volume. In Paper II a particle characteristic function associated undistorted volume of the material point is employed. This utilizes the fact, that when the voxel associated with the material point is a rectangle aligned with the global coordinate system, the weighting functions can be determined analytically. A constant particle characteristic function may mathematically be written as

$$\chi_p(\mathbf{x}_p) = \begin{cases} 1 & \text{if} \quad \mathbf{x} \in \Omega_p \\ 0 & \text{otherwise.} \end{cases} \tag{3.13}$$

The weighting and gradient weighting functions are determined by Eqs. (2.46) and (2.47). The constant particle characteristic function has the advantage that it integrates over the voxel associated with the material point. This leads to smoother representations of field quantities.

In a one dimensional case, where the length associated with a material point is $2l_p$ and the distance between grid nodes is $L$, the weighting function between material point $p$ and grid node $i$ is given by

$$\bar{N}_{ip}^{1D} = \begin{cases} 0 & x_p - x_i \leq -L - l_p \\ \frac{(L+l_p+(x_p-x_i))^2}{4Ll_p} & -L - l_p < x_p - x_i \leq -L + l_p \\ 1 + \frac{x_p - x_i}{L} & -L + l_p < x_p - x_i \leq -l_p \\ 1 - \frac{(x_p-x_i)^2+l_p^2}{2Ll_p} & -l_p \leq x_p - x_i \leq l_p \\ 1 - \frac{x_p - x_i}{L} & l_p < x_p - x_i \leq L - l_p \\ \frac{(L+l_p-(x_p-x_i))^2}{4Ll_p} & L - l_p < x_p - x_i \leq L + l_p \\ 0 & L + l_p < x_p - x_i. \end{cases} \tag{3.14}$$

For more dimensions, the weighting functions can be determined by products of the one dimensional weighting function. For the two-dimensional case with a rectangular material-point voxel aligned with the global coordinate system $(x_1, x_2)$, the weighting function can be determined by

$$\bar{N}_{ip}(\mathbf{x}) = \bar{N}_{ip}^{1D}(x_1)\bar{N}_{ip}^{1D}(x_2) \tag{3.15}$$

Figure 3.6 shows a one dimensional weighting function and a two dimensional weighting function where $l_p = 1/4L$. For physical problems involving finite rotations and deformations, the analytically evaluated GIMP weighting functions Eqs. (3.14) and (3.15) can no longer be applied to determine the weighting functions exactly. Two approaches are suggested to avoid this shortcoming. The first involving calculating the GIMP weighting functions in the deformed configuration using Gauss quadrature. The second approach involves determining the best GIMP approximation that can be evaluated analytically by Eq. (3.15). In two-dimensional problems this amount to defining the area of the particle characteristic function as an unrotated rectangle. Figure 3.7 illustrates the two approaches.

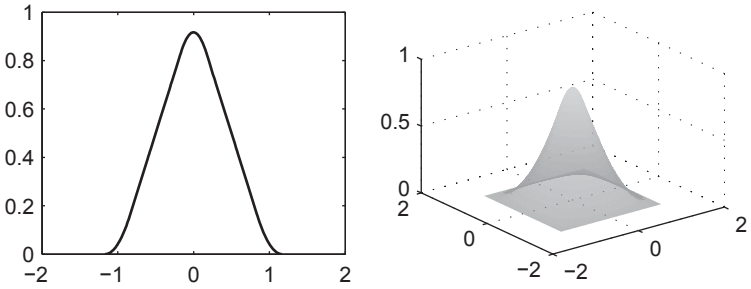


**Figure 3.6** One and two dimensional GIMP weighting functions.

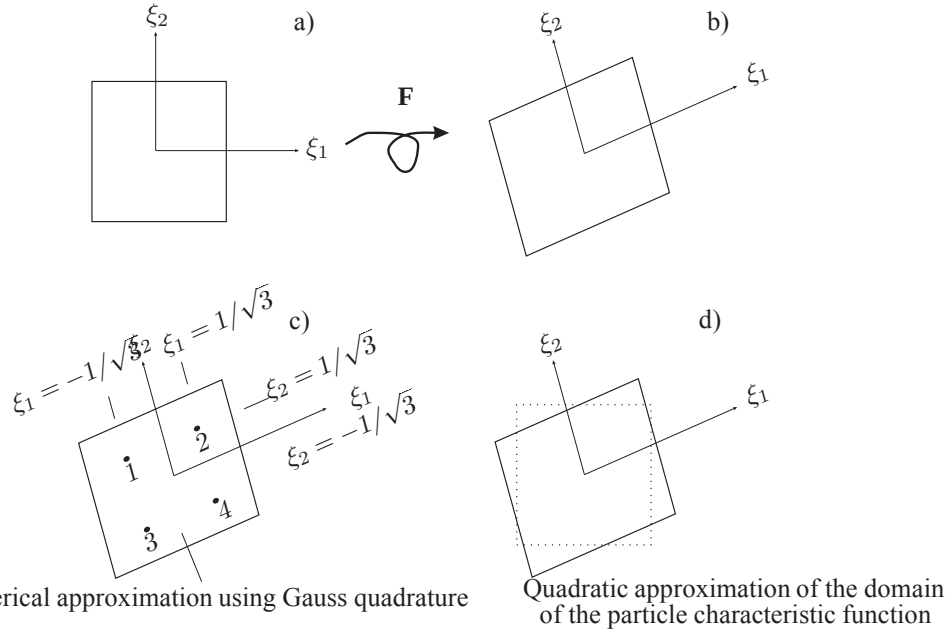


**Figure 3.7** Deformation and evaluation of GIMP weighting functions. a) Shows an initially square material point. b) shows the material point in a deformed configuration. c) One way of evaluate the weighting functions is to employ Gauss quadrature over the deformed geometry. d) Another way to evaluate the weighting functions is to represent the domain of the particle characteristic function as a quadrate. The volume of the quadrate is calculated by $V_p = \det(\mathbf{F}_p)V_p^0$. In this case, the analytically calculated weighting functions can be applied.

### 3.3.1 Evaluating the weighting functions using Gauss quadrature

A scheme for numerically evaluating the GIMP functions in the deformed configuration is presented. Each material volume is assigned a number of Gauss points. Rewriting the integral part of the weighting functions and the gradient weighting functions as sums over the Gauss points yields

$$\bar{N}_{ip} = \frac{1}{V_p} \sum_{GP=1}^{N_{GP}} \chi_p(\mathbf{x}_{GP}) N_i(\mathbf{x}_{GP}) \phi_{GP}, \tag{3.16}$$

where $GP = 1, 2, ..., N_{GP}$ is the number of Gauss points for material point $p$. The gradient weighting functions are given as

$$\frac{\partial \bar{N}_{ip}}{\partial \mathbf{x}} = \frac{1}{V_p} \sum_{GP=1}^{N_{GP}} \chi_p(\mathbf{x}_{GP}) \left. \frac{\partial \bar{N}_{ip}(\mathbf{x})}{\partial \mathbf{x}} \right|_{\mathbf{x}=\mathbf{x}_{GP}} \phi_{GP}, \tag{3.17}$$

where $\phi_{GP}$ is the weight for the Gauss point. Further, $\sum_{GP} \phi_{GP} = V_p$. The equations can be further simplified as

$$\bar{N}_{ip} = \frac{1}{4} \sum_{GP=1}^{N_{GP}} \chi_p(\mathbf{x}_{GP}) N_i(\mathbf{x}_{GP}) \bar{\phi}_{GP} \tag{3.18}$$

and

$$\frac{\partial \bar{N}_{ip}}{\partial \mathbf{x}} = \frac{1}{4} \sum_{GP=1}^{N_{GP}} \chi_p(\mathbf{x}_{GP}) \left. \frac{\partial \bar{N}_{ip}(\mathbf{x})}{\partial \mathbf{x}} \right|_{\mathbf{x}=\mathbf{x}_{GP}} \bar{\phi}_{GP}, \tag{3.19}$$

where $\sum_{GP} \bar{\phi}_{GP} = 4$, since the area measured in the local $(\xi, \eta)$-coordinate system is 4. If a single Gauss point, located at the at the position of the material point, is employed, the weighting function becomes simply the nodal shape function and the original MPM formulation given by Sulsky et al. (1995) is retrieved.

Now, numerical integration is illustrated for the two-dimensional case. Generalization to three dimensions is straightforward. An initially rectangular material area is deformed. A non-linear continuum description is employed, where the deformation is governed by the deformation gradient. Thus, the deformation of a material volume is similar to the deformation of a four node isoparametric element, as illustrated in Figure 3.8. On the left, the material area is shown in the reference configuration, while the deformed configuration of the material area is shown on the right. The local axes are denoted $\xi$ and $\eta$ with $-1 \leq \xi \leq 1$ and $-1 \leq \eta \leq 1$. By using four Gauss points located at $(\xi, \eta) = (\pm 1/\sqrt{3}, \pm 1/\sqrt{3})$, respectively, the weighting functions can be exactly integrated in case that the entire voxel is in a single cell. As the weighting functions are a product of the particle characteristic function and the nodal shape function, some grid-crossing error can be expected, as observed in the original MPM formulation, when a Gauss point changes cell. Hence, numerical integration using more Gauss points per material point can be employed to further reduce the grid crossing error. The Gauss points are updated in a similar fashion as the corners. Considering a material volume with a material point initially located at $\mathbf{x}_p^0$, the coordinate for a Gauss point in the initial configuration can be written as

$$\mathbf{x}_{GP}^0 = \mathbf{x}_p^0 + d\mathbf{x}^0, \tag{3.20}$$

where $\mathbf{x}_{GP}^0$ is the initial location of the Gauss point and $d\mathbf{x}^0$ is the line segment between the material point and the Gauss point in the initial state. At an arbitrary time the location of the Gauss point is given as

$$\mathbf{x}_{GP}^t = \mathbf{x}_p^t + d\mathbf{x}. \tag{3.21}$$

Using the deformation gradient, defined at the material point, the line segment can be calculated by

$$d\mathbf{x} = \mathbf{F} d\mathbf{x}^0. \tag{3.22}$$

The deformation gradient is determined using the procedure described in Section 3.2.

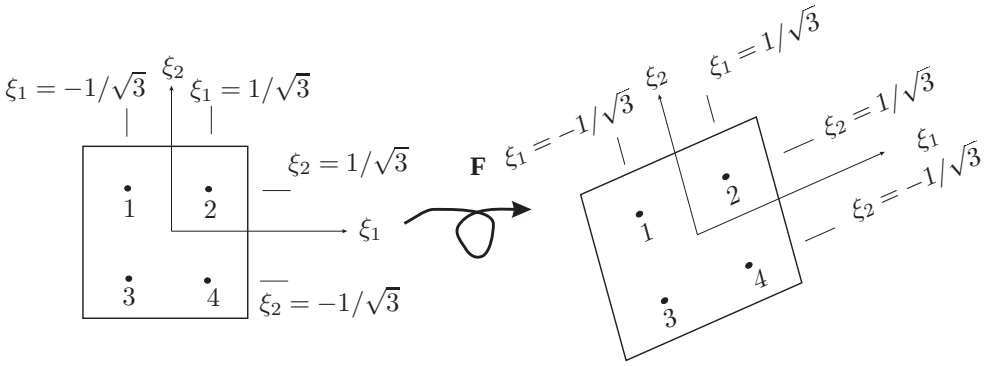


**Figure 3.8** Numerical integration for a material point using Gauss quadrature.

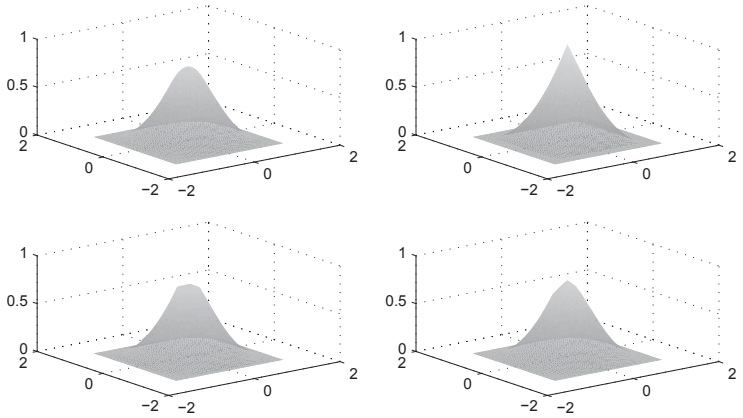


**Figure 3.9** Evaluation of GIMP weighting functions with $L = 1$ and $l_p = 1/4$. Upper left: Analytical solution. Upper right: Using 1 Gauss point. Lower left: Using a 2 by 2 Gauss points. Lower right: Using 3 by 3 Gauss points.

## Numerical evaluation of the shape functions

In order to study the numerically determined weighting functions, a material point located in the neighbourhood of a node is considered. Linear nodal shape functions and a constant particle characteristic function are employed. The value of the weighting function as function of the coordinate of material point is shown in Figure 3.9 for the analytical solution, and using 1, 4 and 9 Gauss points, respectively. The size of the material point corresponds to two by two material points per cell.

Figure 3.10 shows the corresponding gradient weighting functions As seen, using a one-point quadrature rule the linear shape functions are retrieved. Further, it is observed that the approximations using four and nine Gauss points are rather close and hence for computational efficiency the numerical examples presented next are employing weighting and gradient weighting functions obtained by using a four point quadrature rule.

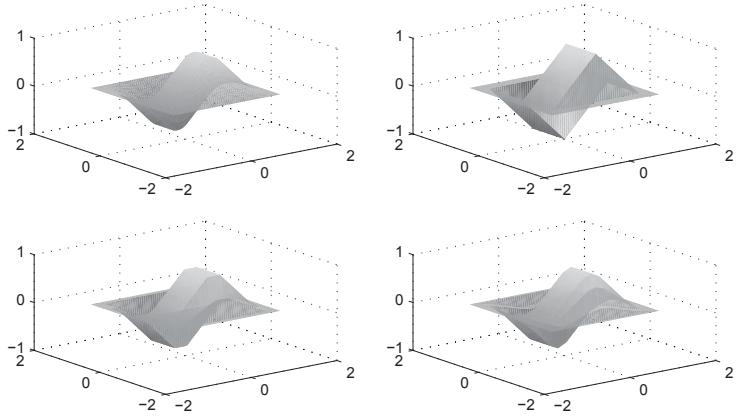

**Figure 3.10** Evaluation of GIMP gradient weighting functions with $L = 1$ and $l_p = 1/4$. Upper left: Analytical solution. Upper right: Using 1 Gauss point. Lower left: Using a 2 by 2 Gauss points. Lower right: Using 3 by 3 Gauss points.

### 3.3.2 Analytical approximation of the weighting functions

The numerical integration involved in calculating the weighting functions as a sum over the Gauss points is computationally expensive. Another approach is to perform an approximation for the domain of the particle characteristic function in such a way, that the weighting functions can be calculated analytically. As shown, if the particle characteristic function is constructed using a rectangle aligned with the direction computational grid, the weighting functions can be calculated analytically. Bardenhagen and Kober (2004) present analytical weighting functions for the one-dimensional case only depending on the length of the material point and the length of the element. The weighting functions can be calculated as bi-linear products in the two-dimensional case and tri-linear products in the three dimensional case. The calculation of the GIMP weighting functions is described above.

Here, a quadratic representation is suggested for the particle characteristic function throughout the deformation history. The length of the material point in the reference configuration in each spatial direction is denoted $l_p^0$. A consistent representation of the deformed length, $l^p$, is given by

$$l^p = l_p^0 \left(\det(\mathbf{F}_p)\right)^{\frac{1}{N_{dim}}} , \tag{3.23}$$

where $N_{dim}$ is the number of spatial directions of the model.

In Section 3.4 it is demonstrated how the tracking of the deformed geometry can be applied to split material points. If a material point is split into $n$ new material points, the lengths associated with the new material points is given by

$$l^{p,new} = \left(\frac{l^{p,old}}{n}\right)^{\frac{1}{N_{dim}}} . \tag{3.24}$$

## 3.4 Refinement in the material-point method

The aim of the presented changes to the material point method is to provide a tool for modelling extreme deformations, where traditional methods usually fail. For typical problems, the most convenient way of discretization is to divide a physical body into equally large material volumes each represented by a material point. However, commonly the nature of the problem leads to localized deformation in parts of the domain. In order to obtain better models in a computationally efficient manner, an adaptive scheme is proposed based on the idea of splitting the material points that undergo the largest strains.

### 3.4.1 Material-point splitting

The proposed splitting algorithm utilizes the concept of the GIMP formulation with a constant particle characteristic function, namely that properties and state variables are considered as constants within the voxel associated with the material point. Hence, it is possible to split this voxel into two new voxels represented by two new material points. Initially, a material point is assigned a rectangular voxel. Due to the tracking of the deformation tensor as a state variable, the deformed state of the voxel is known at any time of the modelling process. Here a simple algorithm is presented for dynamic adaptive discretization based on splitting the material points. The algorithm is described for the two-dimensional case but is easily generalized to three dimensions.

In addition to the total deformation gradient tensor, $\mathbf{F}_p$, a new deformation gradient tensor, $\mathbf{F}_p^{split}$, is defined. Typically, when the physical problem is discretized, $\mathbf{F}_p = \mathbf{I}$. The splitting deformation gradient tensor is integrated in time using Eq. (3.2). A material point is split into two new, whenever one of the following six criterions is satisfied

$$\begin{aligned} &F_{11}^{split} > \alpha, \quad F_{22}^{split} > \alpha, \\ &F_{11}^{split} < \beta, \quad F_{22}^{split} < \beta, \\ &|F_{12}^{split}| > \gamma, \quad |F_{21}^{split}| > \gamma, \end{aligned} \tag{3.25}$$

where $\alpha$, $\beta$ and $\gamma$ are heuristic constants which depends on how much deformation that is allowed before splitting is enforced. In the examples in the thesis, $\alpha = 2$, $\beta = 1/2$ and $\gamma = 1$. Figure 3.11 shows the deformed states corresponding to each of the six splitting criterions for an initially quadratic material volume with $\mathbf{F}_p^0 = \mathbf{F}_p^{split,0} = \mathbf{I}$ and illustrates the direction of splitting. Material properties what was considered as constants within the voxel of the old material volume are simply maintained in the new material points. For plane stress and plane strain problems the mass is split equally to two new material points. For axial-symmetric problems, the mass will need to be distributed to the two new material points depending on the distance from the symmetry axis.

For the new material points $\mathbf{F}_p^{new} = \mathbf{F}_p^{old}$. The splitting tensor is defined by resetting the deformation mode due to which the material points has been split. For instance, if the material points has been split due to $F_{11}^{split,old} > 2$, then $F_{11}^{split,new} = 1$ and the other components of the split tensor are inherited from the parent material point to the two new points.

Figure 3.12 shows the position of the new material points and Gauss points when numerical evaluation of weighting functions is utilized. The location of the new material points (and Gauss points if numerical integration are performed) are found based on the reference geometry and the

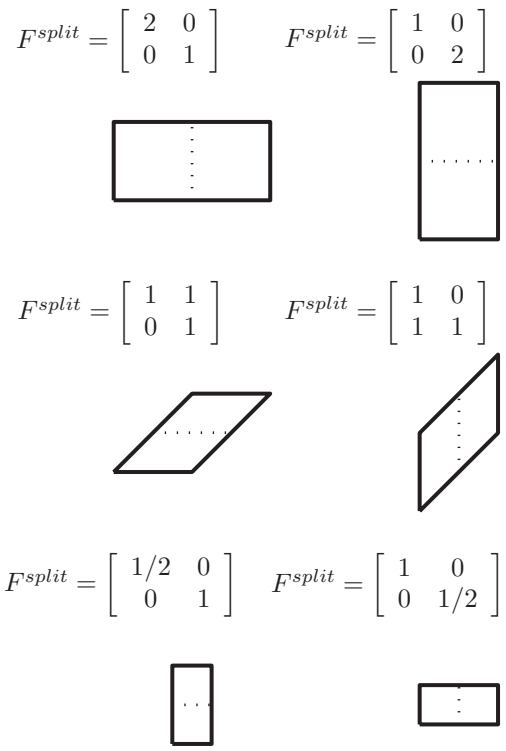


**Figure 3.11** Deformation modes corresponding to the suggested splitting criterion of $\alpha = 2$, $\beta = 1/2$ and $\gamma = 1$. The splitting is indicated by the dotted lines.

**Figure 3.12** Numerically integrated weighting functions. Old and new configuration of material volumes and Gauss-points, for splitting due to extreme deformation.

**Figure 3.13** Splitting scheme for material points in case of extreme deformation. Representation of deformed geometry and position of material points before and after splitting due to extreme deformation.

total deformation gradient tensor. The criterion for splitting material volumes presented here, is based on deformations, as the aim is to provide a better representation of deformation patterns involving extreme local deformations. On the other hand an adaptive discretization scheme based on strain rates can easily be implemented in order to provide finer discretization, for instance in the case of beginning plastic yielding.

### 3.4.2 Material-point splitting in case of extreme deformations

In the case of extreme shear deformations, the splitting scheme shown in Figure 3.12 will eventually fail. Here, material points, described a total deformation gradient tensor will obtain a needle-like shape. An example of this is shown in Section 5.2. In such cases, an approach for splitting somewhat similar to the ideas described in Subsection 3.3.2 is introduced, thus defining two material points with voxels that are quadrates. The location of the new material points (and Gauss points) are found based on the reference geometry and the total deformation gradient tensor. Figure 3.13 shows how to define the new particle characteristic domains where the quadratic representation is employed. The size of the new material points is defined as the size utilized in the GIMP approximation defined by Eq. (3.24). For the new material points, $\mathbf{F}_p = \mathbf{F}_p^{split} = \mathbf{I}$. In preparing the numerical examples for the thesis, several algorithms for enforcing the proposed "reference" splitting has been tested. The optimal way depends of the specific problem and only some general ideas has been obtained. The problem with material points obtaining needle-like shapes are mainly due to extreme shear deformations. Another observation that the most extreme deformations has occurred for material points which has been split the most times. Hence, as a simple way of augmenting the splitting criterion of Section 3.4 in the numerical examples presented, this type of slitting is enforced whenever a material point points has been split four times.

In the numerical examples, the presented splitting algorithm is employed to obtain a better representation of localized deformation.

### 3.4.3 Refining the computational grid

It should be noted that the suggested splitting schemes are generally applicable to analysis of large strain problems. However, in the presented examples the grid is quadrilateral with associated bi-linear shape functions. Even though material points have been split, the same quadrilat-

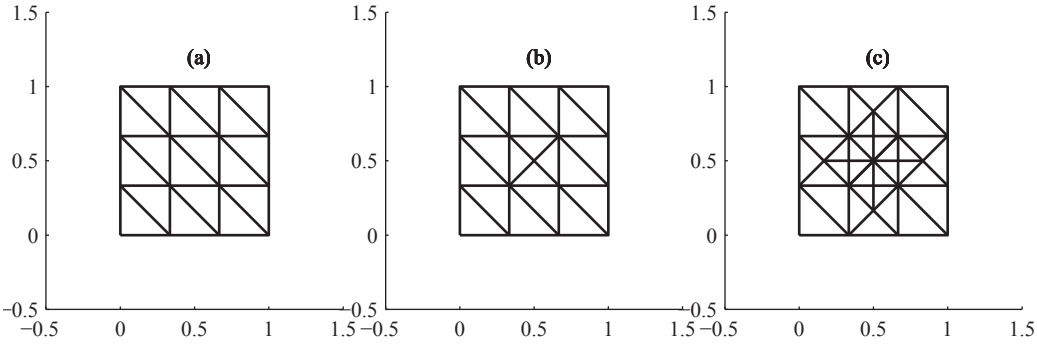


**Figure 3.14** Using triangular elements for the grid would allow for the possibility of a dynamical adaptive mesh. (a) Shows an initially regular grid. The central cell is represented as two triangular elements. Consisting of nine rectangular cells each represented by two triangles. (b) The central cell is now represented using four regular triangular elements. (c) further splitting of the central cell into eight regular triangles. In order to satisfy the requirement of displacement continuity, the neighbouring cells are split into five triangles.

eral grid has been maintained throughout the simulations. In order to get full advantage of the proposed splitting of material points, an adaptive algorithm for refining the grid simultaneously with the splitting of material points would need to be explored. As known from finite element analysis, in order for the shape functions to provide consistent interpolation, the displacement field needs to be continuous along element boundaries. This would make it tricky to perform adaptive remeshing using bi-linear shape functions. One idea is to apply triangular elements instead of the traditionally employed bi-linear quadrilateral elements. The concept of refining the grid using triangular nodal shape functions is illustrated in Figure 3.14 but has not been further addressed in the present work.

# CHAPTER 4
# Stresses in the material-point method

This chapter analyses the representation of stresses in the material-point method. Firstly, a formulation to ensure that the material-point stress represent the current Cauchy stress tensor is presented. Secondly, the problems associated with the MPM formulation, where stresses are updated individually for the material points, are discussed. Next, one of the causes of degradation of the stress field is discussed. Finally, it is shown that realistic stress fields can be obtained by interpolating the results via the computational grid.

## 4.1 Objective evaluation of stresses

Usually, when large deformations are analysed, an objective stress rate should be employed that eliminates the stress change due to a pure rotation. For this purpose, the stress rates proposed by Green and Naghdi or Jaumann are often utilized. A presentation and discussion of the different objective stress rates is given by Johnson and Bamman (1984). In the work by Więckowski et al. (1999), the Jaumann stress rate is employed for modelling silo discharging using the material-point method. Alternatively, as employed here, the increment of the deformation gradient tensor is utilized in such a way that the considered stress at all the discrete time steps is the Cauchy stress. Introducing the linear strain rate as

$$\dot{\boldsymbol{\varepsilon}} = \frac{1}{2}\left(\frac{\partial \mathbf{v}}{\partial \mathbf{x}} + \left(\frac{\partial \mathbf{v}}{\partial \mathbf{x}}\right)^{T}\right), \tag{4.1}$$

the stress is integrated using an updated Lagrangian scheme. At the beginning of the time step, a reference state is defined by $\mathbf{S}^k := \boldsymbol{\sigma}^k$, where $\mathbf{S}$ is the second Piola Kirchhoff stress tensor. For small strain increments, the approximation $\dot{\boldsymbol{\varepsilon}} = \dot{\mathbf{E}}$, where $\dot{\mathbf{E}}$ the rate of change of the Green strain tensor, is valid. Thus, the rate of change of the second Piola Kirchhoff stress tensor is given by

$$\dot{\mathbf{S}} = \mathbf{C}\dot{\boldsymbol{\varepsilon}}, \tag{4.2}$$

where $\mathbf{C}$ yields the constitutive behaviour of an observed material point at the current material state.

Using a forward difference scheme, the Piola-Kirchhoff stress at the end of the time step is approximated by

$$\mathbf{S}^{k+1} = \boldsymbol{\sigma}^k + \Delta t \dot{\mathbf{S}} \tag{4.3}$$

The local deformation occurring during the time step is given by $\Delta F^k_{\alpha\beta}$, hence the Cauchy-stress at end of the time-step is given by

$$\boldsymbol{\sigma}^{k+1} = \frac{1}{\Delta J}\Delta\mathbf{F}^{k+1}\mathbf{S}^{k+1}\left(\Delta\mathbf{F}^{k+1}\right)^T, \tag{4.4}$$

where $\Delta J = \det(\Delta\mathbf{F}^{k+1})$. The idea of utilizing a non-linear strain measure within the MPM is introduced by Guilkey and Weiss (2003), who introduce a weak form of the balance of momentum based on the deformation gradient and the second Piola-Kirchhoff stress tensor.

## 4.2 Grid-crossing errors in the MPM

In order to accurately model landslides and other geotechnical problems, the stresses are important. Especially, as yield criteria such as the Mohr-Coulomb criterion are based on the stresses. However, the representation of stresses is probably the most problematic issue of the material point method.

As mentioned in Section 2.1, one problematic issue of the material point method is the grid-crossing error. In original formulation of the material-point method, linear shape functions are used to map between the nodes and the material points. Linear shape functions have spatial derivatives that are discontinuous across element boundaries. This has the effect that unphysical stress variations occur when material points move between the cells in a fixed grid. This is illustrated in the following example, see Figure 4.1. Imagine that the three grid nodes shown in Figure 4.1 are part of a larger model. A homogenous stress state is presumed in the considered part of the model. The only material points interacting with grid node no. 2 are the four nodes shown in the figure. The grid nodes are located at $x_1$, $x_2$ and $x_3$, respectively. The distance between the grid nodes is denoted $\Delta x$. The local coordinates are given by

$$\xi_1 = \frac{x - x_1}{\Delta x} \quad \xi_2 = \frac{x - x_2}{\Delta x}, \quad \Delta x = x_2 - x_1 = x_3 - x_2 \tag{4.5}$$

and the shape functions are given by

$$\begin{aligned} N_1(x) &= 1 - \xi_1, && x_1 < x < x_2, \\ N_2(x) &= \xi_1, && x_1 < x < x_2, \\ N_2(x) &= 1 - \xi_2, && x_2 < x < x_3, \\ N_3(x) &= \xi_2, && x_2 < x < x_3. \end{aligned} \tag{4.6}$$

The stresses at the four material points are identical, $\sigma_1 = \sigma_2 = \sigma_3 = \sigma_4 = \sigma$, before grid crossing occurs. Finally, a volume of $V_p$ is associated with each material point.

The material points move relatively to the grid with a constant velocity $v_1 = v_2 = v_3 = v_4 = v$. The gradients of the shape functions are given by

$$\begin{aligned} \tfrac{dN_1}{dx}(x) &= -\tfrac{1}{\Delta x}, && x_1 < x < x_2, \\ \tfrac{dN_2}{dx}(x) &= \tfrac{1}{\Delta x}, && x_1 < x < x_2, \\ \tfrac{dN_2}{dx}(x) &= -\tfrac{1}{\Delta x}, && x_2 < x < x_3, \\ \tfrac{dN_3}{dx}(x) &= \tfrac{1}{\Delta x}, && x_2 < x < x_3. \end{aligned} \tag{4.7}$$

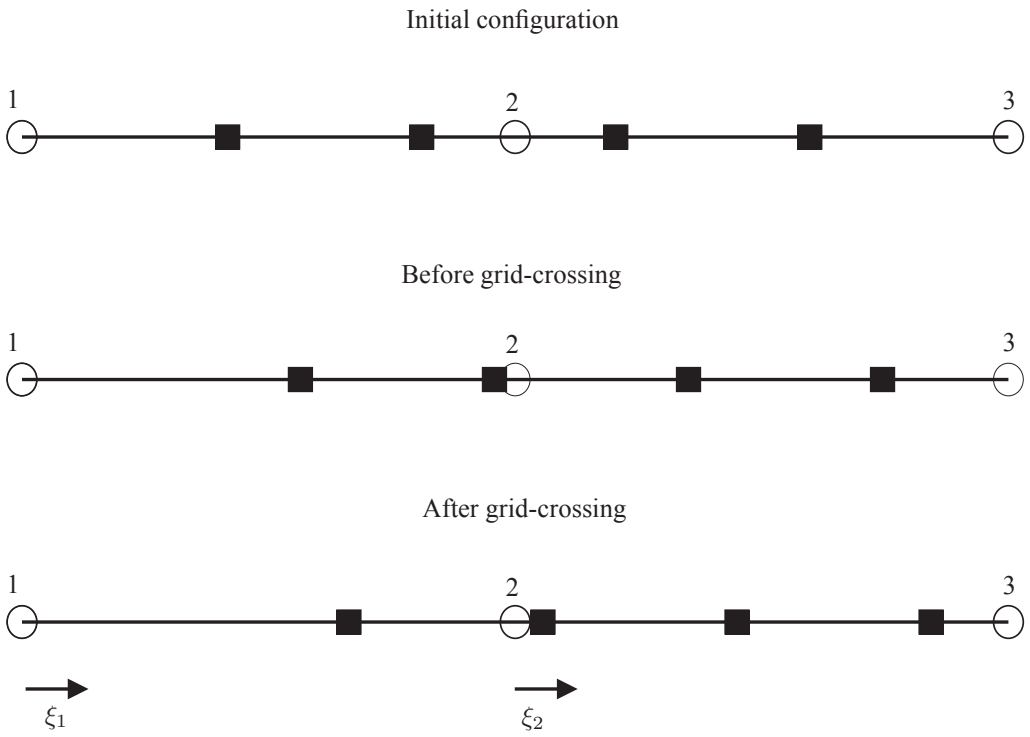


**Figure 4.1** Example illustrating the grid-crossing error.

The internal forces are calculated by

$$f_i^{int} = \sum_{p=1}^{N_p} \sigma_p \left. \frac{dN_i}{dx} \right|_{x=x_p} V_p. \tag{4.8}$$

Before the crossing, the internal force at node 2 is given by

$$f_2^{int,before} = \sigma V_p \left( 2(\frac{1}{\Delta x}) + 2(-\frac{1}{\Delta x}) \right) = 0. \tag{4.9}$$

After the crossing, the internal force at the node becomes

$$f_2^{int,after} = \sigma V_p \left( \frac{1}{\Delta x} + 3(-\frac{1}{\Delta x}) \right) = -2\frac{\sigma V_p}{\Delta x}. \tag{4.10}$$

Similarly, the change of internal force due the crossing at nodes 1 and 3 are

$$\Delta f_1^{int} = \Delta f_3^{int} = \frac{\sigma V}{\Delta x}. \tag{4.11}$$

At the end of the time step, the internal forces are used to update the material points by

$$v_p^{k+1} = v_p^k + \Delta t \sum_{i=1}^{N_n} \frac{N_{ip}^k (f_i^{int,k})}{m_i^k}. \tag{4.12}$$

Hence, when crossing occurs, the material points near node 2 experience a negative acceleration while material points near nodes 1 and 3 experience a positive acceleration. At the next time steps, these erroneous accelerations lead to unphysical strain increments, leading to unphysical stresses. In the MPM formulation using linear interpolation, the grid-crossing errors often prevent convergence when a problem is refined in terms of the number of grid nodes an maintaining a constant number of material points per. cell (Steffen, Wallstedt, Guilkey, Kirby, and Berzins 2008). Further, the noisy results due to grid crossing for MPM using linear shape functions is the main motivation for introducing the GIMP formulation. In the GIMP formulation, when using a spatially fixed grid, a material points that moves relatively to the grid the change of sign of the internal forces will gradually occur, typically over many time steps. As shown several references, the GIMP formulation to a certain extent reduces the negative effects associated with the grid-crossing, however the grid-crossing errors are not eliminated. In the next section, the performance of the linear MPM formulation and the GIMP formulation are compared with respect to the effects of grid crossing.

## 4.3 Gravitational loading in the MPM

In order to model the collapse of slopes, the stress distribution in the slope prior to the collapse needs to be known. This is obtained by the assumption of an elastic stress distribution. Here an approach described in Paper II is employed to determine the elastic stress distribution due to the weight of the soil. The initial stress state is determined using an incremental gravitational scheme. It involves using the dynamical MPM scheme to gradually apply the gravity to the slope as an external force according to Eq.(2.16). Using a total time period of $T$ to apply the gravity the current gravity, the gravity is increased using a sine function until $T/2$ and then maintained constant until $T$ in order to determine a state of equilibrium. In order to ensure a more robust scheme, a slight moderation compared to Paper II is employed, where the gravity is increased according to

$$\mathbf{g}_{current}(t) = \left\{ \begin{array}{cc} 0.5\mathbf{g}(\sin(\frac{2\,t\,\pi}{T} - \frac{\pi}{2}) + 1) & \text{if } t \leq T/2 \\ \mathbf{g} & \text{if } t > T/2 \end{array} \right\}, \tag{4.13}$$

where $\mathbf{g}_{current}(t)$ is the current gravity vector at time $t$ of the incremental gravitation and $\mathbf{g}$ is the total acceleration vector. Using the incremental gravitation scheme it is possible to determine the stress distributions in slopes of general geometry.

Here, the determination of stresses using the incremental gravitation scheme is utilized to determine the stresses for the very simple problem of a horizontal soil surface. Figure 4.2 shows the setting of material-points and grid nodes for a soil box with a horizontal soil surface. Figure 4.3 shows how the gravity is gradually increased using a total time of 20 seconds. The model corresponds to a horizontal soil surface at rest. In this case, the vertical normal stress increases linearly according to

$$\sigma_{yy}(d) = g\rho d, \tag{4.14}$$

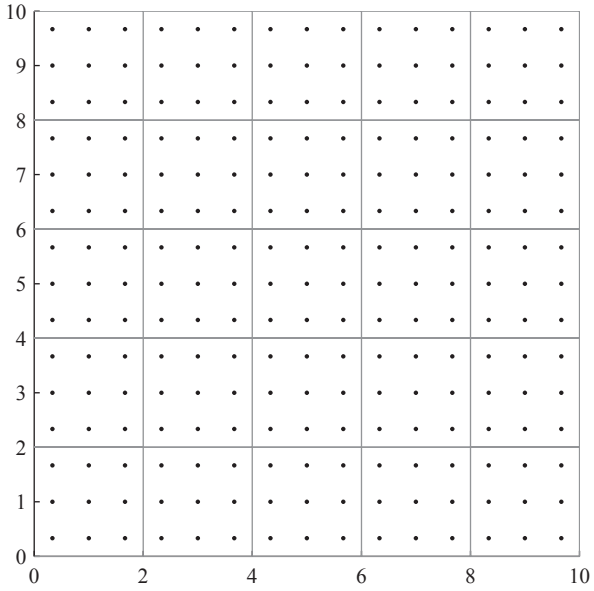


**Figure 4.2** Quasi-static determination of stresses in a horizontal soil column. The soil is fixed horizontally along the vertical walls and vertically fixed along the bottom. Initial setting of material points and grid nodes. The units of the axis are metres.

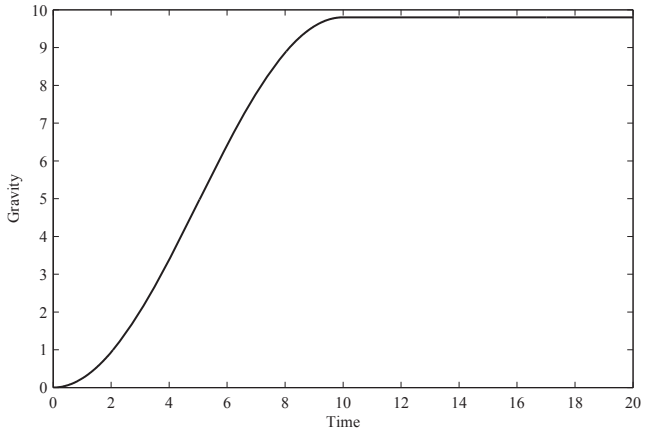


**Figure 4.3** The initial stress state is determined using incremental gravitation, where the stress is gradually applied over time. The figure shows an example where the gravity is increased over 10 seconds and maintained constant in order to ensure a state of equilibrium.

where $g$ is the gravity, $\rho$ is the density and $d$ is the vertical distance to the soil surface.

The grid is maintained spatially fixed in time. In the present example, a Poisson ratio of zero is employed in order to restrict the grid-crossing to the vertical direction. If Young's modulus is sufficiently high and the density is sufficiently low, no grid crossings occur for the MPM

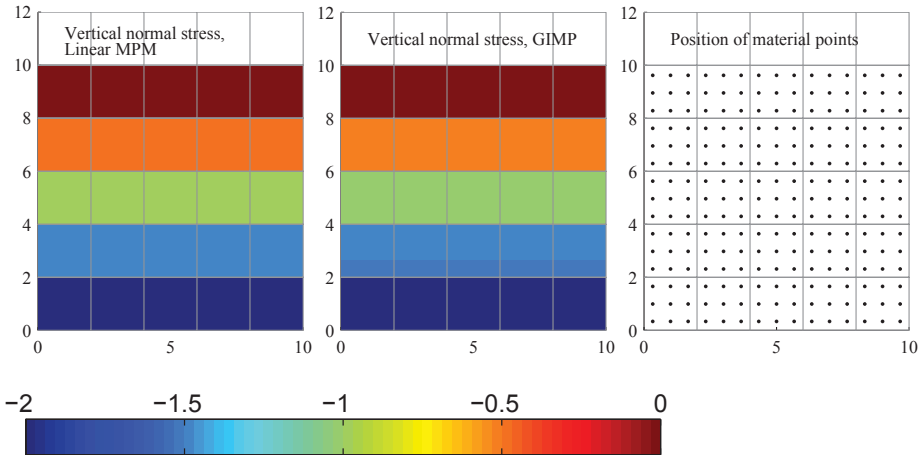


**Figure 4.4** Vertical normals stresses and position of material points at the end of the quasi-static simulation for a hard soil ($E = 20$MPa, $\rho^0 = 2 \cdot 10^3 \text{kg/m}^3$, i.e. where no grid crossings occur for the Linear MPM model.

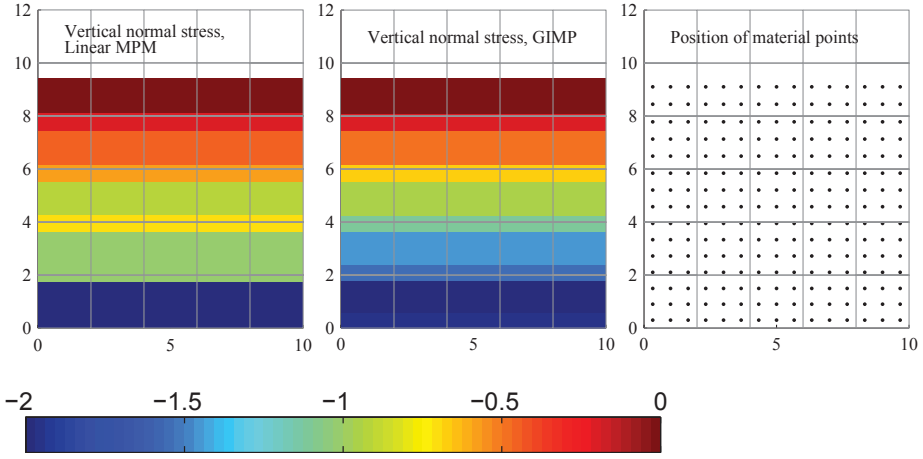


**Figure 4.5** Vertical normals stresses and position of material points at the end of the quasi-static simulation for a soft soil ($E = 5$MPa, $\rho^0 = 6 \cdot 10^3 \text{kg/m}^3$, i.e. where several grid crossings occur.

formulation. In the GIMP formulation, grid crossing will occur gradually as the material-point voxels gradually move between the cells. In the case with $E = 20$ MPa and $\rho^0 = 2 \cdot 10^3$ kg/m$^3$, no grid crossing occurs in the MPM formulation. Figure 4.4 shows the vertical normal stresses at the material points at the end of the simulation. Figure 4.5 shows the vertical stresses in the case of a softer soil, where grid crossings occur at the end of the quasi-static simulation for bi-linear MPM and GIMP, respectively. Figures 4.4 and 4.5 show that where grid crossing completely degrades the linear MPM solution, the GIMP model maintains physically realistic field quantities. Further, Paper II shows that stresses obtained by the incremental gravitation schemes corresponds to stresses determined by commercial finite element software. Finally,

Chapter 5 discusses in more detail the initial state determined by the incremental gravitation scheme.

## 4.4 Alternative approaches for updating stresses

As mentioned in Chapter 2, the question of when to update stresses has been a subject of research (Bardenhagen 2002). Specifically, Bardenhagen discusses two different ways to update the stresses, either before or after the calculation of internal forces. The two approaches are denoted *update stress first* (USF) and *update stress last* (USL). Bardenhagen concluded that the USF approach yields a reasonable energy conservation while significant numerical energy dissipation is associated with the USL scheme. Now, a slight change is proposed for the USL stress update scheme in order to define a consistent average update scheme. The two schemes as well as a suggested combination of the two schemes is presented below:

### Updating stresses first

The USF scheme for updating the stresses between time-step $k$ and $k+1$ can be described by:

1. Nodal velocities at the start of the time step, $\mathbf{v}_i^k$, are calculated by Eq. (2.23),
2. strain increments at the material points, $\Delta\boldsymbol{\varepsilon}_p^k$, are calculated using $\mathbf{v}_i^k$ and Eq. (2.20),
3. stresses, $\boldsymbol{\sigma}_p^{k+1}$, are updated individually for each material point using $\Delta\boldsymbol{\varepsilon}_p^k$,
4. the internal forces are calculated using $\boldsymbol{\sigma}_p^{k+1}$ and Eq. (2.51),
5. the position and velocity of the material points are calculated using the calculated internal forces.

### Updating stresses last

Similarly, the update stress last scheme, utilized in this thesis is given by

1. Nodal velocities at the start of the time step, $\mathbf{v}_i^k$, are calculated by Eq. (2.23)
2. the internal forces are calculated using $\boldsymbol{\sigma}_p^k$ and Eq. (2.51),
3. the velocities of the material points are calculated using the calculated internal forces,
4. new nodal velocities are calculated using the updated material-point velocities,
5. strain increments at the material points, $\Delta\boldsymbol{\varepsilon}_p^k$, are calculated using $\mathbf{v}_i^{k+1}$ and Eq. (2.20).
6. stresses, $\boldsymbol{\sigma}_p^{k+1}$, are updated individually for each material point using $\Delta\boldsymbol{\varepsilon}_p^k$,

### Combining the two formulations

Finally, a combination of the two formulations is considered. In order to obtain clarity, the full update scheme is summarised below:

1. Nodal velocities at the start of the time step, $\mathbf{v}_i^k$, are calculated by Eq. (2.23),
2. strain increments at the material points, $\Delta\boldsymbol{\varepsilon}_p^{k\to k+1/2}$, are calculated using $\mathbf{v}_i^k$ and Eq. (2.20) using a time-increment of $\Delta t/2$,
3. stresses, $\boldsymbol{\sigma}_p^{k+1/2}$, are updated individually for each material points using $\Delta\boldsymbol{\varepsilon}_p^{k\to k+1/2}$,
4. the internal forces are calculated using $\boldsymbol{\sigma}_p^{k+1/2}$ and Eq. (2.51),
5. the position and velocity of the material points are calculated using the calculated internal forces,
6. new nodal velocities are calculated using the updated material-point velocities,
7. strain increments at the material points, $\Delta\boldsymbol{\varepsilon}_p^{k+1/2\to k+1}$, are calculated using $\mathbf{v}_i^{k+1}$ and Eq. (2.20) using a time-increment of $\Delta t/2$
8. stresses, $\boldsymbol{\sigma}_p^{k+1}$, are updated individually for each material point using $\Delta\boldsymbol{\varepsilon}_p^{k+1/2\to k+1}$,

The idea of calculating the strain increments in the middle of the time-step is similar to a formulation presented by Love and Sulsky (Love and Sulsky 2006b).

Now, the colliding disc problem of Chapter 2 is revisited. In order to compare the three suggested stress update schemes, the kinetic energy and the potential energy of the system are considered. The kinetic energy at any time step is simply found as a sum over the material points by

$$E^{kin} = \frac{1}{2}\sum_{p=1}^{N_p} m_p ||\mathbf{v}_p||^2 \tag{4.15}$$

The potential energy in this example is solely the strain energy. It is integrated over the time-steps by

$$E^{pot,k+1} = E^{pot,k} + \sum_{p=1}^{N_p} \frac{m_p}{\rho_p} \frac{\boldsymbol{\sigma}_p^{k+1} + \boldsymbol{\sigma}_p^k}{2} : \Delta\boldsymbol{\varepsilon}_p^k \tag{4.16}$$

Finally, the mechanical energy the simply the kinetic and the total energy

$$E^{mec,k+1} = E^{pot,k+1} + E^{kin,k+1}. \tag{4.17}$$

Figure 4.6 shows the kinetic, potential and mechanical energy as a function of time for the disc impact problem utilizing the three different stress-update schemes. As seen, utilizing the average stress-update scheme, the mechanical energy is conserved during the entire collision.

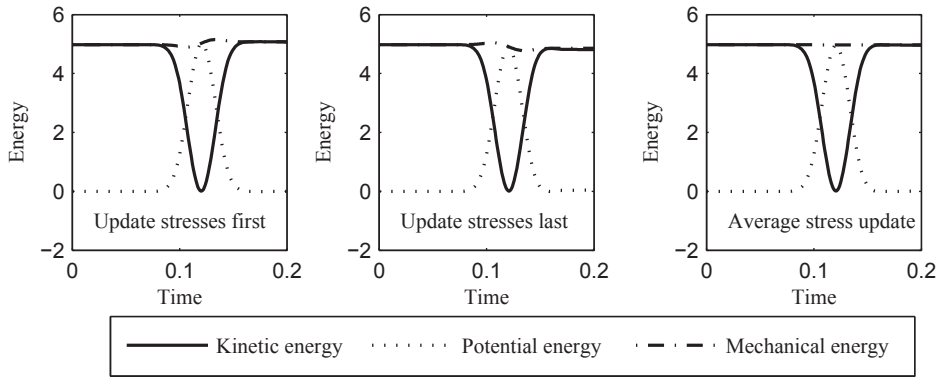


**Figure 4.6** Energies in the colliding disc problem as a function of time using the different stress-update schemes. During the collision, the kinetic energy is transformed into potential energy when the discs compresses. Eventually, the potential energy is transformed back to kinetic energy when the two discs depart. Note that the new average stress-update scheme conserve the energy during and after collision.

## 4.5 Reduced integration of stress

Another effect, which is present in the GIMP and MPM formulations employing linear nodal shape functions for the grid is the so so-called *parasitic shear stresses* the concept of parasitic shear within a finite element context is discussed by Cook et al. (2002). Parasitic shear occurs because the bi-linear quadrilaterals contains all linear polynomial terms but only a single quadratic term. The effect of parasitic shear stress in the case of the classical cantilevered Timoshenko beam, (1970), is described in Paper I.

In finite element analysis, the approach typically applied when dealing with parasitic shear stress is to apply reduced integration of the shear stresses (Sandhu and Singh 1978). This approach is utilized by Andersen et al. (2009) to study the cantilevered Timoshenko beam. Here, the selected shear integration is applied by replacing $\nabla N_{ip}$ by $\nabla N_{ic} = \nabla N_i(\mathbf{x})|_{\mathbf{x}=\mathbf{x}_c}$, where $\mathbf{x}_c$ denotes the center of the element in which material point $p$ is located.

Figure 4.7 shows different stress components using the MPM formulation and standard MPM formulation and selective integration respectively. As seen, the application of reduced integration effectively reduces the parasitic shear. Unfortunately, for other problems the application of reduced integration yields other numerical anomalies. The example of the elastic colliding discs is considered. Figure 4.8 shows the horizontal normal stress at the time $t = 0.13$ using full integration and reduced integration, respectively.

## 4.6 A new approach for visualizing stresses

Paper I, which presents an analysis of a cantilevered beam, shows that for the cantilevered beam the shear stresses at the material points are not realistic for MPM using linear interpolation. Specifically, unrealistic shear stress variations occur within the linear quadrilaterals. But if the stresses are interpolated to the grid nodes and visualized, a realistic stress distribution is seen. This suggests a different way of visualising the stresses using interpolation via the grid nodes. In

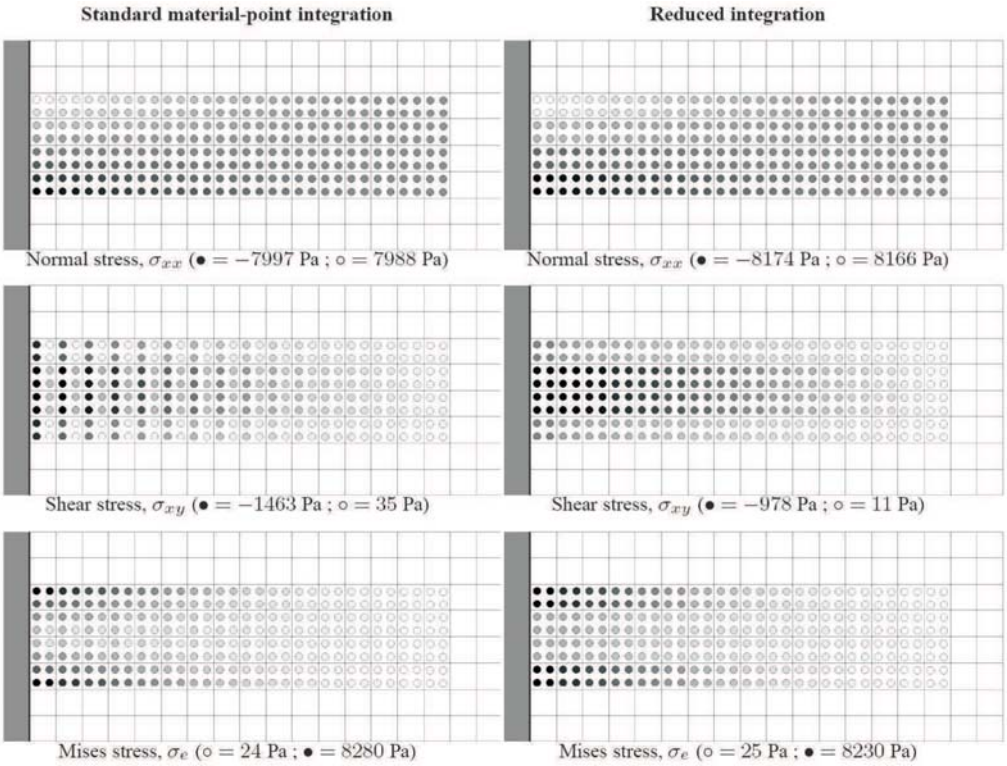


**Figure 4.7** Stresses in the elastic beam at the end of the simulation. A beam with a length of $L = 8$ m in the $x$-direction and a height of $H = 2$ m in the $y$-direction is analysed. The stresses are determined using an incremental gravitation scheme using a gravity of 10 m/s$^2$ and a density of $\rho = 10$ kg/m$^3$. A Young's modulus of $E = 10$ MPa and a Poisson ratio of $\nu = 0.3$ is employed. The figure is also presented in (Andersen et al.,2009).

accordance with Paper I, grid node stress tensors are defined by

$$\boldsymbol{\sigma}_i = \sum_{p=1}^{N_p} \frac{\boldsymbol{\sigma}_p \Phi_{ip} m_p}{m_i}, \tag{4.18}$$

where $\boldsymbol{\sigma}_i$ is the stress tensor, associated with grid node $i$, $\boldsymbol{\sigma}_p$ is the stress of material point $p$, $\Phi_{ip}$ is the interpolation function while $m_i$ and $m_p$ are the nodal and material point masses, respectively. Using the nodal stresses, a smoothed material point stress tensor is defined as

$$\boldsymbol{\sigma}_p^{smooth} = \sum_{i=1}^{N_n} \boldsymbol{\sigma}_i \Phi_{ip}. \tag{4.19}$$

Figure 4.9 shows the same horizontal normal stresses as visualized in Figure 4.8 but smoothed using Eq. (4.19). As seen, if the stresses are interpolated via the grid nodes, both types of integration yield realistic stress fields.

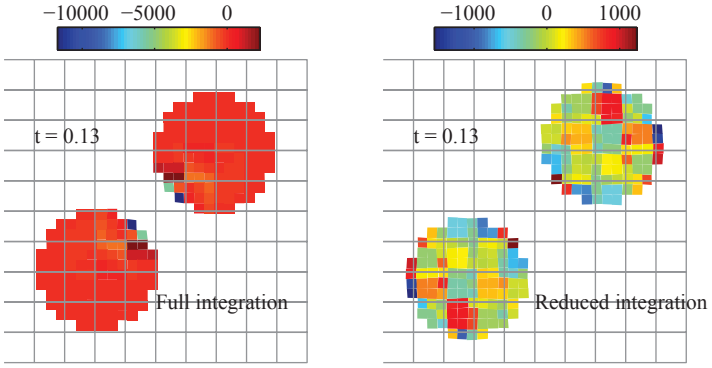


**Figure 4.8** Horizontal normal stresses for the individual material points in the colliding disc problem at $t = 0.13$ using full and reduced integration, respectively. As seen the full integration produces a stress field, whereas the reduced integration degenerates the normal stress field.

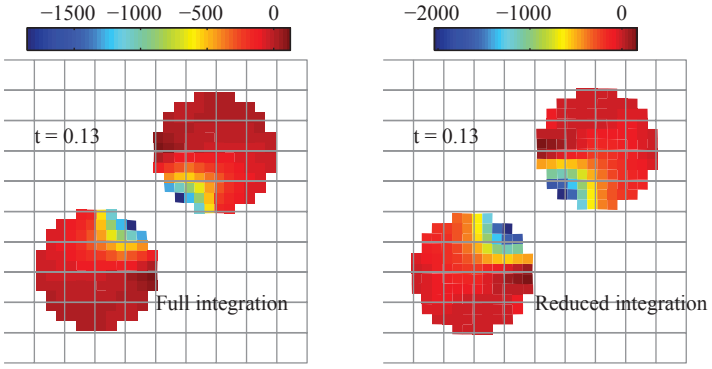


**Figure 4.9** Smoothed horizontal normal stresses using Eq. (4.19) in the colliding disc problem at $t = 0.13$ using full and reduced integration, respectively. As seen both simulations simulations provides realistic stress fields when the smoothed stresses is utilized for visualization.

# CHAPTER 5
# Numerical examples

Two numerical examples employing the concepts presented in Chapters 3 and 4 are presented. Both examples explore the dynamic collapse of soil modelled by an elasto-plastic framework. The first example involves the collapse of a soil column placed on a frictional surface. The second example explores the dynamics when an unstable slope collapses.

## 5.1 Collapsing soil column

In order to study the effects of the proposed large-strain formulation as well as to study stress distributions obtained by the MPM, the collapse of a soil column is analysed. A rectangular block of soil is placed on a frictional surface. A quadratic nodal grid with three times three material points per cell is employed. Figure 5.1 shows the discretization used for the problem.

The most applied material model for elasto-plastic analysis of soil is the Mohr-Coulomb model. In the Mohr-Coulomb model a yield function, $f$, is defined. The yield function determines the response based on a yield criterion, where $f < 0$ implies elastic response, while $f = 0$ leads to elasto-plastic response. The Mohr-Coulomb yield function is defined in terms of principle stresses by

$$f = \frac{1}{2}(\sigma_3 - \sigma_1) + \frac{1}{2}(\sigma_1 + \sigma_3)\sin(\phi) - c\cos(\phi), \tag{5.1}$$

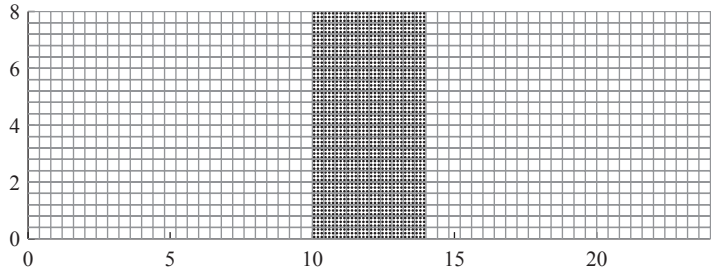


**Figure 5.1** Discretization of the collapsing soil column. The figure shows the coordinates of the material points.

where $\phi$ is the angle of friction and $c$ is the cohesion. The principal stresses are considered positive in tension and $\sigma_1 \leq \sigma_2 \leq \sigma_3$. The second principal stress is assumed not to influence the strength provided by the Mohr-Coulomb criterion.

The stress rate is given in terms of the elastic strain increment, i.e.

$$\dot{\boldsymbol{\sigma}} = \mathbf{C} : (\dot{\boldsymbol{\varepsilon}} - \dot{\boldsymbol{\varepsilon}}^p), \tag{5.2}$$

where $\dot{\boldsymbol{\varepsilon}}$ is the total strain rate, $\dot{\boldsymbol{\varepsilon}}^p$ is the plastic rate and $\mathbf{C}$ is the elastic constitutive tensor. The plastic strain increment is found using the relation

$$\dot{\boldsymbol{\varepsilon}}^p = \dot{\lambda} \frac{\partial g}{\partial \boldsymbol{\sigma}}, \tag{5.3}$$

where $\dot{\lambda}$ a positive scaling factor and $g$ is the plastic potential function given by

$$g = \frac{1}{2}(\sigma_3 - \sigma_1) + \frac{1}{2}(\sigma_1 + \sigma_3)\sin(\psi). \tag{5.4}$$

Here $\psi$ is the angle of dilatation of the soil. In the numerical solution, finite stress increments are considered. The stress increment is calculated by firstly calculating an elastic predictor stress. This elastic predictor stress may be outside the yield surface. An efficient return of the stresses back to the yield surface is obtained by the algorithm proposed by Clausen et al. (2006).

The soil is described using the following set of material properties:

$$E = 20\text{MPa}, \quad \nu = 0.42, \quad \rho_0 = 10^3\text{kg/m}^3, \quad c = 1\text{kPa}, \quad \phi = 42^\circ \quad \text{and} \quad \psi = 0^\circ. \tag{5.5}$$

A frictional coefficient $\mu = 0.6$ is prescribed at the lower boundary.

An initial $K_0$-stress state is specified with the vertical normal stress given by

$$\sigma^0_{yy} = -dg\rho^0, \tag{5.6}$$

where $g = 9.8\text{m/s}^2$ is the gravity and $d$ is the distance from the top soil surface. The initial horizontal normal stresses are given by

$$\sigma^0_{xx} = \sigma^0_{zz} = -dg\rho^0 K_0, \tag{5.7}$$

where the earth pressure coefficient is given by $K_0 = \nu/(1-\nu)$. Finally, $\sigma^0_{xy} = 0$ is prescribed for all material points. At the bottom of the modelled domain, a frictional boundary condition is specified, given in terms of a coefficient of friction $\mu$. Obviously, as the soil is not supported in the horizontal direction, the stresses cannot be sustained and a plastic collapse will occur.

A simple way of implementing a frictional boundary condition is suggested. The resulting force, as calculated from the right-hand side of Eq. (2.49), is decomposed into a normal component, $f_n$, and a tangential component, $f_t$. The normal force is considered positive if it is directed outward from the boundary. Friction is only present in the case of compressive normal force, i.e. when $f_n > 0$, and separation is allowed otherwise. In addition to the internal and external forces, a frictional force is introduced, given by

$$f_t \leq \mu f_n, \tag{5.8}$$

where $\mu$ is the coefficient of friction. Two estimates of the velocity at the end of the time step are calculated: The velocity without any friction and the velocity with full friction. The velocity without any friction is solved from Eq. (2.49) as

$$\tilde{v}_t^{i,k+1} = v_t^{i,k} + \frac{\Delta t}{m_i}(f_t^{i,int} + f_t^{i,ext}) \tag{5.9}$$

and the estimated velocity in the case of full friction is given by

$$\hat{v}_t^{i,k+1} = v_t^{i,k} + \frac{\Delta t}{m_i}(f_t^{i,int} + f_t^{i,ext} + f_t^{i,fric}), \tag{5.10}$$

where the frictional force is given by $f_t^{i,fric} = -\text{sign}(v_t^{i,k})\mu f_n$. In the case of $\tilde{v}_t^{i,k+1}\hat{v}_t^{i,k+1} > 0$, full friction is present and the resulting force is given by the force term of Eq. (5.10). Otherwise, the friction stops the material and the resulting force present in the node is given by

$$f_t^{i,res} = -\frac{m_i v_t^{i,k}}{\Delta t}. \tag{5.11}$$

The algorithm presented is simpler than the algorithm presented by Wieckowski et al. (1999) and avoids the need to specify any penalty parameters. However, it will be demonstrated in the following that useful results are obtained.

A state of plane strain is prescribed. In the dynamical model the soil column will collapse, as it is not supported in the $x$-direction on its sides. The dynamic simulation is performed with a time step of $\Delta t = 0.001$s. The simulation is performed until the soil has reached a state of vanishing velocities. For the present model the time of the collapse is $t = 2.5$s. The initial configuration consists of 1800 material points. The adaptive material point splitting is employed as described in Section 3.4. The final configuration consists of 9402 material points. Figure 5.2 shows the volume occupied by material points at different instances of time. In the final configuration it is possible to recognize the corners of the column from the initial configuration due to the presence of a small cohesion. The first test involves comparing the stresses at the individual material points to the normal stresses calculated by Eq. (4.19). Figure 5.3 and Figure 5.4 show the dynamical evolution of the vertical normal stress as obtained at the individual material points and calculated by Eq. (4.19), respectively. It is clearly seen that the visualization using mapping via the grid nodes provides a realistic evolution of the vertical normal stresses while the visualization of the individual material-point stresses yields a very noisy stress field.

Secondly, the material-point splitting is explored. As no very localized strains are present, the splitting scheme of Section 3.4 is employed. Figure 5.5 shows the deformed configuration of the right half of the soil column with and without the utilization of the proposed material point splitting scheme. As seen, the splitting algorithm significantly enhances the kinematic description of the deformation pattern.

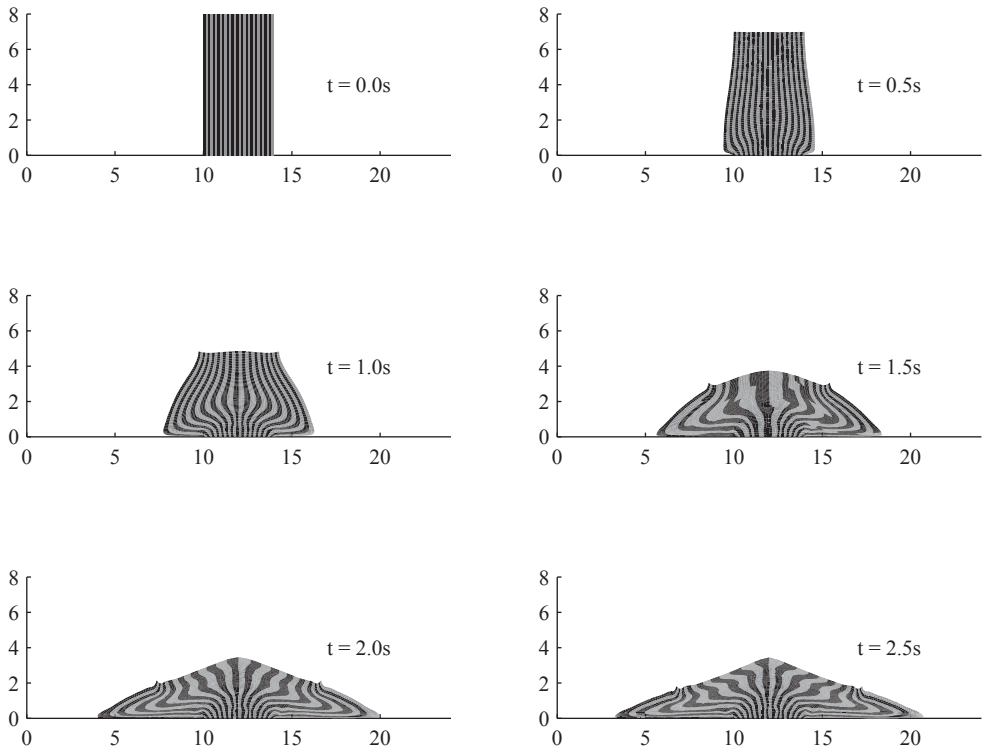


**Figure 5.2** Deformation pattern for the collapsing soil column at different times. The figure uses patching of the corners of the material points. The location of corners in the deformed configuration is calculated using the deformation gradient.

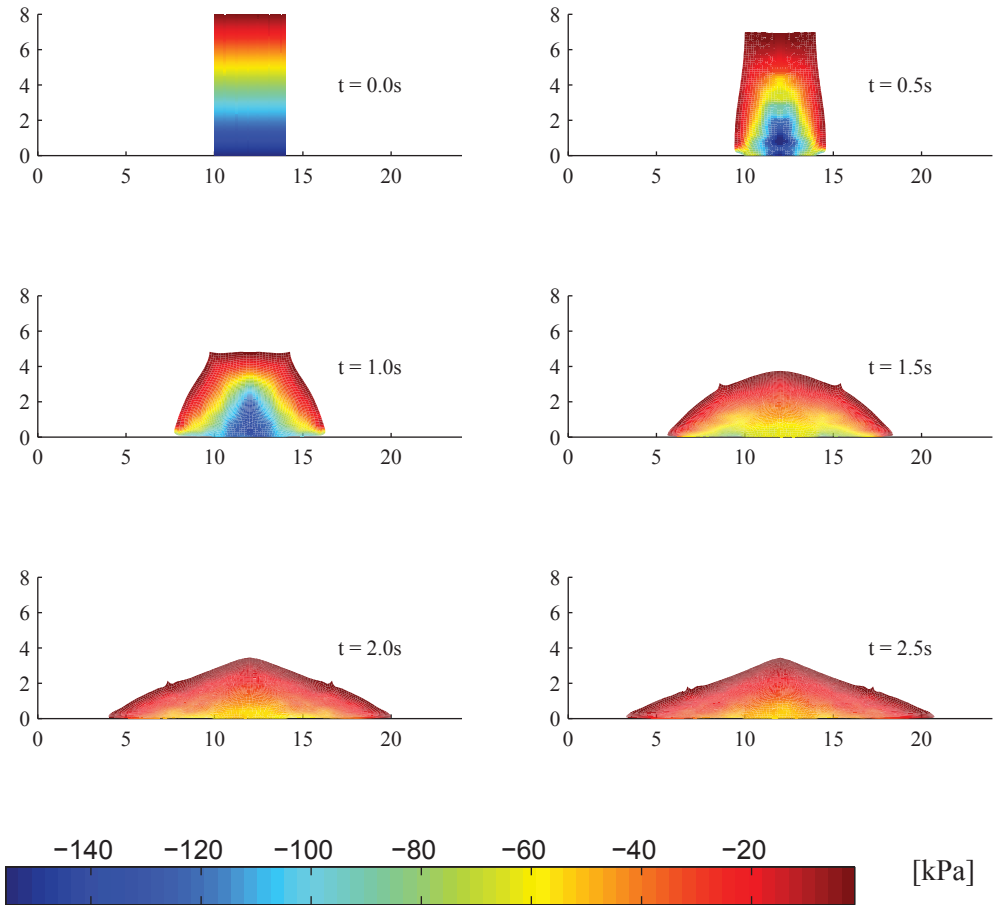


**Figure 5.3** Vertical normal stress visualization using Eq. (4.19).

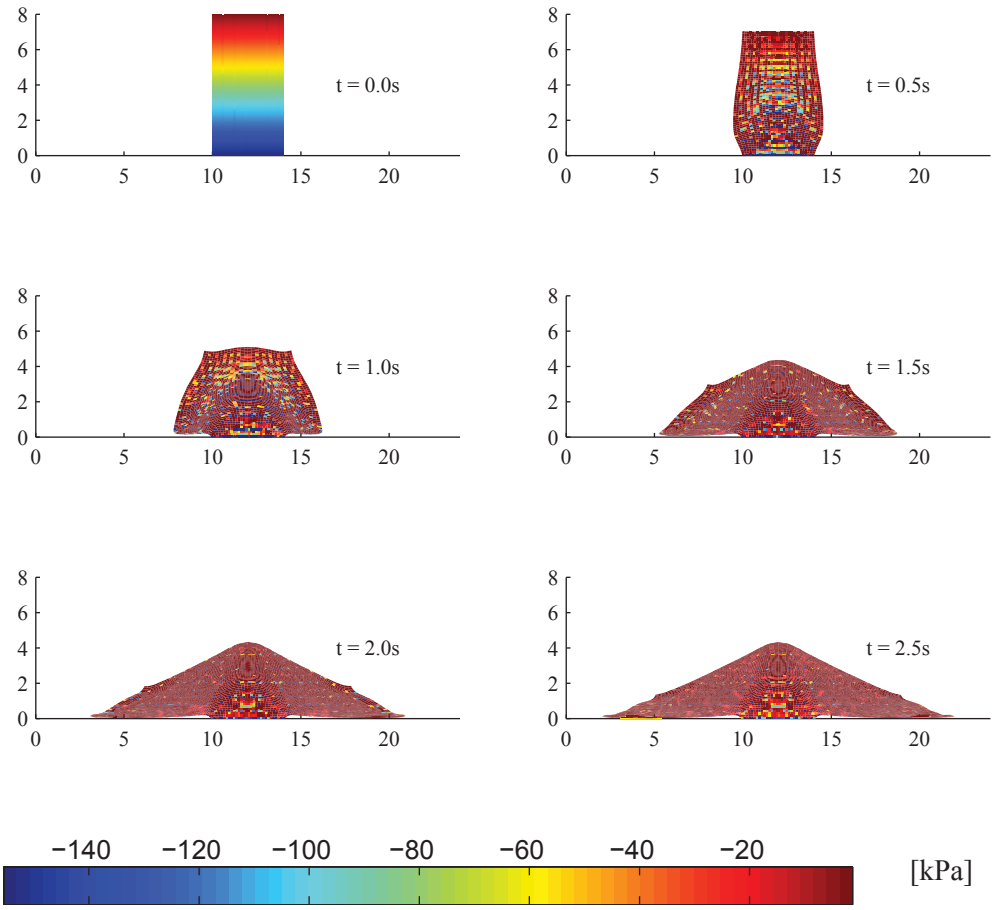


**Figure 5.4** Vertical normal stresses at the individual material points.

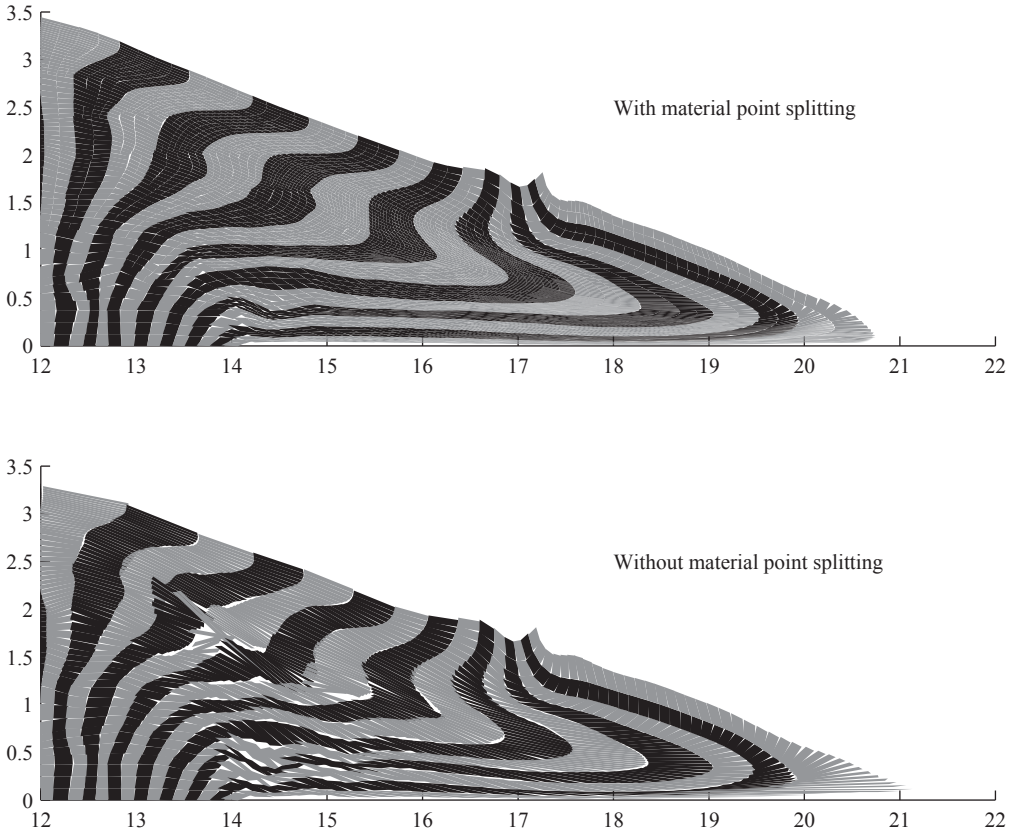


**Figure 5.5** Comparison of the deformation with and without application of the splitting algorithm.

## 5.2 Dynamical modelling of landslides using the large-strain material point model

As described in Section 1.2, a typical scenario for slope collapse is that the strength of upper soil layers is reduced. This can be due to several factors. Examples from Section 1.2 include saturation of partially saturated slopes, thaw in permafrost soils, reduction of shear strength of roots from vegetation on the slope. The work by Huang et al. (2009) analyses how rainfalls increase the soil moisture content and change the pore water pressure from negative (capillarity) to positive. The authors present laboratory tests showing how rainfall induced collapses occur. Similar observations were reported at the landslide at Rubjerg Knude in northern Denmark. Here a major slide took place near the beach due to a slip between the interface between clay and sand layers. The Danish news (Tv2Nord 2008) report that the cause of the slide probably was that major rainfall increased the total weight of the clay, exhausting the adhesion at the interface.

Depending on the type of the slide, different material models can be considered in order to analyse the collapse. In case of rock materials breaking off from the bulk of a rock slope, rock mechanics need to be considered in order to adequately describe the processes leading to landslides. This includes landslides of slip types, for instance in cracked clayey soils. Other kinds of landslides involve that the total stability of a slope is exhausted, caused by either an increase of load of a decrease in strength.

Another aspect involves how to describe the dynamics of collapsing soil. In the case of the rock falls or rock slides, each rock may be represented as a discrete element or particle. Further, for sand, numerical tools for describing the interaction between individual sand grains exists such as the work by Belheine et al. (2008). However, for realistic problems it is not possible to represent each rock or sand grain. Consequently, the dynamics need to be described using continuum mechanics.

Here a study of collapsing soil is performed using the assumption that both the stress redistribution leading to the initiation of the slide and the constitutive response during the landslide can be approximated using an elasto-plastic material model. This analysis utilizes the ideas of Chapters 4 and 4.

A geometrically simple, two dimensional model is introduced for representing the geometry of a typical slope. The geometry of the slope is presented in Figure 5.6. By using a dynamical time integration using the material-point method, collapse of the slope is analysed. The slope is considered a continuum material. In this example, only slopes consisting of homogenous, isotropic soil material are analysed. No water pressures are present, hence a total stress formulation is employed. An elasto plastic material model is employed to analyse the collapse of the slope. In the initial state, the slope is considered to be at rest with an elastic distribution of stresses. If the elastic stress distribution cannot be sustained for a sufficiently large part of the soil a failure mechanism will develop.

Using an elasto-plastic framework, the reduction of soil strength leading to landslides is probably best described as a reduction of the cohesion. The Mohr-Coulomb framework described in Section 5.1 is utilized to model the elasto-plastic response.

In order to study the dynamical collapse, an initial stress state needs to be determined. The initial stresses are determined using the incremental gravitation scheme described in Section 4.3, where the gravity is gradually increased. Applying the gravity in this way ensures that the slope is in equilibrium with respect to elastic stresses. Hence, the collapse of the slope will be due

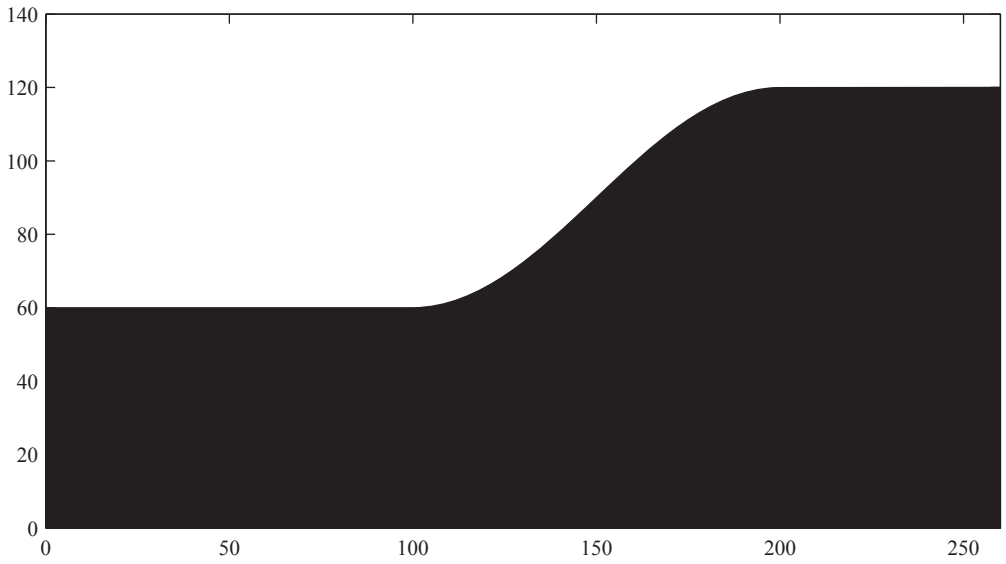


**Figure 5.6** Geometry for a representative soil slope.

to the initiation of plastic yielding. Further, the slide will first start, when a sufficient part of the material points are in a state of plastic response. This is in agreement with the geotechnical models of slope stability.

The discretization involves representing the slope of Figure 5.6 as a finite set of grid nodes and material points. The model is employing a regular computational grid. The discretization employs three by three material points per cell. The interpolation between material points and grid nodes is performed using the GIMP-interpolation functions defined by Bardenhagen and Kober (2004). The algorithm for determining GIMP functions in the deformed geometry described in Paper II is employed.

The slope is defined with homogenous material properties for the entire slope. An initial density of $\rho^0 = 2000\text{kg}/\text{m}^3$, a Young's modulus of $E = 40\text{MPa}$ and a Poisson ratio of $\nu = 0.42$ are employed. The boundary conditions prevent horizontal movement at the vertical boundaries and vertical movement at the lower boundary. This is enforced by prescribing zero velocity components and resulting force components at the grid nodes representing the boundary.

Ideally, since a finite part of an infinite soil domain is modelled, transmitting boundary conditions should be applied along the artificial boundaries. Such boundary were proposed by, amongst others, Higdon (1990) handle both the $p$-waves and the $s$-waves. Analysis of radiation boundary conditions with finite- element examples are presented by Krenk and Kirkegaard (2001). An implementation of a silent boundary scheme within the context of the material-point method is presented by Shen and Chen (2005). However, in the present analysis useful results are obtained without transmitting boundary conditions since plastic response damps the waves propagating in the model.

Figure 5.7 shows the initial setting of material points and grid nodes for a model using

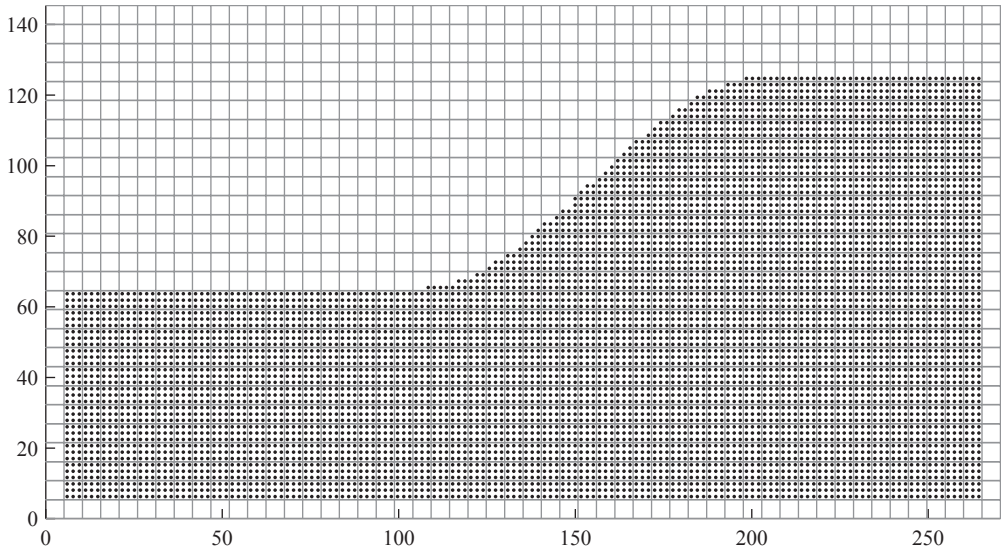


**Figure 5.7** Initial configuration of material points and nodes.

7127 material points. The incremental gravitational scheme leads to initial fields of stresses and corresponding elastic displacements. Figure 5.8 shows the initial state for the model consisting of 7127 material points.

Paper II shows that the initial stress and displacement fields determined by the incremental gravitation are in agreement with the fields obtained by commercial finite element software. The state determined by the incremental gravitation scheme is used as the initial state for the dynamic study of the slides. Hence, for a fixed spatial discretization, the initial state only needs to be calculated once.

Performing dynamical analysis using different sets of friction angles and cohesion, it is concluded that if the soil of the slope is purely frictional, it is stable if the friction angle is larger than approximately $35°$. Similarly, if the slope consists of a uniform cohesive soil with no friction, a the slope is stable for a cohesion larger than approximately $400$kPa. Further, the inclusion of a small friction angle when representing cohesive soils seems to be preferable due to the shear stresses present at the lower boundary (the middle right illustration in Figure 5.8). For low frictions angles and no cohesion, an unrealistic failure will be observed along the lower boundary, when the dynamic time integration is performed using the Mohr-Coulomb yield criterion. As an illustration of this, a combination with $\phi = 5°$ and $c = 175$kPa yield a stable slope in the numerical analysis while failure will be observed for $\phi = 0°$ and $c = 300$kPa.

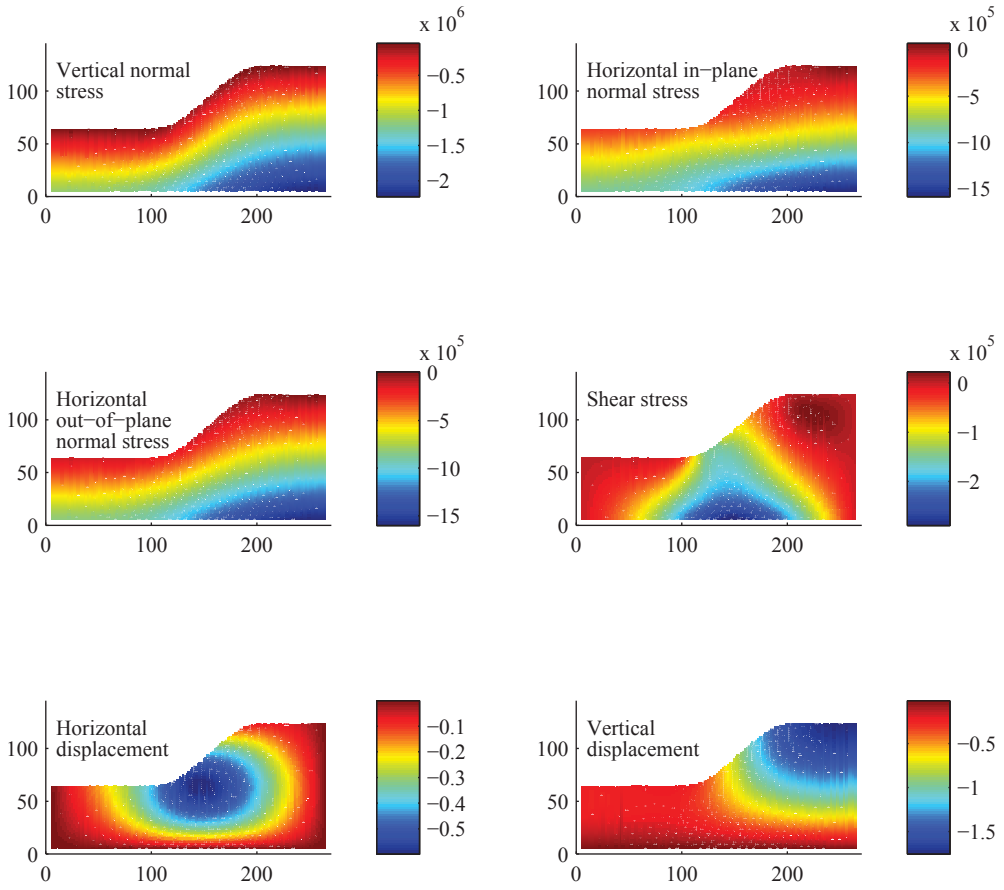


**Figure 5.8** Initial stress and displacement state as a result of gravity. The visualization of the stresses are performed using Eq. 4.19.

### 5.2.1 Analysis of material point splitting

Paper II performs an analysis of landslides using GIMP. Here we analyse, how the large strain modifications suggested are able to improve the modelling of the localized deformations. The dynamical collapse of a slope with $\phi = 18^\circ$ and $c = 5$kPa is explored. The discretization shown in Figure 5.7 with 7126 material points in the reference configuration is employed. Firstly, the collapse is studied, where no splitting criterion is employed. Figure 5.9 shows the collapse as a function of time when no splitting criterion is enforced for a model with $\phi = 18^\circ$ and $c = 5$kPa.

Figure 5.10 shows how the slide progresses as a function of time for a model with the same material properties and the splitting algorithm proposed in Section 3.4 Finally, Figure 5.11 shows the deformation as a function of time employing the combined splitting algorithm of Section 3.4 and Section 3.4.2. As seen, this slide involves significantly localized deformations. The deformations are concentrated where the collapsing slope meets the flat soil surface. Comparing Figures 5.9 to 5.11 its is seem that the concentrated shear deformation makes the kinematic description problematic, in case that no splitting occurs. A careful look at the deformation pattern on Figure 5.9 shows that the voxels associated with the material points that undergoes the largest distortion has obtained needle-likes shapes. This is a consequence of the extremely large and localized strains due to the elasto-plastic collapse. When no splitting is enforced, the voxels associated with the material points becomes severely distorted. However, as seen from Figure 5.9, the splitting criterion dealing with extreme shear strains avoids the tendency for material points to obtaining needle-like shapes.

Comparing to Paper II, it is noted that the tracking of the deformed state by calculating the position of the voxel corners using the deformation gradient tensor leads to a much better visualization of the deformation. In the following simulations all results are presented using the material-point-splitting scheme presented in Sections 3.4 and 3.4.2.

### 5.2.2 Analysis of the stresses in the collapsing slope

As mentioned, one problematic issue regarding the material-point method relates to the fact the governing equations are solved at the grid nodes, while the constitutive response is evaluated at the material points. This may be a concern, as stresses at the individual material points may be unrealistic even though the overall solution may still yield sensible results. Figure 5.12 shows the stresses at the material points

Comparing Figure 5.11 and Figure 5.12, it is observed that the physically unrealistic stress concentrations are observed where the largest deformations occur.

The unrealistic stress distributions observed in Figure 5.12, which is representative for the kind of stress oscillations observed in general large strain problems, has been a concern when evaluating the quality of the simulations performed in this research. Especially for the elasto-plastic material response, as the return mapping applied to enforce the yield criterion uses the material point stresses illustrated in Figure 5.12.

However, the deformations, velocities and the deformation gradient tensor all shows a smooth and physically realistic variation during the landslide. Paper I shows, that for the cantilevered beam, the shear stresses at the material points are unrealistic for MPM using linear interpolation. But if the stresses are interpolated to the grid nodes, the stresses make sense. Figure 5.13 shows the stresses at the end of the slide calculated by Eq. (4.19). As seen, the stresses are realistic when mapped via the grid nodes, but show significant non-physical oscillations at

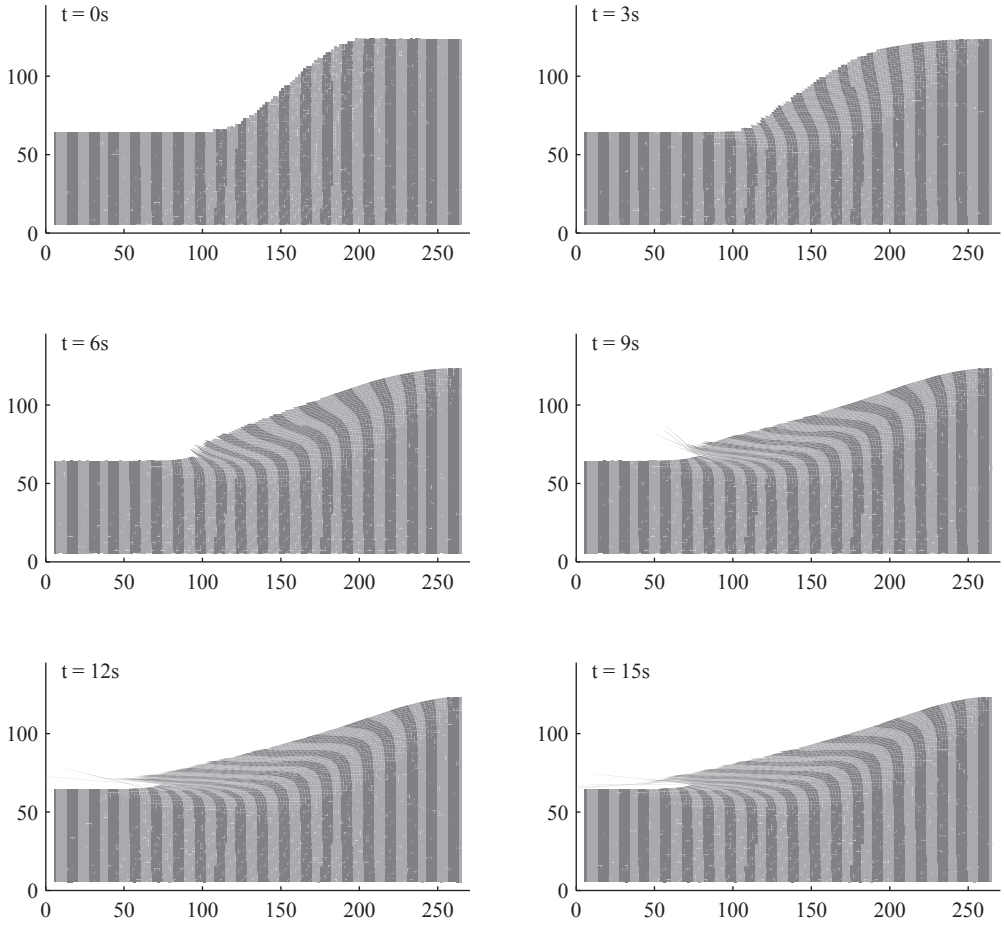


**Figure 5.9** The landslide progression as a function of time for a slide with the elasto plastic properties of $\phi = 18^\circ$ and $c = 5$kPa. The shades is solely for illustration of the deformation. This simulation is performed without the application of material point splitting.

the individual material points. Hence, when the governing equations are solved at the grid nodes, the results are expected to make sense. However, the unrealistic stresses at the material points still provides a concern, as the individual material points is utilized to evaluate the constitutive response. Hence, for improving the consistency of the material-point method the integration of the stresses in time should be further addressed. As shown by Andersen et al. (2009) and discussed in Chapter 4, the elasto plastic behaviour may still be realistic, although the shear stresses behave very erratically.

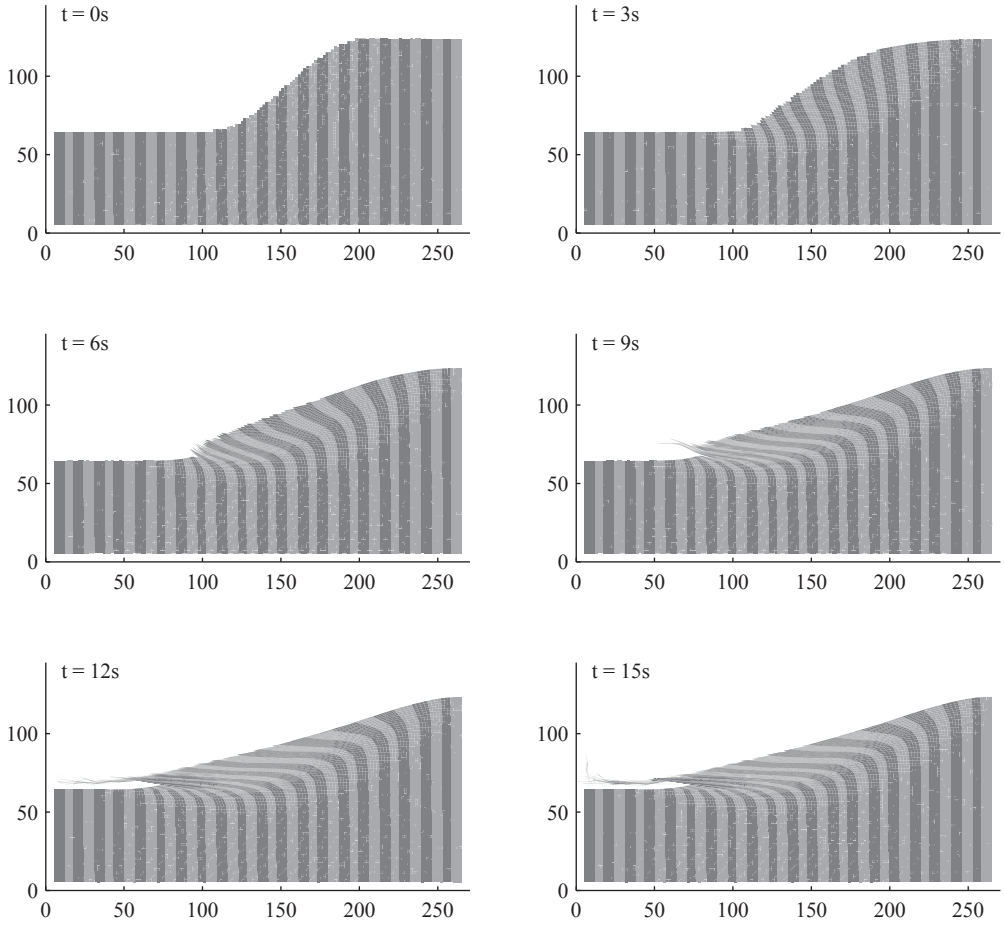


**Figure 5.10** The landslide progression as a function of time for a slide with the elasto plastic properties of $\phi = 18°$ and $c = 5$kPa. The shades is solely for illustration of the deformation. This simulation is performed using the splitting algorithm presented in Section 3.4.

### 5.2.3 Influence of the material strength

In order to understand how landslides develop in slopes of different kinds of soil, a number of simulations have been performed, all starting from the initial state displayed in Figure 5.8. The result of performing the dynamical analysis using different material properties is illustrated in Figure 5.14 and Figure 5.15. Figure 5.14 shows the deformed configuration at the end of the slide for a frictional soil slope with $c = 5$kPa for friction angles of 15, 18, 21, 24, 27 and 30 degrees, respectively. If the small cohesive strength is not included, the localized deformations at

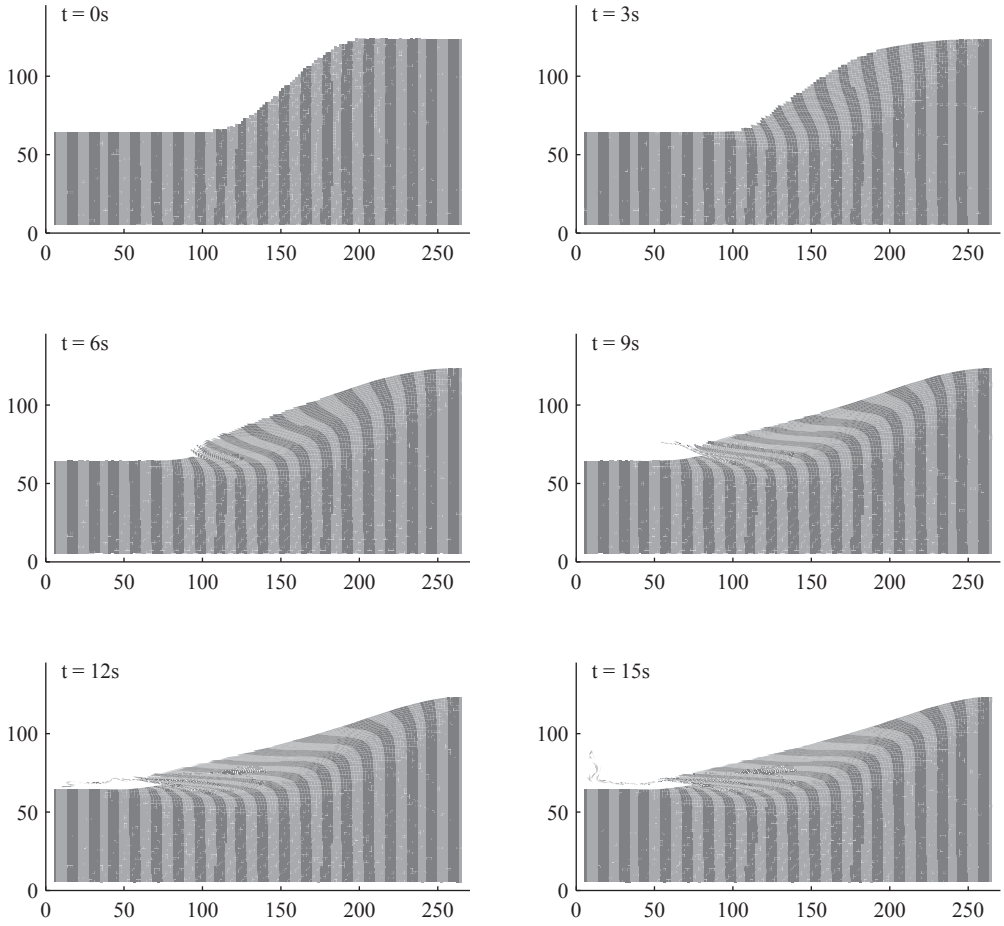


**Figure 5.11** The landslide progression as a function of time for a slide with the elasto plastic properties of $\phi = 18°$ and $c = 5$kPa. The shades is solely for illustration of the deformation. This simulation is performed using the splitting algorithms presented in Section 3.4 and Section 3.4.2.

the top soil layers get too large to adequately describe the kinematics using the proposed method of Section 3.2. In this case, the voxels associated with the material points will undergo extreme deformations, as the resistance to shear deformations vanishes with diminishing overburden pressure.

For very dense sands with friction angles above approximately 35 degrees, the soil is known to expand as a result of plastic deformations. However, as the angle of friction for which no landslide occurs is rather low, $\psi = 0°$ is utilized for all the models. As seen, extreme localized

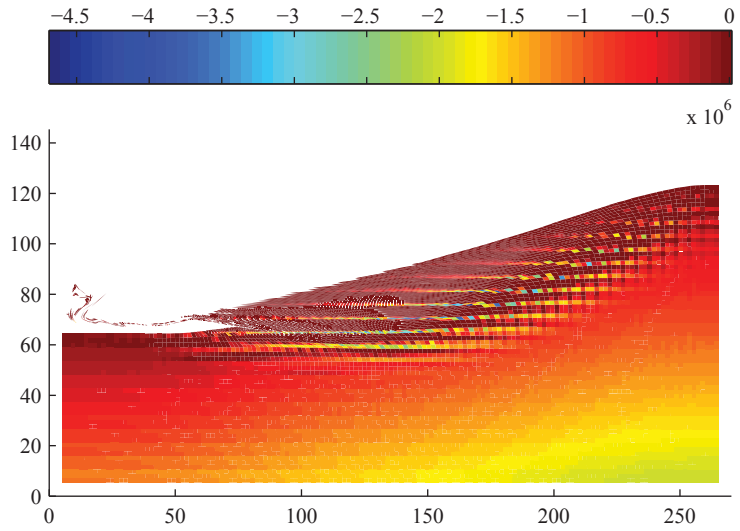


**Figure 5.12** The vertical normal stresses at the individual material points at the end of the slide for the slope with the strength properties $\phi = 18°$ and $c = 5$kPa. Significant non-physical, un-smooth stresses are present.

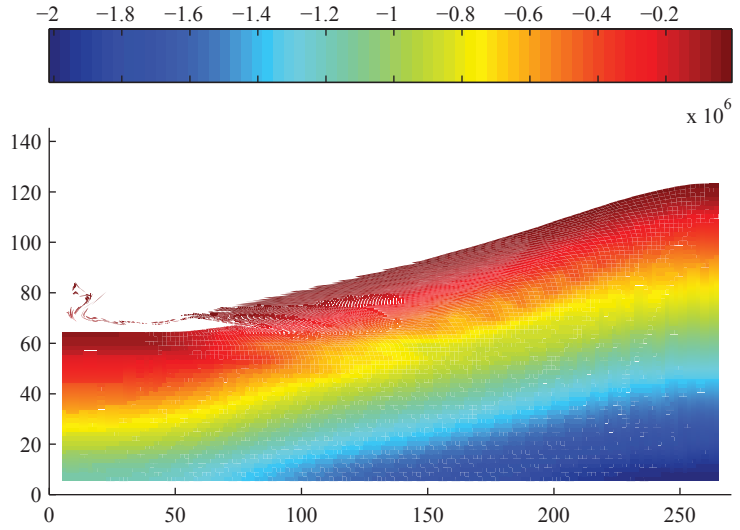


**Figure 5.13** The vertical normal stresses at the end of the slide calculated by Eq. (4.19). The numerical model is not changed, only the visualization of the stresses is changed.

deformations are taking place near the crest, where the sliding soil meets the horizontal soil surface. For the weakest sand slope with $\phi = 15°$, the strain localization is too extreme to handle using the presented discretization. Consequently, material points leave the bulk of material and

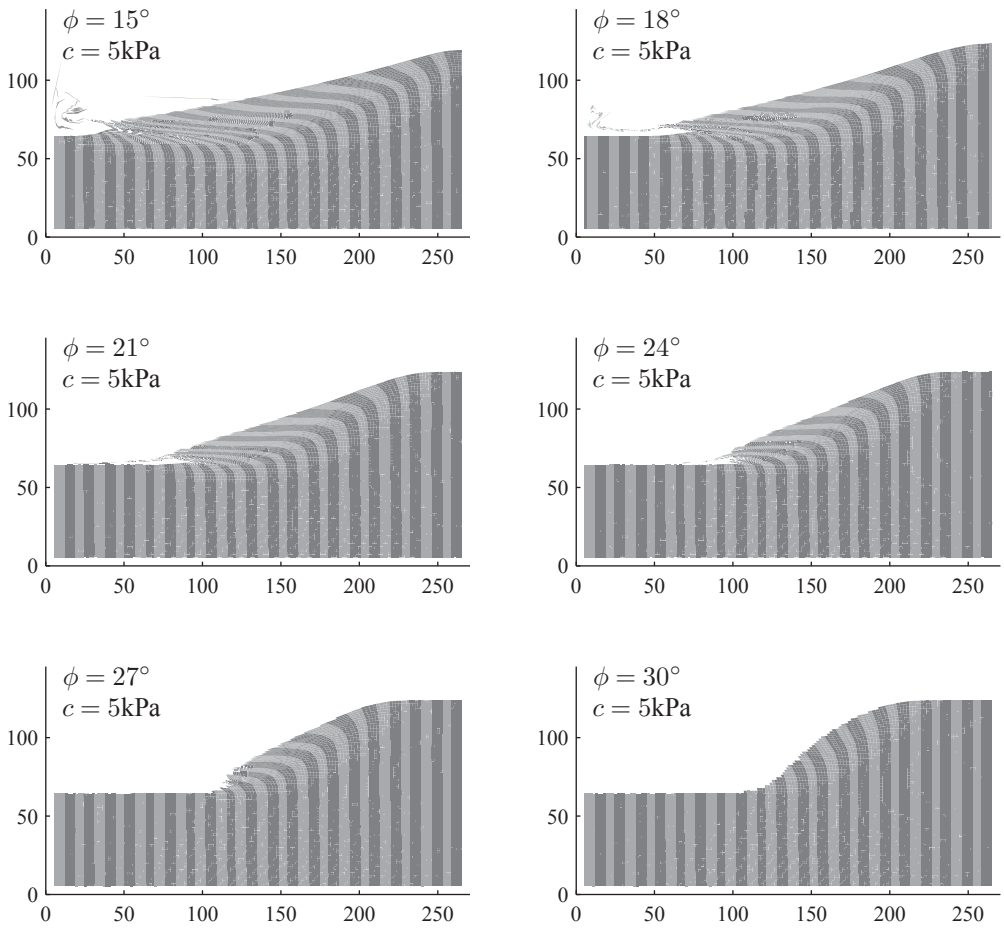


**Figure 5.14** Deformation patterns for landslides in sand slopes with varying amount of friction. As expected a lower strength implies a larger slide.

move as free bodies, undergoing extreme shear deformation.

Similarly, Figure 5.15 shows the deformation patterns in a cohesive soil slope with $\phi = 5°$ for cohesions of 25kPa, 50kPa, 75kPa, 100kPa, 125kPa and 150kPa, respectively. The inclusion of a small friction angle is aimed to ensure that a total collapse of the model does not occur due to the shear stresses present at the lower boundary of the computational model (See Figure 5.8).

Besides the extent of the slides, the speed of the soil during the slides is important to evaluate the potential hazards to urban environments next to unstable slopes. In order to get an idea of the

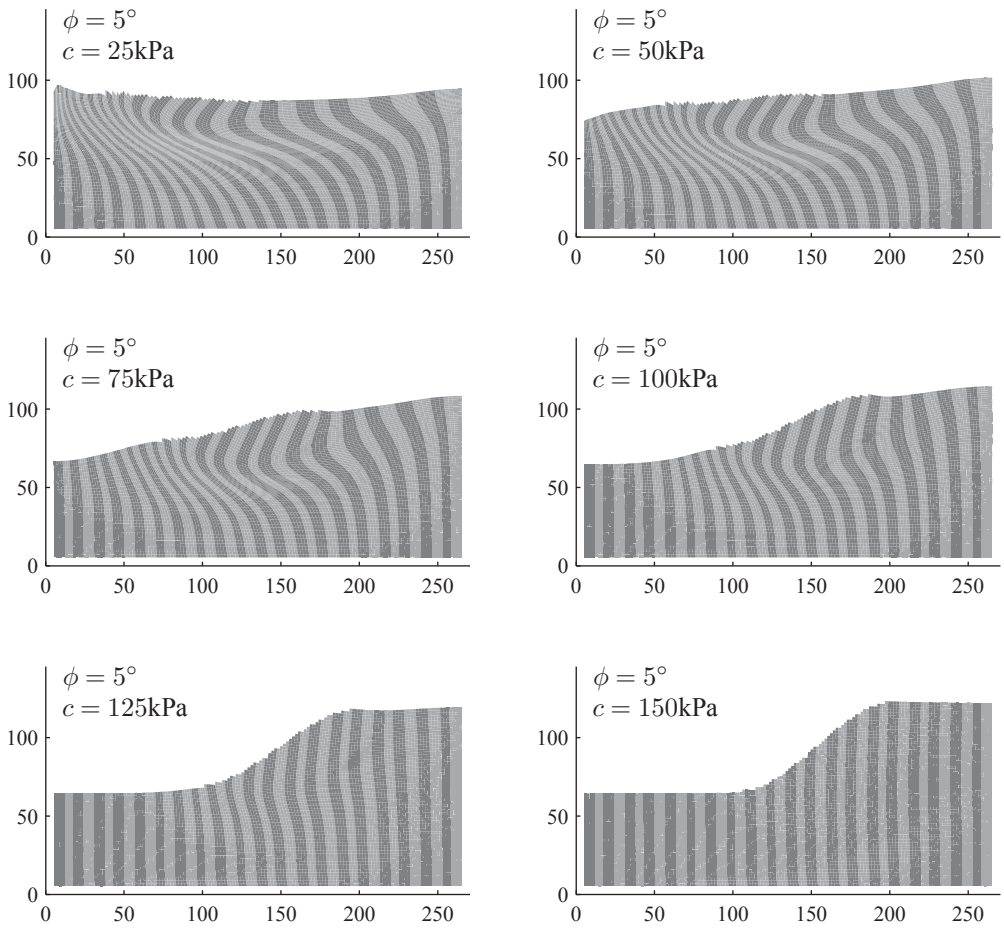


**Figure 5.15** Deformation patterns for landslides in clay slopes with varying amount of cohesion. As expected a lower strength implies a larger slide. For the slope with $\phi = 5°$ and $c = 150$kPa, the plastic deformations are negligible. For the weakest clay slope with $c = 25$kPa, the slide has actually hit the boundary left boundary.

speed of the collapsing slope, mass weighted speeds of material points are defined by

$$v_{average} = \frac{\sum_{p=1}^{N_p} ||\mathbf{v}_p|| m_p}{\sum_{p=1}^{N_p} m_p}. \tag{5.12}$$

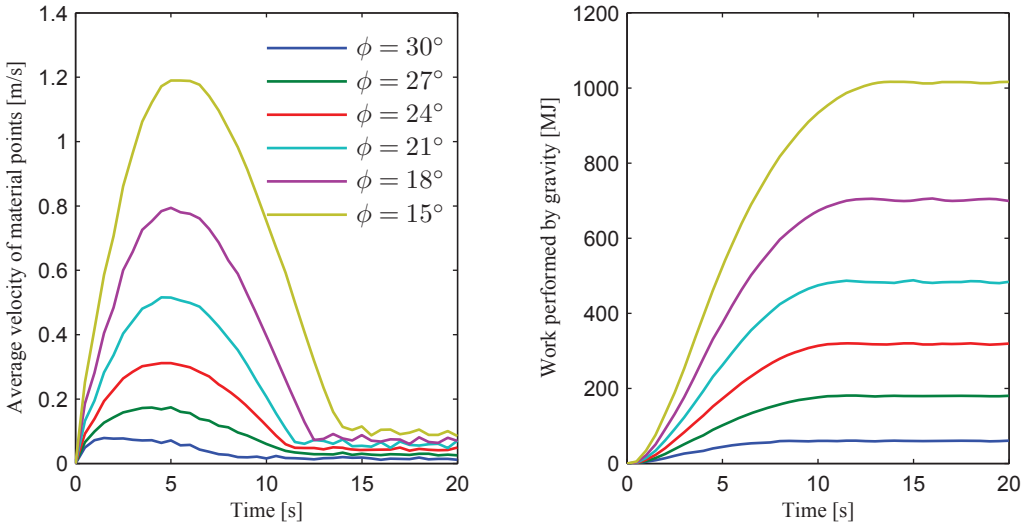


**Figure 5.16** Average speed and work performed by gravity as as function of time for slopes consisting of frictional soils with $c = 5$kPa and varying friction angles.

In order to get an idea of the extent, the work done by gravity is calculated as

$$W_{gravity} = \sum_{p=1}^{N_p} m_p \, \mathbf{g} \cdot \mathbf{u}_p, \tag{5.13}$$

where $\mathbf{g}$ is the vectorial representation of gravity and displacement is given by $\mathbf{u}_p = \mathbf{x}_p - \mathbf{x}_p^0$, where $\mathbf{x}_p^0$ is the position at the start of the dynamical simulation.

Figure 5.16 shows the speed of the bulk and the work done by gravity as a function of time for a slope consisting of frictional soil with $c = 5$kPa and varying amount of friction.

Finally, Figure 5.17 shows the results for frictional soils regarding the areas of elastic and plastic response, 4 seconds into the slides.

As noted, all the slides has yield lines defining the areas of plastic response defined. Further, the areas of plastic response are dependent on the angle of friction. In the slopes with lower strength, the areas of plastic response are larger and consequently the extent of the slide increases.

### 5.2.4 Influence of the spatial discretization

As seen from the previous subsection, in particular for slides on frictional slopes, significant localization of the strains occurs, especially where the collapsing slope hits the flat soil surface. In the present framework, material points were allowed to split where localized deformations are present, but the initial discretizations were the same for the all the models. Now, the influence of the initial discretization is studied. Figure 5.7 shows a setting of material points and cells with 50 by 27 quadratic cells defining the set of grid nodes. The spacing between material points in the reference configuration is three times less than the spacing between grid-nodes. Figure 5.18 shows the results of varying the number of cells to represent the problem. In the

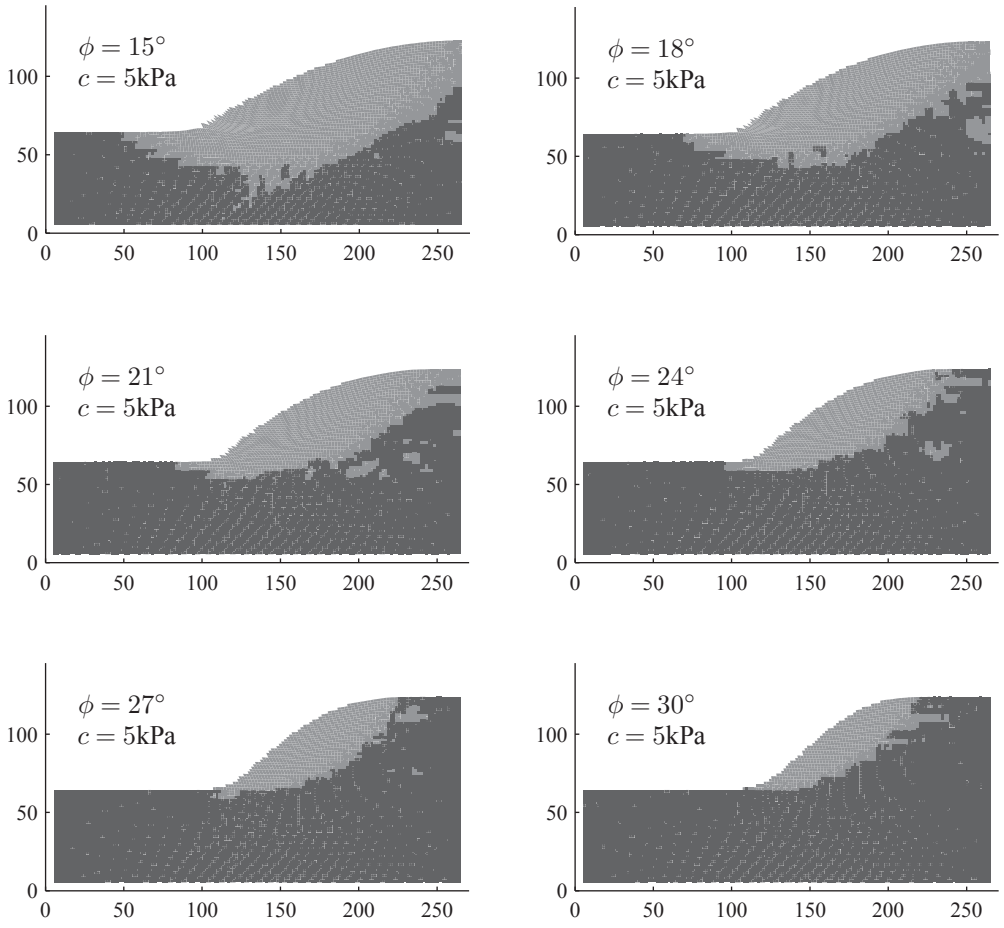


**Figure 5.17** Failure mechanisms for the different soils, 4 seconds into the slides. The dark shade denotes material points with elastic response while the brighter shade means plastic response.

$x$-direction, 20, 30, 40, 50, 60 and 70 are employed. The number of cells in the $y$-direction and the number of the material points increases accordingly. As seen from Figure 5.18, the extent of the slide is similar for the models using 50, 60 and 70 cells in the horizontal direction. Further, it is noted that all the presented models have troubles in describing the parts of the slope undergoing the most significant deformations. As a consequence, the material points undergoing extreme deformations become distorted, obtaining needle-like shapes. Perhaps, a better scheme for splitting material points, using the framework for tracking the deformed geometry presented in Section 3.4 and 3.4.2, may improve this. Another problem is that the continuum assumption

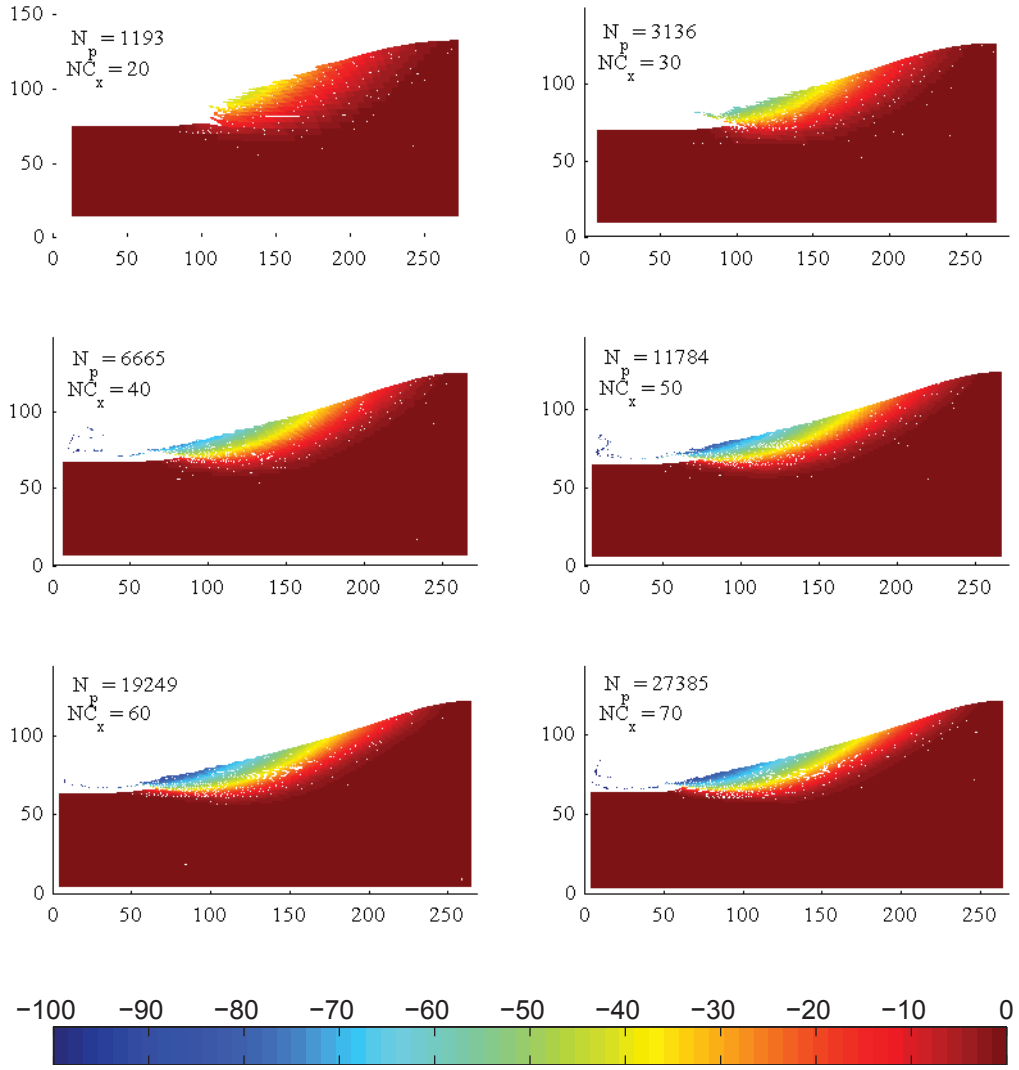


**Figure 5.18** Horizonal displacement of material points. A slope with the $\phi = 18°$ and $c = 5$kPa is considered. $N_p$ is the number of material points at the end of the slide, and $NC_x$ is the number of grid-cells in the horizontal direction.

is not realistic, where the largest deformations are present. Here an algorithm for describing how material points can leave the continuum material and move relatively to the slope would probably present an improvement. An idea may be to combine the material-point formulation with a discrete element formulation.

# CHAPTER 6
# Conclusions

Firstly, an overview of the thesis is presented. Secondly, overall conclusions and discussion of the results are presented. Finally, several ideas for future research, utilizing the ideas of the thesis, are presented.

## 6.1 Summary of the thesis

The first chapter analyses the different types of landslides and reviews geological landslide surveys, geotechnical slope stability methods and modern computational methods that have been applied to study landslides. Chapter 2 presents a state-of-the-art review of the material-point method (MPM) and the generalized interpolation material point method (GIMP).

The Chapters 3 and 4 deal with several new ideas for material-point method analysis of large strain problems. The material point method is a very attractive method when dealing with large strain problems, as it avoids drawbacks associated with pure Lagrangian or pure Eulerian methods. However, several challenges arise, as it is very hard to evaluate obtained results. This is expressed in the work by Steffen, Kirby, and Berzins (2008) as: "The lack of an analysis framework for MPM, as is found in FEMs, makes it challenging to explain anomalies found in its employment and makes it difficult to propose methodology improvements with predictable outcomes".

Chapter 3 presents a number of novel approaches to the analysis of large-strain problems. Firstly, a consistent framework for maintaining objective stresses throughout the time integration is presented. In order to achieve the above-mentioned goal: "propose methodology improvements with predictable outcomes", a deep understanding of the obtained results is important. For visualization of deformation patterns in large-strain problems, a new way of visualization is presented, where a quadratic voxel is associated with each material point in the reference state. The deformation tensor is introduced as a state variable for each material point and utilized to calculate and visualize the voxel in the deformed state. This formulation is utilized to calculate GIMP-weighting functions in the deformed state using Gauss quadrature over each of the voxels. Further, the tracking of the deformation is utilized to present a framework for dynamic refinement utilizing the concept of splitting the material points. The idea is based on splitting material points, where large strains occur in order to avoid extreme deformation of individual points.

Chapter 4 discusses how stresses are handled in the material-point method. Firstly, a scheme for maintaining objective stresses throughout the dynamic time integration is presented. Secondly, the concept of grid-crossing errors is discussed. The chapter also explores how quasi-static stress distributions can be obtained utilizing incremental gravitation. Further, the concept

of selective integration in order to avoid parasitic shear stress are discussed. One of the main results presented is a new way to extract physically realistic stress fields by interpolating the material-point stresses via the computational grid.

Finally, Chapter 5 explores the concepts presented in Chapters 3 and 4 by numerical examples. The first example involves numerically modelling the collapse of a soil column while the second example involves numerical modelling of a collapsing slope. The examples explores several new ideas not discussed in the three research papers found in the appendices.

## 6.2 Overall conclusion

When comparing the finite-element method (FEM) and the material-point method, the most significant difference between them is that in the material-point method, the material points may have an arbitrary placement in the elements that define the set of grid nodes, where the governing equations are solved, whereas fixed integration points are used in the FEM. Further, if using a set of a grid nodes that is spatially fixed in time, material points may move between different cells between the time steps. As demonstrated here and in several other references, this leads to errors when calculating internal forces, denoted grid-crossing errors. This leads to unphysical acceleration variations between the different material points. As demonstrated, these unphysical accelerations leads to unrealistic stress variations between the different material points. In the original MPM formulation using linear shape functions, this effect is most pronounced.

Two approaches can be taken to reduce the effects of grid crossing. The first involves defining a set of higher order interpolation functions for the grid nodes. This approach is studied in Paper I, where interpolation using linear shape functions, quadratic elements and cubic-spline interpolation are compared. As shown, defining a spatially fixed grid by a set of quadratic elements is unfortunately not consistent with the MPM formulation. The cubic-spline interpolation on the other hand displays some advantages, as the field quantities as well as the gradients now vary in a smooth fashion. However, when dealing with large deformations that may have a localized nature, the non-compact nature of the cubic-spline interpolation is expected to cause anomalies. The other approach is known as the generalized interpolation material point method (GIMP). The GIMP formulation defines a volume associated with each material point, a so-called voxel, where a particle characteristic function is defined. The interpolation is then determined by weighting functions that are integrals of the nodal shape functions over the domain of the particle characteristic functions. When dealing with large-strain problems, the GIMP formulation has some attractive features. Firstly, the compact nature of the mapping observed in MPM using linear interpolation is maintained. Secondly, the particle characteristic functions define another way of understanding the presented results, as quantities are now represented over a volume. Hence, it is possible to define new, non-overlapping voxels with new material points defined at the centroids of the new voxels.

Often, the deformations occurring in geotechnical problems due to plastic collapse of the soil are of a very localized nature. What is essentially needed is the ability to refine the discretization of the physical problem during the analysis. As shown in the numerical examples, the use of material-point splitting significantly enhances the kinematical description.

Several pitfalls of the material-point method in its present form is explored. One pitfall pertains to the fact that material response is evaluated at the material points while the equation of motion is solved at the grid nodes. As shown, the stresses at the individual material points are

not realistic. Only when integrated on the grid nodes, realistic stresses are found. This is a major concern when material response is non-linear, for instance in the case of plasticity. As shown in numerical studies, slides are physically realistic in respect to for instance friction angle and angle of a collapsing slope, but the application of an elasto-plastic return mapping scheme for each (unrealistic) material-point stress tensor is an issue of concern.

Another issue in respect to large strain analysis of soil involves the continuum assumption. In typical landslides, the initial deformations can adequately be represented as plastic deformations of a continuum material. At a later stage in larger landslides, the neighbouring parts of soil will start to move relatively to each other. As shown in the numerical examples, reasonable representation of very large strain slides can be obtained using the material-point method, representing the soil as a single continuum throughout the deformation process. However, the numerical models have troubles in capturing slides in frictional soils, where deformations are concentrated near the soil surface. In order to represent landslides, where the response changes from continuum motion to a more discrete response, perhaps the material-point method can be combined combined with a true particle-based method such as the discrete-element method. Due to the tracking of the deformed geometry of the voxels associated with the material points, presented in this thesis, it is possible to define discrete particles at any time of the modelling process.

Although the GIMP formulation significantly increases the performance by reducing the grid-crossing error, significant non-physical stress oscillations still exist. Interpreting the results obtained by the MPM solution scheme, especially in conjunction with the problematic stress updates, is discussed in detail in this thesis. Firstly, it is concluded that although the stress components at the individual material point may show a noisy variation, smooth, physically realistic stress fields can be extracted by a mass-weighted mapping via the computational grid. Secondly, for elasto-plastic problems, utilizing the Mohr-Coulomb criterion, although the individual Cartesian stress components at the material points vary in an erratic fashion, the elasto-plastic response seems to be well defined. For the landslide example discussed in detail in this thesis, this effect is illustrated by visualizing whether the individual material points are in an elastic or a plastic state. Using such a visualization, well-defined failure mechanisms are observed. This is noteworthy, considering the fact that the individual stress components are unrealistic at the material point level. This suggest that the method works well with these relatively simple constitutive models, but also identifies a potential pitfall for implementing more complicated constitutive models.

Conclusively, as fields test results involving the dynamics of large-strain landslides are impossible to obtain, the material-point method provides a tool for increased understanding. This thesis analyse collapsing slopes and provides some moderation for the material-point method in order to obtain better models for large-strain problems. Finally, this thesis discusses some pitfalls of the material-point method.

## 6.3 Recommendations for future research

The research in this thesis has focused on developing new ideas connected to large-strain problems. One of the important ideas involves dynamic refinement by splitting material points. The large-strain formulation along with spatial representation of the GIMP, where state variables are defined as constants within each voxel, provide a robust framework for *how* to split material points. However, a more robust framework for *when* to split material points is needed as the splitting criteria suggested in the thesis are very heuristic.

Further, an open question for the material-point method is if it is possible how to provide a framework for updating the stresses, where the stresses for general problems are more realistic at the individual material points. In the thesis, it is shown that although the stresses are generally unrealistic for the individual points, realistic stresses can be extracted via the grid nodes. However, the attempt to utilize these more realistic stresses directly in the computational MPM scheme has been unsuccessful. Thus, evaluation of stresses in the MPM and the GIMP method is an obvious topic for future research.

With respect to the analysis of landslides and other geotechnical problems using the material-point method, several issues are still to be explored. In many landslides, the presence of pore water plays a crucial role. One important triggering factor is that negative pore pressures due to capillary in semi-saturated soil disappears when the soil becomes fully saturated. Hence, the incorporation of a two-phase water-soil model will provide a more realistic framework for understanding a majority of landslide and other geotechnical phenomena. Secondly, in case of many landslides, the continuum approximation seems inappropriate where extreme strains are observed. Hence, a combination of the material-point method with a discrete method may provide a better description of the parts of a slide where extreme localized deformations occur. One potential method may be the discrete-element method. Finally, it is of interest to model other geotechnical problems, where the traditional numerical tools have shortcomings. An example may be numerical modelling of pile driving and cone penetration.

# References


Andersen, L, Andersen, SM, and Damkilde, L (2009). Selective integration in the material-point method. In *Proceedings of the Twenty Second Nordic Seminar on Computational Mechanics*, Aalborg, Denmark. Aalborg University.

Andersen, SM and Andersen, L (2008). Modeling of landslides with the material point method. In *The Sixth International Conference on Engineering Computational Technology*, Athens, Greece. Civil-Comp Press.

Apuanui, T, Corazzato, C, Cancelli, A, and Tibaldi, A (2005). Stability of a collapsing volcano (Stromboli, Italy): Limit equilibrium analysis and numerical modelling. *Journal of Volcanology and Geothermal Research* **144**, 191–210.

Babuška, I and Miller, A (1984). The post-processing approach in the finite-element method - part 1: Calculation of displacements, stresses and other higher derivatives of the displacements. *International Journal for Numerical Methods in Engineering* **20**, 1085–1109.

Bardenhagen, SG (2002). Energy conservation error in the material point method for solid mechanics. *Journal of Computational Physics* **180**, 383–403.

Bardenhagen, SG, Brackbill, JU, and Sulsky, D (2000a). The material-point method for granular materials. *Computer Methods in Applied Mechanics and Engineering* **187**, 529–541.

Bardenhagen, SG, Brackbill, JU, and Sulsky, D (2000b). Numerical study of stress distribution in sheared granular material in two dimensions. *Physical Review* **62**, 3882–3390.

Bardenhagen, SG, Guilkey, JE, Roessig, KM, Brackbill, JU, Witzel, WM, and Foster, JC (2001). An improved contact algorithm for the material point method and application to stress propagation in granular material. *Computer Modelling in Engineering and Sciences* **2**, 509–522.

Bardenhagen, SG and Kober, EM (2004). The generalized interpolation material point method. *Computer Modelling in Engineering and Sciences* **5**, 477–495.

Belheine, N, Plassiard, J-P, Donzéc, F-V, Darve, F, and Seridi, A (2008). Numerical simulation of drained triaxial test using 3D discrete element modeling. *Computers and Geotechnics* **36**, 320–331.

Belytschko, T, Krongauz, Y, Organ, D, Fleming, M, and Krysl, P (1996). Meshless methods: An overview and recent developments. *Computer Methods in Applied Mechanics and Engineering* **139**, 3–47.

Brackbill, JU (2005). Particle methods. *International Journal for Numerical Methods in Fluids* **47**, 693–705.

Brackbill, JU and Ruppel, HM (1986). FLIP – a method for adaptively zoned, particle in cell calculations in 2 dimensions. *Journal of Computational Physics* **65**, 314–343.

Brydon, AD, Bardenhagen, SG, Miller, EA, and Seidler, GT (2005). Simulation of the densification of real open-celled foam microstructures. *Journal of Mechanics and Physics of Solids* **53**, 2638–2660.

Buzzi, O, Pedroso, DM, and Giacomine, A (2008). Caveats on the implementation of the generalized material point method. *Computer Modelling in Engineering and Sciences* **31**, 85–106.

Chen, H and Hawkins, B (2009). Relationship between earthquake disturbance, tropical rainstorms: an overwiev from Taiwan. *Bulletin of Engineering Geology and the Environment* **68**, 161–186.

Chen, JS, Pan, C, Wu, CT, and Liu, WK (1996). Reproducing kernel particle methods for large deformation analysis of non-linear structures. *Computer Methods in Applied Mechanics and Engineering* **139**, 195–227.

Chen, Z, Hu, W, Shen, L, Xin, X, and Brannon, R (2002). An evaluation of the MPM for simulating dynamic failure with damage diffusion. *Engineering Fracture Mechanics* **69**, 1873–1890.

Clausen, J, Damkilde, L, and Andersen, L (2006). Efficient return algorithms for associated plasticity with multiple yield planes. *International Journal for Numerical Methods in Engineering* **66**, 1036–1059.

Clausen, J, Damkilde, L, and Andersen, L (2007). Efficient return algorithms for non-associated plasticity with linear yield criteria in principal stress space. *Computers and Structures* **66**, 1795–1807.

Cleary, PW and Monaghan, JJ (1999). Conduction modelling using smoothed particle hydrodynamics. *Journal of Computational Physics* **148**, 227–264.

Coetzee, CJ, Basson, AH, and Vermeer, PA (2006). Discrete and continuum modelling of excavator bucket filling. *Journal of Terramechanics* **44**, 177–186.

Coetzee, CJ, Vermeer, PA, and Basson, AH (2005). The modelling of anchors using the material point method. *International Journal for Numerical and Analytical Methods in Geomechanics* **29**(9), 879–895.

Cook, RD, Malkus, DS, Plesha, ME, and Witt, RJ (2002). *Concepts and applications of finite element analysis*. John Wiley and Sons.

Crosta, GB, Imposimato, S, Roddeman, D, Chiesa, S, and Moia, F (2005). Small fast-moving flow-like landslides in volcanic deposits: The 2001 Las Colinas landslide, (el salvador). *Engineering Geology* **79**, 185–214.

Cummins, SJ and Brackbill, JU (2002). An implicit particle-in-cell method for granular materials. *Journal of Computiatonal Physics* **180**, 506–548.

D'Ambrosio, D, Gregorio, SD, Iovine, G, Lupiano, V, Rongo, R, and Spataro, W (2003). First simulations of the Sarno debris flows through cellular automata modelling. *Geomorphology* **54**, 91–117.

Daphalapurkar, NP, Lu, H, Coker, D, and Komanduri, R (2007). Simulation of dynamic crack growth using the generalized interpolation material point (GIMP) method. *International Journal of Fracture* **143**, 79–102.

Dassault Systèmes (2008). *Getting Started with Abaqus: Interactive Edition (v6.8)*.

Deubelbeiss, Y and Kaus, BJP (2008). Comparison of Eulerian and Lagrangian numerical techniques for the Stokes equations in the presence of strongly varying viscosity. *Physics of Earth and Planetary Interiors* **171**, 92–111.

Devoli, G, Cepeda, J, and Kerl, N (2009). The 1998 Casito volcano flank failure revisited - New insights into geological setting and failure mechanisms. *Engineering Geology* **105**, 65–83.

Duarte, CA and Oden, JT (1996). An *h-p* adaptive method using clouds. *Computer Methods in Applied Mechanics and Engineering* **139**, 237–262.

Duncan, JM (1996, July). State of the art: Limit equilibrium and finite-element analysis of slopes. *Journal of Geotechnical Engineering*, 577–596.

Eberhart, E (2003, Apr). Rock slope stability analysis - utilization of advanced numerical teqniques. Technical report, UB C - Vancouver Canada.

Eilertsen, RS, Hansen, L, Bargel, TH, and Solberg, IL (2008). Clay slides in the Målselv valley northern Norway: Characteristiscs, occurence, and triggering mechanicms. *Geomorphology* **93**, 548–562.

Falkovich, G, Gawędzki, K, and Vergassola, M (2001). Particles and fields in fluid turbulence. *Reviews of Modern Physics* **73**, 913–975.

Fan, XM, Xu, Q, Zhang, ZY, Meng, D, and Tang, R (2009). The genetic mechanism for a translational landslide. *Bulletin of Engineering Geology and the Environment* **68**, 231–244.

Furuya, T (2004). Review and comparison of limit equilibrium methods of slices for slope stability analysis. *Bulletin of the Nationial Institute for Rural Engineering, Japan* **43**, 1–22.

Gilmanor, A and Achraya, S (2008). A hybric immersed boundary and material point method for simulating 3d fluid-structure interaction. *International Journal for Numerical Methods in Fluids* **56**, 2151–2177.

Guilkey, JE, Harman, TB, and Banerjee, B (2007). An Eulerian-Lagrangian approach for simulating explosions of energetic devices. *Computers and Structures* **85**, 660–674.

Guilkey, JE and Weiss, JA (2003). Implicit time integration for the material point method: Quantitative and algoritmic comparisons with the finite element method. *International Journal for Numerical Methods in Engineering* **57**, 1323–1338.

Guo, Y and Nairn, JA (2004, sep). Calculation of J-integral and stres intensity factors using the material point method. *Computer Modeling in Engineering and Sciences* **6**(3), 295–308.

Guo, Z and Yang, W (2006). MPM/MD handshaking method for multiscale simulation and its application to high energy cluster impacts. *International Journal of Mechanical Sciences* **48**, 145–159.

Guthrie, RH, Evans, SG, Catane, SG, and Zarco MAH, RM, Saturay Jr. (2009). The 17 February 2006 rock slide-debris avalanche at Guinsaugon Philippines: a synthesis. *Bulletin of Engineering Geology and the Environment* **68**, 201–213.

Ham, G, Rohn, J, Meier, T, and Czurda, K (2009). Finite element simulation of a slow moving natural slope in the upper-austrain alps using a visco-hypoplastic constitutive model. *Geomorphology* **103**, 136–142.

Han, J, Chai, JC, Leshchinsky, D, and Shen, SL (2004). Evaluation of deep-seated slope stability embankments over deep mixed foundations. In *Geosupport Conference on Innovation and Cooperation in the Geo-Industry, JAN 29-31, 2004 Orlando, FL*, pp. 945–954.

Harlow, FH (1964). The particle–in–cell computing method for fluid dynamics. *Methods for Conputational Physics* **3**, 319–343.

Hasegawa, S, Dahal, RK, Yamanaka, M, Bhandary, NP, Yatabe, R, and Inagaki, H (2009). Causes of large-scale landslides in Lesser Himalaya of central Nepal. *Enviromental Geology* **57**, 1423–1434.

Higdon, RL (1990). Radiation boudary conditions for elastic wave propagation. *SIAM Journal of Numerical Analysis* **27**, 831–870.

Hryb, D, Cardozo, M, and Goldsmith, M (2009). Particle transport in turbulent flow using both Lagrangian and Eulerian formulations. *International Communications in Heat and Mass Transfer*, 451–457.

Hu, W and Chen, Z (2003). A multi-mesh MPM for simulation the meshing process of spurning gears. *Computers and Structures* **81**, 1991–2002.

Hu, W and Chen, Z (2006). Model-based simulation of the synergistic effects of blast and fragmentation on a concrete wall using the MPM. *International Journal of Impact Engineering* **32**, 2066–2096.

Huang, C-C, Ju, Y-J, Hwu, L-K, and Lee, J-L (2009). Internal soil moisture and piezometric responce to rainfall-induced shallow slope failures. *Journal of Hydrology* **370**, 39–51.

Huat, BBK, Ali, FH, and Rajoo, RSK (2006). Stability analysis and stability chart for unsaturated residual soil slope. *American Journal of Enviromental Sciences* **2**, 154–160.

Jakob, M and Lanbert, S (2009). Climate change efects on landslides along the southwest coast of British Colombia. *Geomorphology* **107**, 275–284.

Janbu, N (1954). Application of composite slipe surface for stability analysis. In *Proceedings of European Conference on Stability of Earth Slopes, Stockholm*, pp. 43–49.

Johnson, GC and Bamman, DJ (1984). A discussion of stress rates in finite deformation problems. *International Journal of Solids and Structures* **20**, 725–737.

Kequiang, H, Guangming, Y, and Xiangran, L (2009). The regional distribution of landslides and their effects on the enviroments in the Three Gorges Reservoir Region, China. *Enviromental Geology* **57**, 1925–1931.

Krenk, S and Kirkegaard, PH (2001). Local tensor radiation conditions for elastic waves. *Journal of Sound and Vibration* **247**, 875–896.

Lacerda, WA (2007). Landslide initiation in saprolite and colluvium in southern Brazil: Field and laboratory observations. *Geomorphology* **87**, 104–119.

Li, G and Belytsko, T (2001). Element-free Galerkin method for contact problems in metal forming analysis. *Engineering Computations* **18**, 62–78.

Li, S and Liu, WK (2002). Meshfree and particle methods and their applications. *Applied Mechanics Review* **55**, 1–34.

Liszka, TJ, Duarte, CAM, and Tworzydlo, WW (1996). *hp*-meshless cloud method. *Computer Methods in Applied Mechanics and Engineering* **139**, 263–288.

Liu, GR (2002). *Smoothed Particle Hydrodynamics: A meshfree particle method*. World Scientific Publishing Company.

Liu, J, Chen, H, Ewing, R, and Qin, G (2007). An efficient algorithm for characteristic tracking on two-dimensional triangular meshes. *Computing* **80**, 121–136.

Love, E and Sulsky, DL (2006a). An energy-consistent material-point method for dynamic finite deformation plasticity. *International Journal for Numerical Methods in Engineering* **65**, 1608–1638.

Love, E and Sulsky, DL (2006b). An unconditionally stable, energy-momemtum consistent implementation of the material point method. *Computer Methods in Applied Mechanics and Engineering* **195**, 3903–3925.

Ma, J, Hongbing, L, and Komanduri, R (2006). Strucured mesh refinement in generalized interpolation material point method (gimp), method for simulation of dynamic problems. *Computer Modelling in Engineering and Sciences* **12**(3), 213–227.

Ma, J, Lu, H, Wang, B, Roy, S, Hornung, R, Wissing, A, and Komanduri, R (2005). Multiscale simulations using generalized interpolation material point method (gimp) method and samrai parallel processing. *Computer Modelling in Engineering and Sciences*, 135–152.

Ma, S, Zhang, X, and Qiu, XM (2009). Comparison study mpm and sph in modeling hypervelocity impact problems. *International Journal of Impact Engineering* **36**, 272–282.

Michalowski, RL (2002). Stability charts for uniform slopes. *Journal of Geotechnical and Geoenviromental Engineering* **128**, 351–355.

Monaghan, JJ (2005). Smoothed particle hydrodynamics. *Reports on Progress in Physics* **68**, 1703–1759.

Nairn, JA (2003). Material point method calculations with explicit cracks. *Computer Modeling in Engineering and Sciences* **4**, 649–663.

Õnate, E, Idelsohn, S, Zienkiewicz, OC, Taylor, RL, and Sacco, C (1996). A stabilized finite point method for analysis of fluid mechanics problems. *Computer Methods in Applied Mechanics and Engineering* **139**, 315–346.

Nguyen, VP, Rabczuk, T, Bordas, S, and Duflor, M (2008). Meshless methods: A review and computer implementation aspects. *Mathematics and Computers in Simulation* **79**, 763–813.

Pedersen, SAS (2006). Strukturer og dynamisk udvikling af Rubjerg Knude glacialtektoniske kompleks, Vendsyssel, Danmark. Technical report, Danmarks og Grønlands Geologiske Undersøgelse.

Picarelli, L, Olivares, L, and Avolio, B (2008). Zoning for flowslide and debris flow in pyroclastic soils of Campania region based on "infinite slope" analysis. *Engineering Geology* **102**, 132–148.

Rycroft, CH, Kanrin, K, and Bazant, MZ (2009). Assesing the continuum postulates in simulations of granular flow. *Journal of Mechanics and Physics of Solids* **57**, 828–839.

Rzadkiewicz, SA, Mariotti, C, and Heinrich, P (1997). Numerical simulation of submarine landslides and their hydraulic effects. *Journal of Waterway Port Coastal and Ocean Engineering* **123**(149–157).

Sandhu, RS and Singh, J (1978). Reduced integration for improved accuracy of finite element approcimations. *Computer Methods in Applied Mechanics and Engineering* **14**, 23–37.

Savage, SB (1984). The mechanics of rapid granular flows. *Advances in Applied Mechanics* **24**, 289–366.

Schreyer, HL, Sulsky, DL, and Zhou, SJ (2002). Modeling delamination as a strong discontinuity with the material point method. *Computer Methods in Applied Mechanics and Engineering* **191**(23-24), 2483–2507.

Shen, LM and Chen, Z (2005). A silent boundary scheme with the material point method for dynamic analyses. *Computer Modeling in Engineering and Sciences* **7**, 305–320.

Shen, YL, Li, Q, Sulsky, D, and Schreyer, HL (2000). Localization of plastic deformation along grain boundaries in a hardening material. *International Journal of Mechanical Sciences* **42**, 2167–2189.

Skov og Naturstyrelsen (2008). Jordskred ved Maarup Kirke. Webpage, information retrieved Jan 3th, 2009. www.skovognatur.dk.

Steffen, M, Kirby, RM, and Berzins, M (2008). Analysis and reduction of quadrature errors in the material point method (MPM). *International Journal for Numerical Methods in Engineering* **76**, 922–948.

Steffen, M, Wallstedt, PC, Guilkey, JE, Kirby, RM, and Berzins, M (2008). Examination and analysis of implementation choices within the material point method (MPM). *Computer Modelling in Engineering and Sciences* **31**, 107–127.

Stoker, C (1999). *Developments of the Arbitrary Lagrangian-Eulerian Method in non-linear Solid Mechanics – Applications to Forming Processes*. Ph. D. thesis, Universiteit Twente.

Sulsky, D, Chen, Z, and Schreyer, HL (1994). A particle method for history-dependent materials. *Computer Methods in Applied Mechanics and Engineering* **118**, 179–196.

Sulsky, D and Kaul, A (2004). Implicit dynamics in the material-point method. *Computer Methods in Mechanics and Engineering* **193**(12–14), 1137–1170.

Sulsky, D and Schreyer, HL (1996). Axisymmetric form of the material point method with applications to upsetting and Taylor impact problems. *Computer Methods in Applied Mechanics and Engineering* **139**, 409–429.

Sulsky, D and Schreyer, H (2004). MPM simulation of dynamic material failure with a decohesion constitutive model. *European Journal of Mechanics and Solids* **23**, 423–445.

Sulsky, D, Zhou, SJ, and Schreyer, HL (1995). Application of a particle-in-cell method to solid mechanics. *Computer Physics Communications* **87**, 236–252.

Takahashi, T (2007). *Debris Flow - Mechanics, Prediction and Countermeasures*. Taylor and Francis.

Tan, HL and Nairn, JA (2002). Hierarchical, adaptive, material point method for dynamic release rate calculations. *Computer Methods in Applied Mechanics and Engineering* **191**(19-20), 2095–2109.

Taylor, DW (1948). *Fundamental soil mechanics*. John Wiley and Sons, New York.

Timoshenko, SP and Goodier, JN (1970). *Theory of elasticity* (3rd ed.). McGraw-Hill.

Trobec, R, Šterk, M, and Robič, B (2009). Computational complexity and parallelization of the meshless local Petrov-Galerkin method. *Computers and Structures* **87**, 81–90.

Tsuchiya, S, Sasahara, K, Shuin, S, and Ozono, S (2009). The large-scale landslide in South Sulawesi, Indonesia. *Landslides* **6**, 83–88.

Tv2Nord (2008). Kæmpeskred tæt på Rubjerg Knude. Webpage, information retrieved Dec 29th, 2008. www.tv2nord.dk.

United States Geological Survey (2004). Landslide types and processes. Fact sheet 2005-3072. Technical report.

Wallstedt, PC and Guilkey, JE (2007). Improved velocity projection for the material point method. *Computer Modelling in Engineering and Sciences* **3**, 223–232.

Wallstedt, PC and Guilkey, JE (2008). An evaluation of explicit time integration schemes for use with the generalized interpolation material point method. *Journal of Computational Physics* **227**, 9628–9642.

Wang, B, Paudel, B, and Li, H (2009). Retrogression charecteristics of landslides in fine-grained permafrost soils, Mackenzie valley, Canada. *Landslides* **6**, 121–127.

Wieckowski, Z (2004). The material point method in large strain engineering problems. *Computer Methods in Applied Mechanics and Engineering* **193**(39–41), 4417–4438.

Wieckowski, Z, Youn, SK, and Yeon, JH (1999). A particle-in-cell solution to the silo discharging problem. *International Journal for Numerical Methods in Engineering* **45**, 1203–1225.

York, AR, Sulsky, D, and Schreyer, HL (1999). The material point method for simulation of thin membranes. *International Journal for Numerical Methods in Engineering* **44**, 1429–1456.

York, AR, Sulsky, D, and Schreyer, HL (2000). Fluid-membrane interaction based on the material point method. *International Journal for Numerical methods in Engineering* **48**, 901–924.

Zhang, D, Wang, G, Luo, C, Chen, J, and Zhou, Y (2009). A rapid loess flowslide triggered by irrigation in China. *Landslides* **6**, 55–60.

Zhang, HW, Wang, KP, and Chen, Z (2009). Material point method for dynamic analysis of saturated porous media under external contact/impact of solid bodies. *Computer Methods in Applied Mechanical Engineering* **198**, 1457–1472.

Zhang, Z, KY, Szt, and Ma, S (2006). An explicit material point finite element method for hyper-velocity impact. *International Journal for Numerical Methods in Engineering* **66**, 689–706.

Zhou, SJ, Stormont, J, and Chen, Z (1999). Simulation of geomembrane response to settlement in landfills by using the material point method. *International Journal for Numerical and Analtical Methods in Geomechanics* **23**, 1977–1994.

Zienkiewicz, OHC, Chan, AHC, Pastor, M, Schrefler, BA, and Shiomi, T (1999). *Computational Geomechanics - with Special Reference to Earthquake Engineering*. Wiley.

Zienkiewicz, OC and Taylor, RL (2005). *The Finite Element Method for Solids and Structural Mechanics* (5 ed.). Elsevier.

Zienkiewicz, OC, Taylor, RL, and Zhu, JZ (2005). *The Finite Element Method: Its basis and Fundamentals* (5 ed.). Elsevier.

# APPENDIX A
# Paper I: Analysis of Spatial Interpolation in the Material-Point Method

## Analysis of Spatial Interpolation in the Material-Point Method

S. Andersen and L. Andersen

*Department of Civil Engineering, Aalborg University, Aalborg, Denmark*

*Paper published in Computers and Structures, April, 2010*

**Abstract:** This paper analyses different types of spatial interpolation for the material-point method. The interpolations include quadratic elements and cubic splines in addition to the standard linear shape functions usually applied. For the small-strain problem of a vibrating bar, the best results are obtained using quadratic elements. It is shown that for more complex problems, the use of partially negative shape functions is inconsistent with the material-point method in its current form, necessitating other types of interpolation such as cubic splines in order to obtain smoother representations of field quantities. The properties of different interpolation functions are analysed using numerical examples, including the classical cantilevered beam problem.

**Reference:**

Andersen, S and Andersen, L 2010,
Analysis of Spatial Interpolation in the Material-Point Method
Computers and Structures, Vol. 88, Nr. 7-8, 2010, s. 506-518.

**DOI:** 10.1016/j.compstruc.2010.01.004

# Appendix B
# Paper II: Modelling of Landslides with the Material-Point Method

*Paper published in Computational Geosciences, January, 2010*

## Modelling of Landslides with the Material-Point Method

S. Andersen , L. Andersen

*Department of Civil Engineering, Aalborg University, Aalborg, Denmark*

**Abstract:** A numerical model for studying the dynamic evolution of landslides is presented. The numerical model is based on the Generalized Interpolation Material Point Method. A simplified slope with a house placed on top is analysed. An elasto-plastic material model based on the Mohr-Coulomb yield criterion is employed for the soil. The slide is triggered for the initially stable slope by removing the cohesion of the soil and the slide is followed from the triggering until a state of equilibrium is again reached. Parameter studies, in which the angle of internal friction of the soil and the degree of discretization is varied, are presented.

**Reference:**

Andersen, S and Andersen, 2010,
Modelling of Landslides with the Material-point Method
Computational Geosciences, vol 14, nr. 1, s. 137–147.

**DOI:** 10.1007/s10596-009-9137-y

# APPENDIX C
# Paper III: Material-Point Analysis of Collapsing Slopes

*This paper was presented at the First International Symposium on Computational Geomechanics (COMGEO I), Juan-les-Pins, France, 29 April – 1 May, 2009.*

# Material-Point Analysis of Collapsing Slopes

S. Andersen , L. Andersen

*Department of Civil Engineering, Aalborg University, Aalborg, Denmark*

**Abstract:** The collapse of slopes leading to landslides is a severe natural hazard taking many lives every year. Besides understanding when slopes becomes unstable, the understanding of the behaviour of the collapsing slope is of great interest in order to estimate the potential risk. The idea in the present paper is to examine the dynamic evolution of slides in unstable slopes by means of numerical simulations.

The modelling is performed with the aid of our recently developed material-point method for large strain problems. The model is an extension of the Material-Point Method (MPM) (Sulsky et al. 1994), (Sulsky et al. 1995) and the generalized interpolation material point method (Bardenhagen and Kober 2004). The soil is described using a Lagrangian description in which the soil is divided into a number of discrete material points at which the mass, stresses, strains and other properties are evaluated. This allows for incorporation of complex constitutive material models as history dependent variables are tracked trough the simulation. The physical properties are mapped to a Eulerian grid where the kinematic equations are solved. The combination of the Lagrangian and the Eulerian material description allows the simultaneous modelling of complex material behaviour and large displacements. Further, a friction condition is introduced in order to introduce frictional contact between different particles.

The presented test case is a recent landslide in Denmark, near Rubjerg Knude, on steep slopes near the beach. Our data on the geometry is based on surveying after the landslide. This is compared with GIS data from 2007. The slope before the slide is discretized using our numerical method and different algorithms for triggering the slide is tested. Despite a large uncertainty regarding the properties and variation of the soil layers before and after the slide, the presented numerical model provides insight into the physics while the slide is taking place.

## C.1 Introduction

This article present a novel computational technique for modelling of dynamic problems involving large strains and complex material behaviour. The presented numerical model is an extension of the material point method (Sulsky et al. 1994) and the generalized interpolation material point method (Bardenhagen and Kober 2004). In the material point method the physical domain is discretized into a number of points where material properties and state variables are prescribed. The interaction between the different points is obtained by mapping to a grid when solving the governing equations. Further, the grid is used to obtain strain increments for the material points. As the material points carry all the state variables, an undeformed mesh is employed at all time steps. Also, convection issues associated with a Eulerian formulation are avoided.

In the original MPM formulation, (Sulsky et al. 1994), mapping between the material points and the grid is performed by evaluating the nodal shape-functions associated with the grid at the location of the material points. Representing each material point as a volume, and integrating over the volume when mapping between material points the grid is shown by (Bardenhagen et al. 2001) to provide more accurate results. The method presented here provides a numerical means of integration when the material points are subject to significant strains and rotations. This is done by associating a deformation gradient tensor with each material point. The deformed volume of the material point is found using the deformation gradient tensor. The integration of the material point volume on the grid is then performed using Gauss quadrature.

In order to understand the interaction between different physical bodies, a frictional contact algorithm is presented. This allow for modelling different continuum materials. The governing equations are solved separately for each particular continuum. The interaction between different materials is governed by a frictional contact law. The employed frictional contact law avoids interpenetration of two materials and allows materials to slide relatively to each other. The evaluation of the frictional contact forces is performed using the grid. In the algorithms presented in (York et al. 1999), (Bardenhagen et al. 2000a) and (Bardenhagen et al. 2001) the normal vectors for each continuum are found independently, by employing the grid-node density field obtained the particular continuum. Due to poor discretization, the normal vectors of two adjacent materials may not point in straightly opposite directions and therefore this approach may fail. In particular, sliding at an interface can be hindered by an erroneous on parts of the surface of a small body interacting with a body much greater extent. In order to avoid these issues, a change of the original algorithm is presented that allows for interaction between continuum materials with an arbitrary interface. This is done by defining a hierarchy of the continuum materials, and letting the normal vector for the master material define the direction of the common interface.

The presented method is employed to analyse a recent landslide at Rubjerg Knude in northern Denmark. The soil in the landslide at Rubjerg Knude consist of clay and sand. The layers interfaces are inlcined at high angles due to ice techtonic dislocation during last age. Hence, the slide has likely occured due to the clay becoming heavy and caused it to slide along the interface with sand.

The theory behind the numerical model is presented in Section C.2. Section C.3 presents the numerical study of the slide while the conclusions are presented in Section C.4.

## C.2 Theory

### C.2.1 Governing equations

A continuum problem subject to initial and boundary conditions is considered. The governing equation for the momentum is given by

$$\rho \frac{dv_\alpha}{dt} = \frac{\partial \sigma_{\alpha\beta}}{\partial x_\beta} + \rho b_\alpha, \tag{C.1}$$

where $\sigma_{\alpha\beta}$ is the Cauchy stress tensor and $b_\alpha$ is the specific body force. The index $\alpha$ ranges over 1 and 2 in the case of plane strain considered in the presented analysis.

### C.2.2 Weak formulation

A weak form of Eq. (C.1) is obtained by multiplying the balance of momentum by an arbitrary test function $w_\alpha$ and integrating over the initial volume. Applying integration by parts and employing the Green theorem, the weak form is given by

$$\int_\Omega \rho w_\alpha \frac{dv_\alpha}{dt} dV = \int_{\Gamma_\tau} w_\alpha \tau_\alpha d\Gamma - \int_\Omega \frac{\partial w_\alpha}{\partial x_\beta} \sigma_{\alpha\beta} dV + \int_\Omega \rho w_\alpha b_\alpha dV, \tag{C.2}$$

where $\tau_\alpha$ is the surface traction on part of the boundary, $\Gamma_\tau$, where the surface tractions are prescribed, and $\Omega$ the physical domain.

### C.2.3 Generalized interpolation material-point discretization

In order to discretize Eq. (C.2), the domain is represented by a set of $n_p$ smaller domains. A material point is associated with the centre of each subdomain, defined by the coordinates, $x^p_\alpha$, $p = 1, ..n_p$. The velocity and stress associated with a material point are defined as volume-weighted quantities, i.e.

$$v^p_\alpha = \frac{1}{V_p} \int_{\Omega_p} v_\alpha(x_\beta) dV, \tag{C.3}$$

where $V_p$ is the volume of the material point region in the current state and

$$\sigma^p_{\alpha\beta} = \frac{1}{V_p} \int_{\Omega_p} \sigma_{\alpha\beta}(x_\gamma) dV. \tag{C.4}$$

Similarly, external body forces are defined by.

$$b^p_\alpha = \frac{1}{V_p} \int_{\Omega_p} b_\alpha(x_\beta) dV. \tag{C.5}$$

Finally a deformation gradient is associated with each material point in the current state as

$$F^p_{\alpha\beta} = \frac{\partial x_\alpha}{\partial x^0_\beta}_p \Bigg|_{x=x_p} = \frac{1}{V_p} \int_{\Omega^p} F_{\alpha\beta}(x_\gamma) dV, \tag{C.6}$$

where $x_0$ are the initial coordinates. In order to obtain a discrete spatial representation, particle characteristic functions, $\chi_p$, associated with the material points are defined (Bardenhagen and Kober 2004). The particle characteristic functions are normalized with respect to the initial volume, i.e.

$$\int_{\Omega^p_0} \chi_p(x_\alpha, t) d\Omega = V^0_p, \tag{C.7}$$

where $V^0_p$ is the volume associated with the point in the initial state.

Field quantities are represented as sums over the material points, i.e.

$$f(x_\alpha) = \sum_p f_p \chi_p(x_\alpha), \tag{C.8}$$

For instance the first term in the balance of momentum is represented by

$$\rho\frac{dv_\alpha}{dt} \cong \sum_p \rho^p \frac{dv_\alpha^p}{dt}\chi_p = \sum_p \frac{m_p}{V_p}\frac{dv_\alpha^p}{dt}\chi_p = \sum_p \frac{\dot{\pi}^p}{V_p}\chi_p, \tag{C.9}$$

where the momentum rate of change has been introduced as $\dot{\pi}^p = m_p dv_\alpha^p/dt$. In our implementation we use a constant particle characteristic function. Hence, stresses, densities etc. are considered constants within the volume associated with each material point.

Using the material-points representation in the balance of momentum yields

$$\sum_p \frac{\dot{\pi}_\alpha^p}{V_p}\int_{\Omega_p \bigcup \Omega} w_\alpha \chi_p dV = \int_{\Gamma_\tau} w_\alpha \tau_\alpha dS - \sum_p \sigma_{\alpha\beta}^p \int_{\Omega_p \bigcup \Omega} \frac{\partial w_\alpha}{\partial x_\beta}\chi_p dV$$

$$+\sum_p \frac{m^p b_\alpha^p}{V_p}\int_{\Omega_p \bigcup \Omega} w_\alpha \chi_p dV. \tag{C.10}$$

The term on the left hand side represents the rate of change of momentum. On the right hand side, the first term represents the surface tractions, the second term represents internal forces due to stress gradients while the last term represents external body forces. Further it is noted that the physical quantities are evaluated at each material point.

A background grid is introduced and the test function $w_\alpha(x_\beta, t)$ is discretized in to its values $w_\alpha^i$, $i = 1, 2..n_n$ at $n_n$ nodes. Within each cell of the grid, interoplation of the test function and its gradient is carried out by means of shape functions $N_i(x_\beta)$ associated with the nodes, i.e

$$w_\alpha(x_\beta) \cong \sum_i w_\alpha^i N_i(x_\beta), \quad \frac{\partial w_\alpha(x_\gamma)}{\partial x_\beta} \cong \sum_i w_\alpha^i \frac{\partial N_i(x_\gamma)}{\partial x_\beta}, \tag{C.11}$$

where $\sum_i$ denotes the sum over the grid nodes and $N_i$ is the nodal shape function associated with node $i$.

Employing Eq. (C.11), the balance of momentum can be written.

$$\sum_i \sum_p w_\alpha^i \dot{\pi}_\alpha^p \frac{1}{V_p}\int_{\Omega_p \bigcup \Omega} N_i \chi_p dV = \sum_i w_\alpha^i \int_{\Gamma_\tau} N_i \tau_\alpha dS$$

$$-\sum_i \sum_p w_\alpha^i \sigma_{\alpha\beta}^p \int_{\Omega_p \bigcup \Omega} \frac{\partial N_i}{\partial x_\beta}\chi_p dV + \sum_i \sum_p w_\alpha^i m^p b_\alpha^p \frac{1}{V_p}\int_{\Omega_p \bigcup \Omega} N_i \chi_p dV. \tag{C.12}$$

Now the weighting and the gradient-weighting functions are introduced as

$$\bar{N}_{ip} = \frac{1}{V_p}\int_{\Omega_p \bigcup \Omega} N_i \chi_p dV, \quad \frac{\partial \bar{N}_{ip}}{\partial x_\beta} = \frac{1}{V_p}\int_{\Omega_p \bigcup \Omega} \frac{\partial N_i}{\partial x_\beta}\chi_p dV. \tag{C.13}$$

Utilising that the test functions $w_\alpha^i$ are arbitrary, the system of equations need to be satisfied at all grid nodes. Employing Eq. (C.13) in Eq. (C.12) yields

$$\sum_p \dot{\pi}_\alpha^p \bar{N}_{ip} = \int_{\partial\Omega_\tau^0} N_i \tau_\alpha dS - \sum_p \sigma_{\alpha\beta}^p V_p \frac{\partial \bar{N}_{ip}}{\partial x_\beta} + \sum_p m^p b_\alpha^p \bar{N}_{ip}. \tag{C.14}$$

Rewriting the balance of momentum yields

$$\dot{\pi}_\alpha^i = f_\alpha^{i,int} + f_\alpha^{i,ext}, \tag{C.15}$$

where

$$\dot{\pi}_\alpha^i = \sum_p \dot{\pi}_\alpha^p \bar{N}_{ip}, \quad f_\alpha^{i,int} = -\sum_p \sigma_{\alpha\beta}^p V_p \frac{\partial \bar{N}_{ip}}{\partial x_\beta}, \quad f_\alpha^{i,ext} = \int_{\Gamma_\tau} N_i \tau_\alpha dS + \sum_p m^p b_\alpha^p \bar{N}_{ip} \tag{C.16}$$

is the rate of change of the nodal momentum, the internal force and the external force, respectively. As the mass is tracked through the material points, the conservation of mass is automatically satisfied.

### C.2.4 Numerical integration

The above derivation yields final equations identical to the GIMP formulation presented by Bardenhagen (2004). For landslides involving rotations and deformations the analytically evaluated GIMP weighting functions in (Bardenhagen and Kober 2004) can no longer be applied to represent the physical domain of the material points. Hence, a scheme for numerically evaluating the GIMP functions is presented. Each region associated with material point is assigned a number of Gauss points. Rewriting the integral part of the weighting functions and the gradient weighting functions as sums over the Gauss points yields

$$\bar{N}_{ip} = \frac{1}{V_p} \sum_{GP} \chi_p(x_\alpha^{GP}) N_i(x_\alpha^{GP}) \phi_{GP}, \quad \frac{\partial \bar{N}_{ip}}{\partial x_\beta} = \frac{1}{V_p} \sum_{GP} \chi_p(x_\alpha^{GP}) \left. \frac{\partial \bar{N}_{ip}(x_\alpha)}{\partial x_\beta} \right|_{x_\alpha = x_\alpha^{GP}} \phi_{GP}, \tag{C.17}$$

where $\phi_{GP}$ is the weight for the Gauss point, normalized to provide $\sum_{GP} \phi_{GP} = V_p$. Integrating numerically over the shared domain is consistent as either $N_i(x_\alpha^{GP}) = 0$ or $\chi_p(x_\alpha^{GP}) = 0$ outside the shared domain. The equations can be further simplified as

$$\bar{N}_{ip} = \sum_{GP} \chi_p(x_\alpha^{GP}) N_i(x_\alpha^{GP}) \bar{\phi}_{GP}, \quad \frac{\partial \bar{N}_{ip}}{\partial x_\beta} = \sum_{GP} \chi_p(x_\alpha^{GP}) \left. \frac{\partial \bar{N}_{ip}(x_\alpha)}{\partial x_\beta} \right|_{x_\alpha = x_\alpha^{GP}} \bar{\phi}_{GP}, \tag{C.18}$$

where $\sum_{GP} \bar{\phi}_{GP} = 1$. If a single Gauss point, located at the material point, is employed, the weighting function becomes simply the nodal shape function and the original MPM formulation given by Sulsky et al. (1995) is retrieved.

Considering a material point initially located at $x_\alpha^{p,0}$, the coordinate for a Gauss point can be written as

$$x_\alpha^{GP,0} = x_\alpha^{p,0} + dx_\alpha^0, \tag{C.19}$$

where $x_\alpha^{GP,0}$ is the location of the Gauss point in the initial configuration and $dx_\alpha^0$ is the line segment between the material point and the Gauss point in the initial configuration. At an arbitrary time the location of the Gauss point is given as

$$x_\alpha^{GP} = x_\alpha^p + dx_\alpha. \tag{C.20}$$

Using the deformation gradient, defined at the material point, the line segment can be calculated by

$$dx_\alpha = F_{\alpha\beta} dx^0_\beta, \tag{C.21}$$

where $dx_\beta$ is the deformed line segment and $F_{\alpha\beta}$ is the deformation-gradient tensor defined locally by

$$F_{\alpha\beta} = \frac{\partial x_\alpha}{\partial \xi_\gamma} \frac{\partial \xi_\gamma}{\partial \xi^0_\delta} \frac{\partial \xi^0_\delta}{\partial x^0_\beta}. \tag{C.22}$$

In the presented examples, the initial local axes are chosen along the global coordinate system. Hence, in this case

$$F_{\alpha\beta} = \frac{\partial \xi_\alpha}{\partial \xi^0_\beta}. \tag{C.23}$$

The idea of utilizing a non-linear strain measure within the MPM is introduced by Guilkey and Weiss (2003) who introduce a weak form of the balance of momentum based on the deformation gradient and the second Piola-Kirchhoff stress tensor.

### C.2.5 Kinematics

The location of the Gauss points is specified through the deformation-gradient tensor which needs to be tracked through the simulation for each material point. In the initial configuration, the deformation gradient tensor is presumed known. Typically, an undeformed material state will be prescribed, i.e. $F^0_{\alpha\beta} = \delta_{\alpha\beta}$, where $\delta_{\alpha\beta}$ is the Kronecker delta. An explicit forward difference updating scheme for updating the deformation gradient is employed,

$$F^{k+1}_{\alpha\beta} = \Delta F^{k+1}_{\alpha\beta} F^k_{\alpha\beta}. \tag{C.24}$$

Expressing the time derivative of the deformation gradient as $\partial F_{\alpha\beta}/\partial t = \partial v^k_\alpha / \partial x^0_\beta$, $\Delta F^k_{\alpha\beta}$ can be expressed as

$$\Delta F^{k+1}_{\alpha\beta} = \delta_{\alpha\beta} + \Delta t \frac{\partial v^k_\alpha}{\partial x_\beta}. \tag{C.25}$$

Using the nodal shape functions, the change in deformation gradient at an arbitrary point $x_\gamma$ can be evaluated as

$$\Delta F^{k+1}_{\alpha\beta}(x_\gamma) = \delta_{\alpha\beta} + \Delta t \sum_i v^{i,k}_\alpha \frac{\partial N_i(x_\gamma)}{\partial x_\beta}. \tag{C.26}$$

By use of the particle characteristic function the increment of deformation gradient can be formulated as

$$\Delta F^{p,k+1}_{\alpha\beta} = \delta_{\alpha\beta} + \Delta t \sum_i v^{i,k}_\alpha \frac{\partial \bar{N}_{ip}}{\partial x_\beta}. \tag{C.27}$$

This way of integrating the deformation gradient, using the grid velocities, is also employed by Love and Sulsky (2006b).

The stress is integrated using an updated Lagrangian scheme. At the beginning of the time step, a reference state is defined by $S^k_{\alpha\beta} := \sigma^k_{\alpha\beta}$. For small strain increments, the approximation $\dot{\varepsilon}_{\alpha\beta} = \dot{E}_{\alpha\beta}$ is valid, where $\dot{E}_{\alpha\beta}$ is the Green strain rate and $\dot{\varepsilon}_{\alpha\beta}$ is the linear strain rate,

$$\dot{\varepsilon}_{\alpha\beta} = \frac{1}{2}\left(\frac{\partial v_\alpha}{\partial x_\beta} + \frac{\partial v_\beta}{\partial x_\alpha}\right). \tag{C.28}$$

Thus the rate of change of the second Piola Kirchhoff stress tensor is given by

$$\dot{S}_{\alpha\beta} = C_{\alpha\beta\gamma\delta}\dot{\varepsilon}_{\gamma\delta}, \tag{C.29}$$

where $C_{\alpha\beta\gamma\delta}$ yields the constitutive behaviour of an observed material point at the current material state.

Using a forward difference scheme the Piola-Kirchhoff stress at the end of the time step is approximated by

$$S^{k+1}_{\alpha\beta} = \sigma^k_{\alpha\beta} + \Delta t\dot{S}_{\alpha\beta} \tag{C.30}$$

The local deformation occurring during the time step is given by $\Delta F^k_{\alpha\beta}$, hence the rate-objective Cauchy-stress at end of the time-step is given by

$$\sigma^{k+1}_{\alpha\beta} = \frac{1}{\Delta J}\Delta F^{k+1}_{\alpha\gamma} S^{k+1}_{\gamma\delta}\Delta F^{k+1}_{\delta\beta}, \tag{C.31}$$

where $\Delta J = \det(\Delta F^{k+1}_{\alpha\beta})$

### C.2.6 Implementation

Above the governing equations for a large strain GIMP method using numerical integration is given. The basic idea is to solve the balance of momentum on the grid and then use the information to update the state variables at the material points. The mass and momentum at a grid node $i$ are found by

$$m^k_i = \sum_p m^k_p \bar{N}_{ip} \quad \text{and} \quad \pi^{i,k}_\alpha = \sum_p \pi^{p,k}_\alpha \bar{N}_{ip}, \tag{C.32}$$

respectively. Using a linear extrapolation of Eq. (C.15), the nodal momentum at the end of the time step is found by

$$\pi^{i,k+1}_\alpha = \pi^{i,k}_\alpha + \Delta t(f^{i,int,k}_\alpha + f^{i,ext,k}_\alpha). \tag{C.33}$$

The position and the velocity update for the material points are then given by

$$x^{p,k+1}_\alpha = x^{p,k}_\alpha + \frac{\Delta t}{m_p}\sum_i \pi^{i,k+1}_\alpha \bar{N}_{ip} \tag{C.34}$$

and

$$v^{p,k+1}_\alpha = v^{p,k}_\alpha + \frac{\Delta t}{m_p}\sum_i (f^{i,int,k}_\alpha + f^{i,ext,k}_\alpha)\bar{N}_{ip}. \tag{C.35}$$

The algorithm can be summarised as:

**1** Initialisation of material properties, including the deformation gradient at the material points at time $t^k = 0$

**2** At each time step:

- A background computational grid is generated
- The coordinates for the Gauss-points are found by Eq. (C.20)
- The weighting and the gradient weighting functions are determined using numerical integration by Eq. (C.18)
- Stress and strain increments are found and stresses and strains are updated
- The objective Cauchy stress at the end of the time-step is found by Eq. (C.31)
- Internal and external forces are found by Eq. (C.16)
- The updated nodal momentum is determined using Eqs. (C.16) and (C.33)
- The position and the velocity of the material points are found by Eqs. (C.34) and (C.35)
- The deformation gradient increment for the material points are updated using Eq. (C.24) and the total deformation gradient is calculated.

Here an algorithm as simple as possible has been presented, hence, explicit forward difference schemes has employed for both updating deformation gradient, Eq. (C.27) , the stress, Eq. (C.30) and to update the velocity and position of the material points, (C.35) and (C.34). As the resulting equations are similar to the original MPM formulation, the difference being how to construct the weighting functions and how to integrate constitutive behaviour, implicit MPM schemes such as presented by Cummins and Brackbill (2002), Guilkey and Weiss (2003), and Sulsky and Kaul (2004) can also be implemented.

### C.2.7 Frictional contact algorithm

The algorithm above described is employed when the modelled material can be considered one single continuum. In (Sulsky et al. 1995) it shown that the algorithm can also model collision between colliding bodies, illustrated by the simple problem of collision of two elastic discs. This is due to the interaction between the two bodies when internal forces are calculated on the grid. However, in (York et al. 1999) modelling interaction between different bodies is shown to have shortcomings using a shared nodal field for the whole domain. If the contact between two particles is over a large area compared to the volume or the materials are soft the two interacting materials tend to stick together instead of separating after contact. The authors provides an algorithm that allow different bodies to only share grid-nodes when they are moving towards each other.

In the study of landslides it is essential to model friction in the interfaces between the sand and the clay. Further, the large strains observed in a landslide necessitates the ability to model material separation, i.e. when parts of the soil stop belonging to the continuum, and is able to move relative to the remaining soil. Hence, a frictional contact algorithm is introduced. The idea to model interaction between different materials using frictional contact laws was introduced in (Bardenhagen et al. 2000a), and an improved algorithm to determine contact was presented in (Bardenhagen et al. 2001). Here the domain of material points is subdivided into a number

of continuums ("grains" in the initial reference). Within each subdomain, the equations of a continuum are valid. The interpolations defined by Eq. (C.32) and Eq. (C.16) are performed for each continuum. Between adjacent continua, a frictional contact model is introduced. Using $v_\alpha^i = \pi_\alpha^i / m_i$, a center-of-mass velocity, $v_\alpha^{i,CM}$, at a grid node can be found by integrating over all material points. Similarly, a velocity of one continuum, $v_\alpha^{i,c}$, can be found, where index $c$ corresponds to the continuum material. Nodes representing interfaces are identified by

$$v_\alpha^{i,CM} - v_\alpha^{i,c} \neq 0. \tag{C.36}$$

For a node representing an interface, a normal surface traction, $\tau_n^{i,c}$, is introduced by $\tau_n^{i,c} = n_\alpha^{i,c} \sigma_{\alpha\beta}^{i,c} n_\beta^{i,c}$, where $n_\alpha^{i,c}$ is the outward unit normal of continuum $c$ evaluated at node $i$ and $\sigma_{\alpha\beta}^{i,c}$ is the Cauchy stress at the node found by mapping from the material points.

The contact forces are determined at the grid nodes. Direction-of-sliding forces and normal forces applied to the continuum at a grid node are determined based on unit outward normal vectors. An algorithm for determining these normal vectors based on the density fields is presented in (York et al. 1999). In order to model problems, in which three or more continua interact, a master–slave relationship is employed. The continua at a grid node are assigned numbers, where $c = 1$ corresponds to the master material. For material 1, the normal vector $n_\alpha^{i,1}$ is determined according to the original scheme proposed by (York et al. 1999). The normal vector for material 2 is prescribed as $n_\alpha^{i,2} = -n_\alpha^{i,1}$, i.e. orthogonal to the density field of material 1. The normal vector for material 3 is prescribed orthogonal to the combined density fields of materials 1 and 2. This can be generalized to handle any number of continua.

The normal surface traction is found as described in (Bardenhagen et al. 2001). Using the sign convention where compressive stress is negative, the frictional-contact algorithm is enforced at an interface node when $t_n^{i,c} < 0$.

When continua are not in contact, the governing equation (C.15) is solved for each body on its own. When the bodies are moving towards each other, frictional contact is enforced by changing the velocity fields of each continuum in order to prevent interpenetration and allow for incorporation of frictional forces. The details in the numerical implementation are found in (Bardenhagen et al. 2001). Basically the algorithm stops sliding when $t_t^{i,c} < \mu t_n^{i,c}$, where $t_t^{i,c}$ is the unit traction vector resolved in the tangential direction of sliding and $\mu$ is the coefficient of friction between the continuum and the other materials it is interacting with. When $t_t^{i,c} = \mu t_n^{i,c}$ sliding is allowed and the frictional force is determined by the coefficient of friction.

## C.3 Numerical study of a collapsing slope

### C.3.1 Presentation of the physical problem

The landslide near Rubjerg Knude occured in the night between Nov. 30th and Dec. 1st, 2008. Among other descriptive references, the slide is reported by (Tv2Nord 2008). On December 3rd., a survey of the slope was carried out in order to determine the geometry of the collapsed slope. The photos presented in Figs. C.1 and C.2 (left) are from the field trip. Smaller, but similar slides in the area is often reported, for instance in (Skov og Naturstyrelsen 2008).

The soil in the area consist of interchanging layers of clay and sand. A detailed geological study of the glacial tectonic complex, which the slope at Rubjerg Knude is a part of, is presented in (Pedersen 2006). The layers vary in a complex pattern due to events after the soil was deposited. Due to glacial tectonic events that occurred during last ice age, initially horizontal or

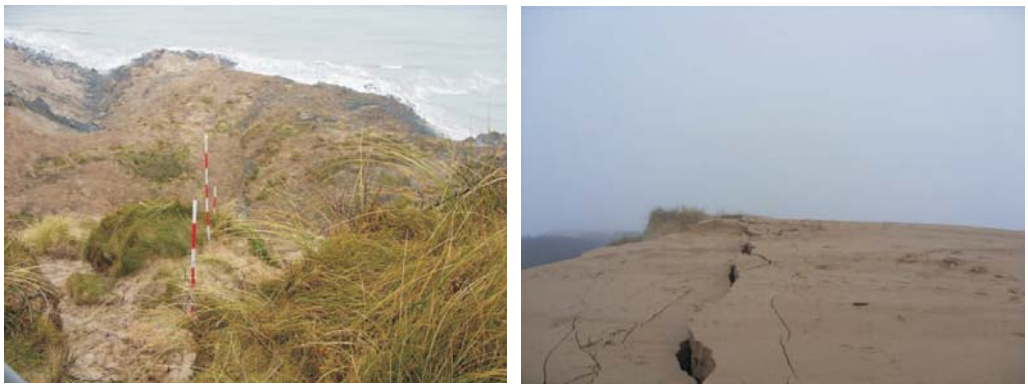

**Figure C.1** Left: After the landslide. This and the next photos were taken Dec. 3th, 2008. The poles in the picture are used as points in the surveying performed, in order to obtain the geometry of a typical cross-section after the slide. Right: Development of cracks in the sand material. Photo taken approximately 300 metres to the south of the slide.

almost horizontal layers between layers of clay and silt are now deposited at an angle of inclination as large as 60 degrees (Pedersen 2006). This has a significant impact on the slope stability, as landslides are often observed reported at the interfaces between different layers.

According to Bent Lykkegård, who is responsible for the maintenance of the area were the slides take place, the slide that occurred in the night between Nov. 30th and Dec. 1st, 200 is the largest in his 20 year period, (Tv2Nord 2008). On Nov. 27th, 2008 deep cracks were observed, but it was expected that it would take several years for the cracks to develop into a slide. A photo of typical cracks, probably due to sliding in an interface between clay and sand, about 300 metres to the south of the slide, is shown in Fig. C.1 (right).

Lykkegaard reports that the likely cause of the slide is heavy rainfall in the period up to the occurrence of the slide. This has likely has caused the clay material to become so heavy that started sliding down to the beach. Figure C.2 (left) shows the steepest part of the slope after the slide. After the field trip, the data obtained from the survey was compared to GIS data from 2007. Figure C.2 (right) show the cross sections before and after the slide. Some of the survey poles, utilized for obtaining the slope geometry after the slide, is visible in Fig. C.1 (left).

The relative location of the two cross sections, shown in Fig. C.2 (right), are subject to uncertainty. The location of a reference point on the slope after the slide was made a simple GPS-transmitter is with an uncertainty $\pm 12$m at the point of measuring, while the resolution of the GIS data is 10 metres. However, the figure clearly shows the extent of the slide and a large difference in the slope geometry before and after the slide.

### C.3.2 Material model for the soil

A major difficulty in obtaining a reliable numerical analysis of the particular slide is the complex material properties and the identification of layer boundaries present in the slope. In the considered problem, the soil consists of a complex pattern of clay and different sand materials. Further, the material properties, at the initiation of the slide, are uncertain. Another limitation is the lack of constitutive models involving very large deformations for soil materials. In order to test the frictional contact model and to study the suggested failure mechanism reported in

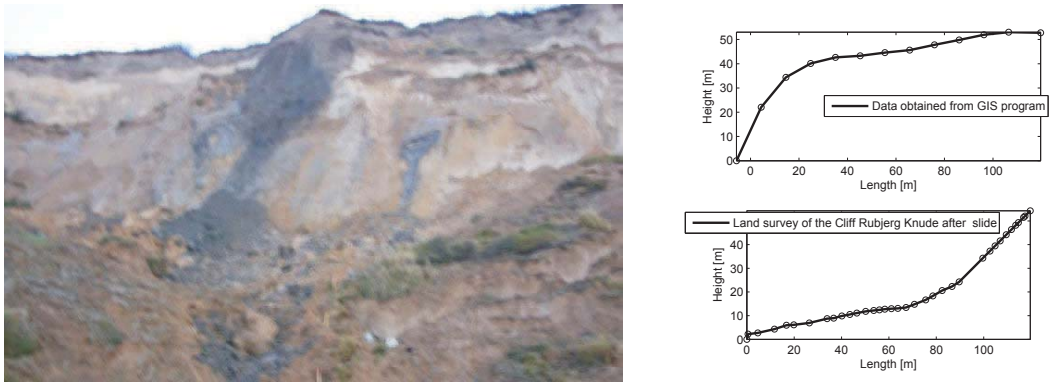


**Figure C.2** Left: The steep part of the slope after the slide. The soil in the steep part consist of a silty sand. Traces of clay, that has not eroded is visible. Right: Comparison of slope geometry before and after the slide.

(Tv2Nord 2008) a numerical model with simplified material assumptions is introduced.

By introducing simplified material and geometrical models, the soil is represented as two isotropic, homogenous materials, clay and sand. The clay and sand are modelled as different continuum materials. The interaction between the materials is described using the frictional-contact algorithm.

Both the sand and the clay are modelled as elasto-plastic materials, based on the Mohr-Coulomb yield criteria. A non-associated plasticity-model is employed. A yield function $f$ is introduced such that $f < 0$ corresponds to elastic material behaviour and elasto-plastic behaviour is observed when $f = 0$. The yield criterion is given in terms of the Mohr-Coulomb yield function defined in terms of the principal stresses by

$$f = \frac{1}{2}(\sigma_3 - \sigma_1) + \frac{1}{2}(\sigma_1 + \sigma_3)\sin(\phi) - c\cos(\phi) \leq 0, \tag{C.37}$$

where $\phi$ is the angle of friction and $c$ is the cohesion. In Equation (C.37), tension is considered positive and the principal stresses are ordered as $\sigma_1 \leq \sigma_2 \leq \sigma_3$. The stress rate is given in terms of the elastic strain rate, i.e.

$$\dot{\sigma}_{\alpha\beta} = E_{\alpha\beta\gamma\delta} : (\dot{\varepsilon}_{\gamma\delta} - \dot{\varepsilon}^p_{\gamma\delta}), \tag{C.38}$$

where $\dot{\varepsilon}_{\gamma\delta}$ is the total strain rate, $\dot{\varepsilon}^p_{\gamma\delta}$ is the plastic rate and $E_{\alpha\beta\gamma\delta}$ is the elastic constitutive tensor. The plastic strain increment is found using the relation

$$\dot{\boldsymbol{\varepsilon}}^p = \dot{\lambda}\frac{\partial g}{\partial \boldsymbol{\sigma}}, \tag{C.39}$$

where $\dot{\lambda}$ is a positive scaling factor and $g$ is the plastic potential function given by

$$g = \frac{1}{2}(\sigma_3 - \sigma_1) + \frac{1}{2}(\sigma_1 + \sigma_3)\sin(\psi). \tag{C.40}$$

Here $\psi$ is the angle of dilatation of the soil. In the numerical solution, finite increments in the strain are considered. Hence, the state of stress may initially be taken outside the yield surface.

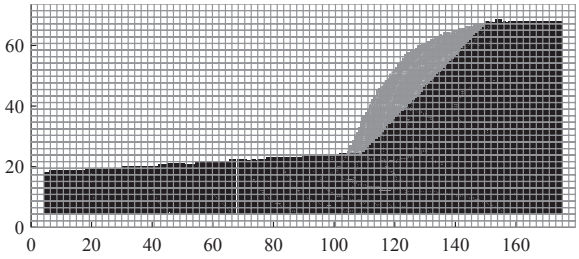


**Figure C.3** The configuration of material points before the slide. The mesh visible is the computational grid. A total number of 10977 material point is employed in the shown model. The darkest material is the sand and the brightest is clay. Geometric information from GIS data has been utilized for defining the geometry.

An efficient return of the stresses back to the yield surface is obtained by the algorithm proposed in (Clausen et al. 2006).

The clay and the sand is represented by the following sets of material properties

- **Sand**: $E = 20$ MPa, $\nu = 0.40$, $\rho_0 = 1900\ \mathrm{kg/m^3}$ $c = 0$, $\phi = 35°$, $\psi = 5°$
- **Clay**: $E = 20$ MPa, $\nu = 0.40$, $\rho_0 = 1900\ \mathrm{kg/m^3}$ $c = 100kPa$, $\phi = 1°$, $\psi = 0°$

The interface between sand and clay is modelled with an coefficient of friction $\mu = 0.6$. This corresponds to requiring a smaller force in order to enforce sliding at the interface than to trigger plastic response in the sand next to the interface, as $\tan 35° = 0.7$.

During the landslide, significant plastic shear strains are accumulated in the sand. This leads to over-excessive dilatation if the material model is used uncritically. To avoid this, dilation cut-off is implemented when the maximum void ratio for the sand has been reached. The cut-off condition is implemented numerically by representing all material points that has obtained the maximum void ratio as a new continuum. This allows the maximally dilated sand particles to slide relative to the remaining sand. In the present analysis, an initial void ratio of 0.5 is assumed and the maximum void ratio is estimated to 0.8. A more realistic model would consider the effects of capillary tension in the sand as well as the curvature of the yield function at low confining pressures (i.e. near the ground surface). The utilisation of more accurate material models is the focus of future research.

### C.3.3 Numerical model

A two-dimensional cross section is divided into a number of rectangular domains each represented by a material point (either clay or sand). A model with 80 computational cells in the horizontal. The model with 10977 material points is analysed, see Figure C.3. The geometry for the part of the numerical model representing the slope is obtained from the GIS data. The part of the model to the left of the slope, that represents the beach and the seabed, is modelled with an inclination of 6%. Three by three material points are defined for each cell of the grid. The initial stresses in the slope are determined using the algorithm presented in (Andersen and Andersen 2008) where the gravity is gradually applied to the material points. Based the geometry and the initial stresses, the deformed slope geometry is found by explicitly integrating in time. A time increment of $\Delta t = 0.002$s is employed in the presented model. The simulation has been set to

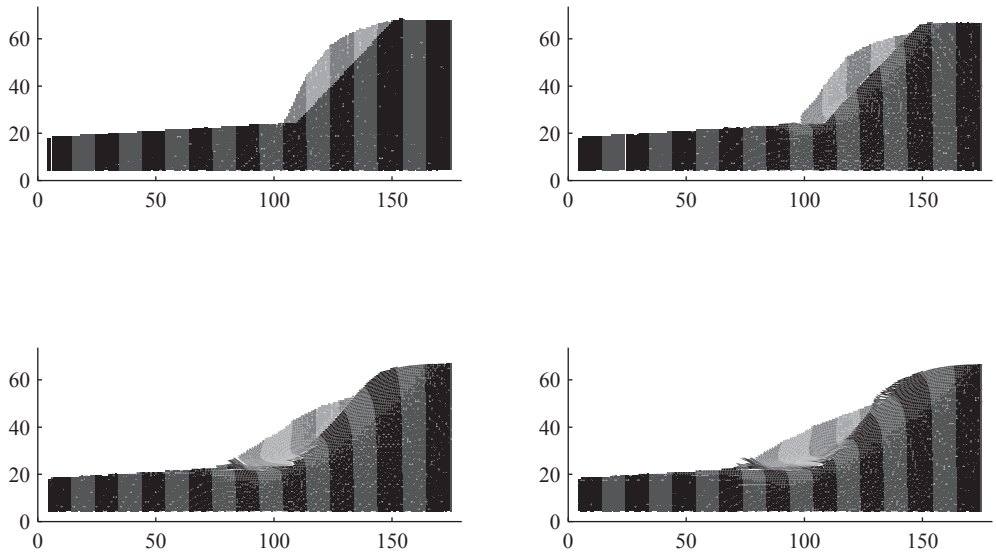


**Figure C.4** The geometry of the slope as a function of time. The stripes in the model are solely inserted to provide a better visualisation of the deformation mechanism. Upper left: start geometry. Upper right: $t = 2.9$s. Lower left: $t = 5.8$s. Lower right: $t = 9.0$s.

integrate, until the sliding motion has ceased. In the current model the slide took approximately 9.0s. Figure C.4 shows the configuration at different instances of time.

The slide starts as a slip at the interface between the clay and the sand. At $t = 2.9$s the sliding is mostly due to the clay sliding down the sand with some plastic deformations taking place in the clay. Plastic deformations in the sand is of little importance. At $t = 2.9$s the physically dominant interface is the interface between the clay and the sand. At $t = 5.8$s the interaction between the sand and the clay at the interface on the beach has lead to plastic deformations in the sand closest to the clay. Normal forces enforced onto the clay by the frictional-contact is now yielding a large contribution to stopping the slide. Another observation to be made from that figure is the significant changes in the shape of the clay. At $t = 9.0$s, after which no sliding is taking place, the clay has stopped at a new formed interface between the two materials (between $x = 70$ and $x = 90$metres). The interface has an inclination opposite to the inclination of the original slope. Hence, with the provided layer boundaries and material properties, the plastic deformations in the sand along the beach contributes in stopping the slide. Finally, comparing $t = 5.8$s with $t = 9.0$s plastic deformations is observed in the sand at the upper part (between $x = 130$ and $x = 150$metres).

## C.4 Conclusion

A new numerical technique for modelling large strain and deformation problems is presented. The model is an extension of the generalized interpolation material point method, employing numerical integration in the deformed state. Interaction between several materials, each modelled as a continuum, is modelled using a frictional contact algorithm based on a master-slave interface definition.

The numerical method is tested by analysing a recent landslide at Rubjerg Knude, located in northern Denmark. A two-dimensional model of the slope before the landslide is obtained using GIS data. The model is analysed with simplified material properties using representative materials of sand and clay, respectively. A Mohr-Coulomb model is employed to model the elasto-plastic of the two materials. The reported failure mechanism (Tv2Nord 2008), that the clay due to rainfall, has become so heavy that its starts sliding down along the interface with the sand, is tested. This is done by modelling the interface between the clay and the sand using the frictional contact algorithm to model the interface between the materials. With the utilized material and interface properties, the landslide is triggered at the interface between the sand and the clay. The elasto-plastic properties of the two soils are of a lesser importance for the initiation of the slide but has a significant influence during the slide.

The numerical test case shows that it is possible to model elasto-plastic deformation, slide between the different soil materials and the changes of the sand properties due to dilatation using a fairly simple model. A model able to handle all these physical effects simultaneously would be extremely difficult to construct using a conventional method such as the finite element method. Despite the many simplifications in the numerical representation of the physical problem, our results provides an insight into the physics during the slides while the numerical model provides qualitatively similar to physical slide observed.